3-16-2021

Penta-Modal Imaging Platform with OCT- Guided Dynamic Focusing for Simultaneous Multimodal Imaging

Arash Dadkhah
Adadk001@fiu.edu

FLORIDA INTERNATIONAL UNIVERSITY

Miami, Florida

PENTA-MODAL IMAGING PLATFORM WITH OCT- GUIDED DYNAMIC FOCUSING FOR SIMULTANEOUS MULTIMODAL IMAGING

A dissertation submitted in partial fulfillment of

the requirements for the degree of

DOCTOR OF PHILOSOPHY

in

BIOMEDICAL ENGINEERING

by

Arash Dadkhah

2021

To: Dean John L. Volakis
College of Engineering and Computing

This dissertation, written by Arash Dadkhah, and entitled Penta-modal Imaging Platform with OCT- guided Dynamic Focusing for Simultaneous Multimodal Imaging, having been approved in respect to style and intellectual content, is referred to you for judgment.

We have read this dissertation and recommend that it be approved.

_____
Wei-Chiang Lin

_____
Jessica Ramella-Roman

_____
Rong Wen

_____
Jin He

_____
Shuliang Jiao, Major Professor

Date of Defense: March 16, 2021

The dissertation of Arash Dadkhah is approved.

_____
Dean John L.Volakis
College of Engineering and Computing

_____
Andrés G. Gil
Vice President for Research and Economic Development
and Dean of the University Graduate School

Florida International University, 2021

DEDICATION

I dedicate this dissertation to my father, Manouchehr Dadkhah, my mother, Nadereh Bastami and my younger brother, Ashkan Dadkhah. Their unconditional support, encouragement, and selfless love have made this journey possible.

ACKNOWLEDGMENTS

I would like to thank my major advisor Professor Shuliang Jiao for guiding me throughout this journey and my dissertation committee members, Dr. Jessica Ramella-Roman, Prof. Rong Wen, Dr. Wei-Chiang Lin, and Prof. Jin He, for their continuous support. I would like to extend my gratitude to my lab members Dr. Jun Zhou for training me at the beginning of this journey, Nusrat Yeasmin for assisting me with the multimodal imaging development and Zahra Nafar for helping me with the software and image processing development. I would also like to acknowledge the assistance provided by Dr. Horatiu Vinerean from FIU animal facility for animal training and providing me with the animal models, and Dr. Qifa Zhou from University of Southern California for fabricating and providing me with the needle ultrasound transducer for the photoacoustic imaging microscopy experiments. I would like to thank Dr. Jun Li for preparing the malaria parasite samples for the multimodal imaging experiments.

I am grateful to my parents, Manouchehr Dadkhah and Nadereh Bastami, my supportive brother, Ashkan Dadkhah for their unconditional love and support during these years. Also, I would like to express my gratitude to all my colleagues, and friends who have extensively helped me during my Ph.D.

I would like to acknowledge the financial support received throughout my Ph.D. study, including the Teaching Assistantship from the Department of Biomedical Engineering, Research Assistantship from the National Institute of Health grants, and Dissertation Year Fellowship from University Graduate School at Florida International University.

Authorship Attribution Statement

This dissertation contains material from 4 published papers in the following peer-reviewed journals.

The content of chapter 3 is published in Biomedical Optics Express as Arash Dadkhah, Jun Zhou, Nusrat Yeasmin, and Shuliang Jiao," Integrated multimodal photoacoustic microscopy with OCT- guided dynamic focusing".

The content of chapter 4 is published in the Journal of Biomedical Optics, as Arash Dadkhah and Shuliang Jiao," Optical coherence tomography-guided dynamic focusing for combined optical and mechanical scanning multimodal photoacoustic microscopy".

The content of chapter 5 is published in Journal of Experimental Biology and Medicine, as Arash Dadkhah and Shuliang Jiao," Integrating Photoacoustic Microscopy, Optical Coherence Tomography, OCT Angiography, and Fluorescence Microscopy for Multimodal Imaging".

Parts of the content of chapter 2 and chapter 8 are published in Journal of Experimental Biology and Medicine, as Arash Dadkhah and Shuliang Jiao," Integrating Photoacoustic Microscopy with Other Imaging Technologies for Multimodal Imaging".

ABSTRACT OF THE DISSERTATION

PENTA-MODAL IMAGING PLATFORM WITH OCT- GUIDED DYNAMIC FOCUSING FOR SIMULTANEOUS MULTIMODAL IMAGING

by

Arash Dadkhah

Florida International University, 2021

Miami, Florida

Professor Shuliang Jiao, Major Professor

Complex diseases, such as Alzheimer's disease, are associated with sequences of changes in multiple disease-specific biomarkers. These biomarkers may show dynamic changes at specific stages of disease progression. Thus, testing/monitoring each biomarker may provide insight into specific disease-related processes, which can result in early diagnosis or even development of preventive measures. Obtaining a comprehensive information of biological tissues requires imaging of multiple optical contrasts, which is not typically offered by a single imaging modality. Thus, combining different contrast mechanisms to achieve simultaneous multimodal imaging is desirable. However, this process is highly challenging due to specific optical and hardware requirements for each optical imaging system.

The objective of this dissertation is to develop a novel Penta-modal optical imaging system integrating photoacoustic microscopy (PAM), optical coherence tomography (OCT), optical Doppler tomography (ODT), OCT angiography (OCTA) and confocal fluorescence microscopy (CFM) in one platform providing comprehensive structural, functional, and

molecular information of living biological tissues. The system can simultaneously image different biomarkers with a large field-of-view (FOV) and high-speed imaging. The large FOV and the high imaging speed is achieved by combining optical and mechanical scanning mechanisms. To compensate for an uneven surface of biological samples, which result in images with non-uniform resolution and low signal to noise ratio (SNR), we further develop a novel OCT-guided surface contour scanning methodology, a technique for adjusting objective lens focus to follow the contour of the sample surface, to provide a uniform spatial resolution and SNR across the region of interest (ROI).

The imaging system was tested by imaging phantoms, ex vivo biological samples, and in vivo. our multimodal imaging system was able to provide images of an in vivo mouse ear with FOV of 10 mm x 10 mm and an imaging time of ~5 minutes. In addition to measuring the blood flow, the system also successfully imaged mouse ear blood vessels, sebaceous glands, as well as several tissue structures. The multimodal imaging system outlined in this dissertation can be useful in a variety of applications thanks to the specific optical contrast offered by each employed modality, including retinal and brain imaging.

TABLE OF CONTENTS

CHAPTER PAGE

LIST OF TABLES

TABLE PAGE

LIST OF FIGURES

FIGURE PAGE

LIST OF ABBREVIATIONS

Photoacoutic Microscopy	PAM
Optical Coherence Tomography	OCT
Optical Coherence Doppler Tomography	ODT
Optical Coherence Tomography Angiography	OCTA
Confocal Fluorescence Microscopy	CFM
Multiphoton Microscopy	MPM
Diffuse Optical Tomography	DOT
Raman Spectroscopy	RS
Super-resolution Microscopy	SRM
Two-photon Microscopy	TPM
Charge-Coupled Device	CCD
Photoacoustic	PA
Swept-Source Optical Coherence Tomography	SS-OCT
Fourier-Domain Optical Coherence Tomography	FD-OCT
Age-related macular Degeneration	AMD

Choroidal neovascularization	CNV
American National Standards Institute	ANSI
area of interest	AOI
Wide-field Fluorescence Microscopy	WFM
Confocal Laser Scanning Microscopy	CLSM
Laser Confocal Scanning Microscopy	LCSM
Second Harmonic Generation	SHG
Autofluorescence	AF
Sclera	SL
Dichroic mirror	DM
Field of view	FOV
Maximum Permissible Exposure	MPE
National Institutes of Health	NIH
Near-Infrared	NIR
Near-Infrared light OCT	NIR-OCT
Neutral Density	ND
non-polarizing beam splitter	NBS
N-retinylidene-N-retinylethanolamine	A2E
Optical Density	OD
Photomultiplier Tube	PMT

Retinal Pigment Epithelium	RPE
Spectral-Domain Optical Coherence Tomography	SD-OCT
Superluminescent diode	SLD
Time Domain Optical Coherence Tomography	TD-OCT
Two dimensional	2D
Three dimensional	3D
Four dimensioal	4D
Pulse repetion rate	PRR
Cerebral blood flow	CBF
Improved speckle contrast	ISC
Optical microangiography	OMAG
Phase variance	PV

CHAPTER 1 Introduction

1.1 Significance of Multimodality Imaging Concept

Brain disorders, including Alzheimer's and Parkinson's disease, as well as brain cancerous tumors, are among the leading causes of death in the United States. With the staggering projected number of approximately 8 million people suffering from these disorders by 2030, early detection of these pathologies can substantially increase the survival rate and the effectiveness of treatment strategies. There are several concurrent functional and structural indicators known as "biomarkers", attributed to these disorders, which can be detected (using advanced imaging modalities) even prior to the appearance of global symptoms of these pathological conditions. These biomarkers include changes in the blood vessel structure, blood flow pattern and velocity, as well as alterations in the function of the brain neurons. Current imaging modalities are limited to measuring/detecting only a few of these indicators at a time due to the limited contrast mechanism each can provide. Therefore, there is a need to develop a multi-functional imaging system which can simultaneously test multiple biomarkers by imaging different optical contrast providing physicians with the necessary information for the early diagnosis of complex brain disorders and to advance the field of medical imaging. However, combining different contrast mechanisms to achieve simultaneous multimodal imaging is always challenging due to the different optical and hardware requirements for different imaging systems.

1.2 Rationale

We developed a multimodal microscopic optical imaging system with the capability of providing comprehensive structural, functional, and molecular information of living tissues. This imaging system integrated photoacoustic microscopy (PAM), optical coherence tomography (OCT), optical Doppler tomography (ODT), Optical coherence tomography angiography (OCTA), and confocal fluorescence microscopy (CFM) in one platform. By taking advantage of the depth resolving capability of OCT, we developed a novel OCT-guided surface contour scanning methodology for dynamic focusing adjustment. We have conducted phantom, in vivo, and ex vivo tests to demonstrate the capability of the multimodal imaging system for providing comprehensive microscopic information on biological tissues. Integrating all the aforementioned imaging modalities with OCT-guided dynamic focusing for simultaneous multimodal imaging has promising potential for preclinical research and clinical practice in the future.

1.3 Design Goals

The overall goal of the dissertation in this document is to develop a multimodal optical imaging system integrating PAM, OCT, ODT, OCTA, and CFM in a single platform. The multimodal imaging technology should be able to:

- Simultaneously acquire PAM, OCT, ODT, CFM together with OCTA using a broadband Near-infrared (NIR) light source and a visible pulsed laser.
- Image objects with uneven surface using a novel OCT-guided contour scanning methodology.

- Perform dynamic focusing in two modes: point by point and area by area.
- Perform imaging with high speed and large field of view (FOV) using the combined optical and mechanical scanning scheme.
- Provide comprehensive structural, functional, and molecular information on living tissues.
- Be suitable for preclinical research and clinical practice in the future.

The specific aims listed below serve to accomplish these goals and further translation of the Penta-modal imaging system for clinical use.

1.4 Specific Aims

1.4.1 Specific Aim 1: To develop an integrated PAM, OCT, ODT, and CFM for multimodal imaging of biological sample along with a novel OCT-guided surface contour scanning methodology and apply it to in vivo animal imaging (Chapter 3).

a) To design and develop a simultaneous multimodal imaging system integrating PAM, OCT, ODT, and CFM in a single platform that employs two light sources: i) a single broadband NIR light source with center wavelength 840 nm and bandwidth of 100 nm ii) and a visible pulsed laser (532 nm) will be used for OCT/ODT/OCTA and PAM/CFM, respectively.

b) To develop a novel OCT-guided surface contour scanning methodology for dynamic focusing.

c) To test the capability of the developed multimodal imaging system with dynamic focusing by imaging phantom, ex vivo and in vivo animal models.

1.4.2 Specific Aim 2: To combine optical and mechanical scanning to achieve large FOV and high speed for multimodal imaging together with OCT-guided dynamic focusing. (Chapter 4)

a) To incorporate a pair of galvanometer-driven mirrors into the optical system to achieve fast scanning and large FOV.
b) To modify the developed OCT-guided contour scanning methodology to become compatible with the combined optical-mechanical scanning scheme.
c) To assess the capability of the modified multimodal optical imaging system with areal dynamic focusing and the combined optical and mechanical scanning scheme by imaging ex vivo and in vivo samples.

1.4.3 Specific Aim 3: To achieve multimodal imaging with integrated PAM, OCT, CFM and OCTA and perform in vivo experimental animal imaging. (Chapter 5)

a) To incorporate a charge-coupled device (CCD) camera with a higher line rate of 70 kHz to perform OCT angiography.
b) To test the upgraded multimodal imaging system by imaging phantom and in vivo specimens.

1.5 Organization of this Dissertation

Chapter 1: Introduction

This chapter discusses the significance and rationale behind this project and the organization of this dissertation.

Chapter 2: Biomedical optical imaging technology

In this chapter, we review the principle of different optical imaging techniques including photoacoustic imaging, optical coherence tomography (OCT), optical Doppler tomography, OCT angiography, and confocal fluorescence microscopy imaging. We also review some of the previously developed multimodal optical imaging instruments including dual modal and tri modal optical imaging systems. Later, we introduce our Penta-modal imaging system to overcome the limitations caused by the complexity of combing different imaging modalities.

Chapter 3: Integrated multimodal photoacoustic microscopy with oct-guided dynamic focusing

This chapter reviews the design and development of the Penta-modal imaging system with two light sources, in the near infrared (NIR) and visible spectrum, for OCT/ODT and PAM/CFM, respectively. In addition, the novel OCT-guided contour scanning methodology for dynamic focusing is explained in detail. The imaging system with dynamic focusing was tested on phantom, ex vivo human eye and in vivo mouse ear.

Chapter 4: OCT-guided dynamic focusing for combined optical and mechanical scanning multimodal photoacoustic microscopy

This chapter reviews the modified multimodal imaging system, which integrated optical resolution photoacoustic microscopy, optical coherence tomography (OCT), and confocal fluorescence microscopy in one platform to achieve fast imaging and a large field of view (FOV). The imaging speed and FOV were improved by combining optical scanning with mechanical scanning. To ensure good focusing of the objective lens over all the imaged area, the OCT-guided dynamic focusing was modified and the areal focusing adjustment strategy was applied. The performance of the system was demonstrated by imaging biological samples ex vivo (plant leaf) and in vivo (mouse ear).

Chapter 5: Integrating photoacoustic microscopy, optical coherence tomography, OCT angiography, and fluorescence microscopy for multimodal imaging

In this chapter, we explain our investigation on the feasibility of integrating the OCTA function into our multimodal imaging platform. The upgraded imaging system was able to perform fast imaging with a large field of view (FOV) by combining optical scanning with mechanical scanning, similar to the previous imaging configuration described in Chapter 4. The capability of the multimodal imaging system together with the OCTA function was validated by imaging a mouse ear in vivo.

Chapter 6: Comparative study of optical coherence tomography angiography algorithms for rodent retinal imaging

In this chapter, we present the results of a comparative study of OCTA algorithms for rodent imaging. We imaged in vivo rats' retinal and a mouse ear in vivo and applied three OCTA algorithms, namely the phase variance (PV), improved speckle contrast (ISC), and optical microangiography (OMAG), to visualize the blood vessels and the microvasculature networks. Both qualitative and quantitative studies were conducted to assess the performance of each OCTA image processing technique.

Chapter 7: Mosquito malaria parasite midgut multimodal imaging

In this chapter, we report the preliminary results in a study of multimodal imaging of plasmodium parasites in mosquito midguts. An ex vivo midgut sample was imaged with OCT, CFM, and PAM to demonstrate the capability of the proposed imaging system for imaging different biomarkers. Lastly, we imaged an in vivo infected mosquito using OCT motion-contrast imaging together with conventional OCT. It was shown that the proposed imaging system can potentially be used in the study of the malaria parasites.

Chapter 8: Concluding remarks

Concluding remarks include a summary of the proposed multimodal imaging system technology, its capabilities, and its limitations. Further, future applications toward the clinical usefulness of the technology have been discussed.

CHAPTER 2 Biomedical Optical Imaging Technology

2.1 Optical Imaging Technology

Optical imaging is an emerging technique for non-invasively imaging different organs, tissues, and cells inside the body. Unlike other imaging techniques such as X-ray, optical imaging is non-ionizing and takes advantage of light, including visible, ultraviolet, and infrared light (NIR), to see and measure different properties of various tissue structures, cells, and even molecules at the same time [1]. Optical imaging is rapidly growing and being applied in a variety of applications ranging from clinical diagnosis to molecular biology. Scientists and physicians also use optical imaging techniques for research studies and disease diagnosis/treatment. Due to the capability of monitoring functional and structural changes with the high spatial resolution and high sensitivity which optical imaging technique can offer, it is expected that optical technologies can make a substantial impact on the prevention and treatment of lethal diseases such as cancer. Optical imaging techniques are inexpensive, portable, and safe with the capability of adapting to endoscopes and microscopes providing images in both microscopic and macroscopic scales.

The major limitation of optical imaging is the imaging penetration depth, which is due to the high scattering property of biological tissues. However, scientists tackle this limitation by using NIR light to excite tissues improving the penetration depth up to few centimeters. There are various optical imaging techniques, such as photoacoustic microscopy (PAM) [2,3], optical coherence tomography (OCT) [4,5], optical Doppler tomography (ODT) [6,7], optical coherence tomography angiography (OCTA) [8,9], confocal fluorescence microscopy (CFM)

[10], multi-photon microscopy (MPM) [11], diffuse optical tomography (DOT) [12], Raman spectroscopy (RS) [13], super-resolution microscopy (SRM) [14], etc. Here, we briefly review the principle of the optical imaging technologies which has been developed in this dissertation: PAM, OCT, ODT, OCTA and CFM.

2.1.1 Photoacoustic Imaging Microscopy

Photoacoustic microscopy (PAM) is an emerging branch of photoacoustic (PA) imaging, a field of hybrid optical imaging technologies. It has attracted tremendous attention among scientists and researchers in the biomedical optical imaging field since invented more than a decade ago. It has been shown that PAM can image the structure and function of biological tissues with three-dimension (3D) spatial resolution by taking advantage of the spatially-resolved PA effect. [15] The PA effect is generated in a sample as a result of a transient pressure increase upon the illumination of a pulsed/intensity-modulated laser. The pressure increase is caused by the conversion of the light energy into heat when absorbed by an optical absorber in the biological sample, typically hemoglobin in the blood or melanin. The locally absorbed light energy together with the sample's mechanical and thermal properties determines the amplitude of the initial pressure impulse.[16,17] The amplitude of the generated initial pressure rise is expressed as:

$$P(\vec{r}) = \Gamma \eta \mu_a(\vec{r}) F(\overrightarrow{r}) \qquad (1)$$

where Γ is the Grueneisen parameter; η is the contributed absorbed light percentage that is converted into heat; μ_a is the absorption coefficient; and, F is the local optical fluence.

Eventually, ultrasonic waves are generated and detected with an ultrasonic transducer converting them into electric signals. The signals are then amplified, digitized, and constructed into an image with a computer. The transverse resolution of PAM is determined by either the ultrasonic or the optical focus and accordingly the technology can be categorized as either acoustic- or optical-resolution PAM (AR-PAM vs OR-PAM).[18] Different from AR-PAM, where the light illuminates an area bigger than the ultrasonic focal spot, in OR-PAM the illuminating light is focused into the sample. [19] In both versions of PAM, the frequency of the ultrasonic transducer and its bandwidth determines the depth resolution.

PAM offers additional complementary information when integrated with other imaging technologies in a multimodal imaging platform. PAM images the optical absorption contrasts of biological tissues, a unique contrast mechanism different from other imaging modalities.

2.1.2 Optical Coherence Tomography

Optical coherence tomography (OCT) is an optical imaging method based on low-coherence light providing three-dimensional and cross-sectional imaging within biological tissues with no need for exogenous contrast agent [20]. In general, there are two main OCT imaging techniques: time-domain OCT (TD-OCT) [21] and Fourier-domain OCT (FD-OCT) [22]. The latter can also be performed in two different approaches: spectral-domain OCT (SD-OCT) [23] and swept-source OCT (SS-OCT) [24]. In OCT, either time-domain or Fourier-domain, optical contrast is generated in the image as a result of the nonuniformity of refractive indices in different boundaries of examined tissue based on various reflection

and scattering properties of tissue. The key components of OCT imaging systems include a low coherence light source, sample arm, reference arm, and detector. TD-OCT was first introduced and appeared in the1990s [25] and since then, the principle and the theory along with its applications have been frequently reported and can be found in the literature. In TD-OCT, the back-scattered light is sequentially detected by the step-movement of a reference mirror from a different depth, while in FD-OCT, all the light echoes are acquired simultaneously from the entire depth as modulations in the source spectrum. The major difference between TD-OCT and FD-OCT systems is that the former employs a moving mirror while the latter uses a stationary mirror in their reference arms. Due to the elimination of the moving mirror, FD-OCT systems can perform imaging with a much higher imaging speed compared to TD-OCT systems.

OCT has been applied in various clinical studies, including cardiology [26], ophthalmology [27], dermatology [28]. However, due to the excellent axial resolution as well as the high imaging speed, OCT has been extensively used in in vivo retina imaging studying the morphology of the eye with age-related macular degeneration (AMD) [29] and Choroidal neovascularization (CNV) [30]. Currently, several companies have developed and commercialized OCT imaging systems that are being used in clinics and research, such as Carl Zeiss Meditec, Optovue, Heidelberg, Optopol, and Nidek.

2.1.3 Optical Coherence Doppler Tomography

Optical coherence Doppler tomography (ODT) is one of the functional extensions of OCT to visualize and quantify vasculature and blood flow in living tissues [31]. Since many diseases are associated with vascular abnormalities as well changes in blood flow, ODT

has become a very attractive imaging technique, i.e., several ocular diseases were found to be linked to changes in retinal blood flow including diabetic retinopathy, age-related macular degeneration, and glaucoma. Due to the high resolution which OCT can offer, ODT is also capable of imaging small capillaries within biological specimens. ODT can be performed in both TD-OCT and FD-OCT systems, however, the Fourier-domain ODT (FD-ODT) has been largely replaced with time-domain ODT (TD-ODT) and is extensively used in the clinical environment due to its unprecedented imaging speed and sensitivity which it can provide, similar to FD-OCT.

The ODT flow signal is extracted by calculating the phase difference between adjacent depth profiles for each depth position [32]. The phase difference $\Delta\phi$ (x, z) needs to be confined to $[-\pi, \pi]$ to avoid phase unwrapping. Briefly, the projected flow speed on the direction of the incident sample light can be calculated from the phase difference among the adjacent A-lines $\Delta\varphi_i = \varphi_{i+1} - \varphi_i$, where i is the A-line number:

$$v_p = \frac{\Delta\varphi_i \lambda_0 f_{A-line}}{4\,\pi n} \tag{2}$$

where v_p is the projection of the absolute velocity v_a along the depth direction, λ_0 is the center wavelength of the light source, f_{A-line} is the axial scan frequency (A-line rate), n is the index of refraction of the sample.

2.1.4 OCT Angiography

Optical coherence tomography angiography (OCTA) is non-invasive motion contrast-based imaging technology that has become a powerful tool for visualizing microvasculature in living tissues among researchers and physicians [33]. OCTA

differentiates flowing particles (i.e., mainly red blood cells in blood flow) from static background tissues without using any dye agent generating volumetric angiography images in a matter of seconds. To extract decorrelation signals constructing a map of blood flow, OCTA measures the difference in the back-scattered OCT signal intensity or phase between sequentially acquired OCT B-scans at the same cross-section location. Several algorithms have been developed for OCTA image visualization, e.g., the OCT signal contains intensity/amplitude and phase information after Fourier transform. These algorithms are categorized into: i) phase-signal-based OCTA[34], ii) intensity-signal-based OCTA [35], and (iii) complex-signal-based OCTA [36].

OCTA has rapidly gained clinical acceptance and revolutionized the practice of ophthalmology in the past two decades becoming a powerful imaging technology to evaluate common ophthalmologic diseases, such as diabetic retinopathy [37], glaucoma [38], age-related macular degeneration (AMD) [39], artery and vein occlusions [40]. In addition, OCTA has also been used in other research and clinical areas such as dermatology [41], gastroenterology [42] and neurology [43].

Currently, several OCTA instruments are commercially available throughout the world for research use, including Carl Zeiss Meditec (AngioPlex™), Optovue (AngioVue™), and Topcon Medical (Triton™ DRI SS-OCT). Most other major OCT manufacturers, including Heidelberg, Optopol, and Nidek, have demonstrated OCTA platforms at major meetings and have these devices available for research use only at specific sites.

2.1.5 Confocal Fluorescence Microscopy

Confocal fluorescence microscopy (CFM) is a popular imaging tool among researchers and scientists mainly due to its ability to eliminate the out-of-focus light causing blurry images [44]. CFM employs point-by-point illumination and a pinhole in front of the detector to remove the unfocused signals. Comparing CFM to conventional wide-field fluorescence microscopy (WFM) [45] which only image thin specimens, CFM can image thick samples generating clear 2D and 3D images with high spatial resolution. CFM performs sharply focused optical sectioning by acquiring images of thin slices of a thick specimen which eventually stack all the images to reconstruct a high-quality 3D image. The most frequently used confocal microscopy techniques include confocal laser scanning microscopy (CLSM) [46] or laser confocal scanning microscopy (LCSM) [47].

CFM has been mainly used in dermatology [48] for studying the skin surface, epidermis, and superficial dermis due to its ability to offer a cellular resolution. In addition, Fluorescence confocal microscopes have become an attractive tool in biological research in which a variety of dyes, immunofluorescence probes, and green fluorescent protein are imaged. Even though CFM has many advantages compared to WFM, (i.e., this includes providing the high optical resolution and contrast of an image of a specimen, reconstructing clear 3D images, and offering optical sectioning within thick specimens), CFM still has some limitations such as the imaging depth within thick specimens, the higher cost compared to WFM as well as photobleaching and phototoxicity.

2.2 Combination of PAM, OCT, ODT, OCTA and CFM

Even though each of those above-mentioned optical imaging techniques has been successfully used in various biomedical research, a single imaging modality alone cannot provide all the information needed for a full understanding of the tissue pathophysiology and disease diagnosis. This is due to a certain type of optical contrast mechanism that each can acquire. To fill this gap, multimodal optical imaging microscopy systems are proposed by integrating different imaging techniques to offer more comprehensive information from a biological sample. Multimodal imaging with combined PAM, OCT, ODT, OCTA, and CFM can offer different optical contrasts of a biological sample, including absorption, scattering, fluorescence, and motion contrast.

Several research groups have developed different multimodal optical imaging systems for imaging the various characteristics of biological specimens, including dual-modal [49,50], and tri-modal imaging [51-53] systems. The feasibility of mapping two different molecules simultaneously by imaging the absorption and fluorescence contrasts using a single pulsed light source was first reported in 2010. [54] The technique was demonstrated by imaging excised ocular tissues. Xiangyang Zhang et al [55] further integrated photoacoustic ophthalmoscopy (PAOM), a PAM technology for imaging the retina in vivo, with autofluorescence (AF) imaging. The technique was able to image melanin and lipofuscin in the retinal pigment epithelium (RPE) cells of rat eyes simultaneously in vivo with a single light source of 532 nm. The PAM-AF imaging system was also integrated with a spectral-domain OCT, which used a near-infrared broadband light source centered at 830 nm. The OCT system provides guidance to PAOM and can help reduce visible laser

exposure to the eye. The pulsed laser light was scanned and delivered to the eye by an X-Y galvanometer scanner in combination with a pair of relay and ocular lenses. For PAM signal detection, a single element unfocused 30 MHz needle ultrasound transducer placed on the eyelid using ultrasonic coupling gel was used. The fluorescence signal was detected with an avalanche photodiode through a 50 μm multimode optical fiber acting as a pinhole. With a 24 kHz PRR, the system can acquire 3D images of the retina within 2.7 seconds.

Dual modal OR-PAM and CFM using a single excitation laser was also demonstrated by Yu Wang et al [56] for in-vivo mouse ear imaging to examine tumor angiogenesis, vasculature, and microenvironments. The sample was illuminated by two wavelengths, 570 nm and 593 nm, which were applied sequentially for each B-scan. The PAM mode was thus able to provide oxygen saturation imaging of the blood vessels. With a 75 MHz ultrasonic transducer, the depth and transverse resolutions were quantified, 17 μm and 3.9 μm for PAM, 38 μm and 3.9 μm for CFM. By combining PAM angiography and fluorescence lymphangiography, they successfully demonstrated that the dual modal PAM-CFM system was able to provide comprehensive information for monitoring the growth and treatment effect of tumors in small animals.

Combining PAM with OCT was first introduced in 2009 for in vivo animal imaging, [57] by using two different light sources for PAM and OCT. Xiangyang Zhang et al [58] reported the first dual modal PAM-OCT technology in 2012 using a shared broadband pulsed light source to achieve PAM and OCT imaging simultaneously. The PAM signal was detected with an unfocused ultrasonic transducer while the OCT interference signal was detected with a Michelson interferometer in the spectral domain. The technology was termed optical

coherence photoacoustic microscopy (OC-PAM). Following that, several research groups published similar techniques. [58-61]

The first reported OC-PAM [58] used a pulsed broadband dye-laser (center wavelength: 580 nm) for both PAM and OCT. The OCT Michelson interferometer was built in free space. Each laser pulse generated one depth-scan for both imaging modalities. The speed of the PAM and OCT was determined by the PRR of the dye laser (Maximum PRR: 5 kHz). The system was demonstrated by imaging the vasculature of a mouse ear in vivo. Changho Lee et al [61] also combined PAM with OCT in 2013 using a supercontinuum laser source centered at 1064 nm; however, no in vivo imaging study was reported in their work.

Xiaojing Liu et al [59] reported an OC-PAM technology in 2015 to provide multimodal in vivo imaging of the retina. The system used an ultrafast Ti:sapphire laser amplifier as the illuminating light source for both PAM and OCT (Maximum PRR: 10 kHz, center wavelength: 800 nm, bandwidth: 30 nm). A 2 × 2 single-mode optical fiber coupler was used to build the Michelson interferometer for OCT. A custom-built needle ultrasonic transducer was used to detect the PAM signal. The transducer (center frequency: 30 MHz, active element diameter: 0.4 mm) was placed in contact with the eyelid coupled with ultrasound gel. Pigmented rat retina was successfully imaged, in which the retinal layer structures were imaged by OCT, while the melanin distribution in the retina was imaged by PAM.

OC-PAM with an intensity-modulated continuous-wave light source was also demonstrated. [62] The technique used an 840 nm superluminescent diode (SLD). The output light was modulated by modulating the SLD driving current. Compared to pulsed OC-

PAM, the advantage of this technique is that the OCT image quality can be as good as conventional spectral-domain OCT with similar light intensity and bandwidth. The technique was tested by imaging biological samples in vivo and ex vivo. Gold nanorods were used as contrast agents for the PAM mode when the vasculature of the mouse ear was imaged.

Magalie Bondu et al [60] reported a dual modal OCT-PAM technology with a configuration similar to Ref. 23 except that a supercontinuum light source was used. Although the same light source was used, the OCT and PAM were generated by different bands of the supercontinuum output: OCT used the band centered at 1310 nm while PAM used the band of 500– 840 nm. Since the center wavelength and bandwidth of the light source can be independently selected, the system can perform multispectral PAM (MPAM). A customized ultrasonic transducer (center frequency: 40.3 MHz, active element: φ0.4 mm) was used to detect the PA signals. The system achieved an imaging speed of 20 B-scans/second for both PAM and OCT. The system was tested on phantoms and in vitro samples using dyes as the contrast agent.

In this dissertation, we present a novel Penta-modal optical imaging system integrating PAM, OCT, ODT, OCTA, and CFM. The system can simultaneously image different biomarkers in biological tissues with large FOV and high-speed imaging. The imaging system also features our novel OCT-guided dynamic focusing technique, suitable for imaging objects with uneven surfaces. The details of the design, development, and assessment of the performance of the Penta-modal imaging system using phantoms, ex vivo and in vivo specimens, will be discussed in subsequent chapters.

CHAPTER 3 Integrated Multimodal Photoacoustic Microscopy with OCT-guided Dynamic Focusing

3.1 Introduction

Over the past years, various optical microscopy techniques, such as optical coherence tomography (OCT) [63,64], confocal fluorescence microscopy (CFM) [65-67], photoacoustic microscopy (PAM) [17,68,69], and optical Doppler tomography (ODT) [31,70,71], have been established and broadly applied in biomedical research and preclinical/clinical studies. All these optical imaging techniques have been shown to be a powerful tool for revealing structural, functional and molecular features of biological specimens noninvasively [1,72-76]. Based on low-coherence interferometry, the imaging contrast of OCT is mainly provided by boundaries formed by regions with different optical properties. OCT is capable to offer structural information of biological tissues with no need for exogenous contrast agents. ODT is a branch of OCT, which is used to characterize the functional information, e.g. the blood flow velocity (mainly the flow velocity of the red blood cells), of biological samples with high resolution [31,71]. Blood flow is an important functional parameter for biological tissues, for example, various ocular diseases are associated with alterations in blood flow, such as glaucoma, age-related macular degeneration, and diabetic retinopathy [77-79].

Photoacoustic microscopy (PAM) is an emerging microscopic imaging technology, which is capable of extracting optical absorption information in biological samples based on the photoacoustic effect. In PAM, the sample is irradiated by a pulsed laser with a pulse width down to a few nanoseconds, and a broadband ultrasonic wave is produced as result of rapid

temperature rise as well as thermo-elastic expansion/relaxation process of the tissue [80]. The photoacoustic (PA) waves are detected by an ultrasound (US) transducer, and an optical absorption-based PA image can be constructed. Optical-resolution photoacoustic microscopy (OR-PAM), a well-known branch of PAM, relies on the optical focus to provide high lateral resolution at the cost of imaging depth [81]. OR-PAM has successfully demonstrated its great potential for structural and functional imaging in living animal models, such as vessel morphology, brain activity, and oxygen metabolism [69,82-85].

CFM is an established technology for imaging the molecular features of biological specimen by mapping the distribution of fluorophores with known fluorescence spectrum [86]. Confocal fluorescence microscope employs a pinhole at the detector site to block the light coming from out-of-focus planes [87]. As a result, high resolution biological imaging is achieved with autofluorescence or exogenous fluorophore. CFM has been explored as an analytical instrument for studying various biochemical reactions in intact living cells [88-90].

Each individual imaging technology has its limitations due to the limited specific contrast mechanism used for imaging, and thus each imaging technology alone cannot provide all the information needed for biomedical research and disease diagnosis. For example, conventional OCT in the near infrared spectrum cannot offer molecular contrasts; PAM and CFM are capable of providing optical absorption and molecular information of a biological specimen in cellular level, however, they cannot provide contrasts of tissue structure as OCT can offer and they do not provide blood flow information. To overcome their limitations, multimodal optical microscopy imaging systems are developed to gather more comprehensive information from a biological specimen that was previously

unavailable by using a single modal microscope [17,51,91-93]. Many efforts have been made in developing various multimodal imaging systems to provide simultaneous imaging of the different properties of biological samples. For instance, a dual-modal imaging system, combining OCT and CFM, was built for simultaneous visualization of biochemical as well as morphological features of biological tissue [94-97]. A tri-modal imaging microscope, integrating PAM, two-photon, and second harmonic generation microscopy, has been successfully developed for simultaneous multimodal imaging of mouse ear. In another study, a hybrid optical system has been developed by combining optical-resolution PAM, two-photon excitation fluorescence (TPEF), second harmonic generation (SHG) and third harmonic generation (THG) microscopy for label-free imaging of a mouse ear and zebrafish larva ex-vivo [51,98].

For microscopic imaging, the lateral resolution and signal intensity highly rely on focusing of the objective lens. Dynamic focusing is necessary when the contour of the sample surface is uneven and has a range of depth-variation that exceeds the depth of focus of the objective lens. Several groups have reported dynamic focusing for PAM imaging by using contour scan with PAM [99] or ultrasound [100]. In comparison, our multimodal imaging system provides an unprecedented advantage that the OCT system can accomplish the contour scan with potentially much higher imaging speed and better depth resolution.

In this paper, we present a quad-modality microscopy imaging system that combined OCT, CFM, PAM and ODT to achieve simultaneous multimodal imaging together with dynamic focusing enabled by the integrated OCT system. The system can gather more comprehensive information of biological samples by imaging the complementary

contrasts, including optical backscattering, optical absorption, blood flow speed and fluorescence. The imaging system was tested on a phantom as well as biological tissues both in vivo and ex vivo.

3.2 Methods

3.2.1 Imaging System

A schematic of the experimental setup is shown in Fig. 3-1. The system employs two light sources, in the near infrared (NIR) and visible spectrum, for OCT/ODT and PAM/CFM, respectively. OCT/ODT works with a single broadband NIR light source (T-840 Broadlighter; Superlum Diodes Ltd, center wavelength 840 nm, FWHM bandwidth 100 nm). In PAM/CFM, a single Q-switched frequency-doubled Nd:YAG laser (SPOT-10-200-532, Elforlight Ltd, UK; output wavelength: 532 nm; maximum pulse energy: 20 μJ; pulse duration: 2ns; maximum pulse repetition rate: 30 kHz) is used as the illuminating light source. The NIR light power was measured to be 570 μW. The laser pulse energy was measured to be 300 nJ on the sample during the experiments. The pulsed laser light first passed through a neutral density filter (ND, optical density: 0.04), the surface reflection from which was detected by a photodiode (PD) whose output was used to trigger a digital delay generator for synchronization of the different imaging modalities. The laser light was attenuated by a set of neutral density filters before coupled into a single-mode optical fiber (SMF). After exiting the SMF, the light was collimated into a beam diameter of 2 mm, combined with the OCT probe light by a dichroic mirror (DM1, DMSP650 - Ø1" Shortpass, 650 nm Cutoff, Thorlabs), and focused onto the sample with an objective lens (Microspot focusing objectives, LMH-5X-532, EFL= 40mm, NA=0.13, Thorlabs).

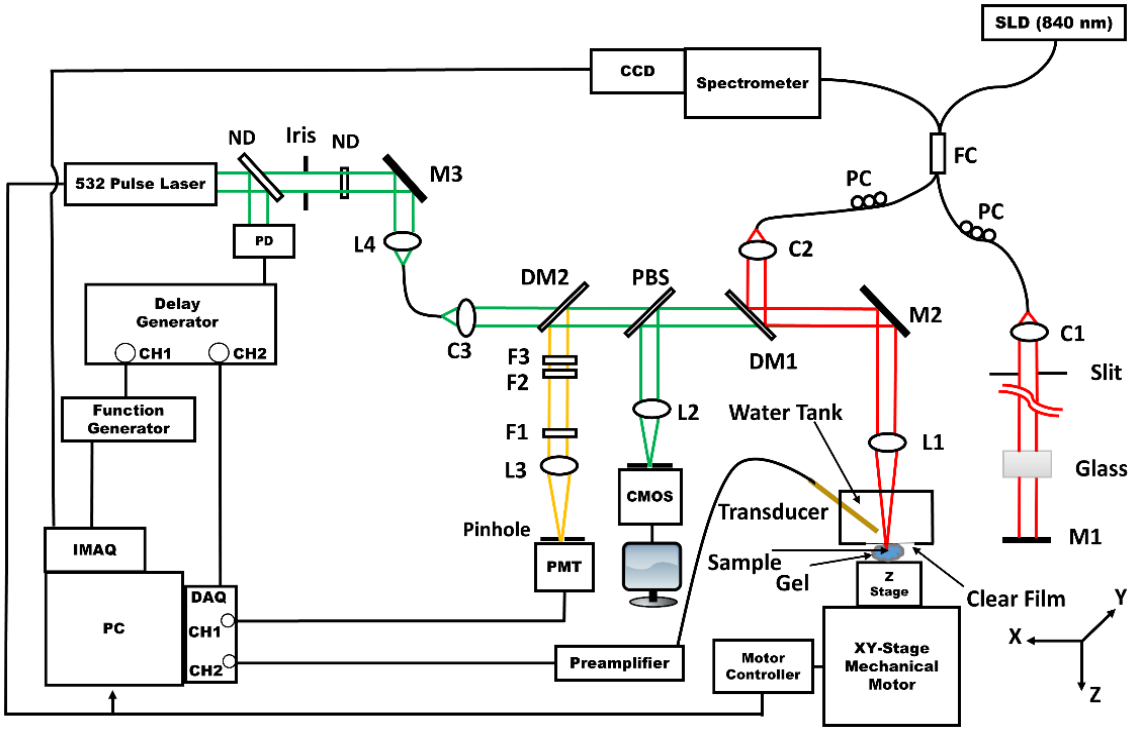

Figure 3-1 Schematic of the integrated PAM/OCT/ODT/CFM experimental system. SLD: Superluminescent diode; FC: 2×2 Fiber coupler; PC: Polarization controller; L1, L2, L3, L4: Lens; M1, M2, M3: Mirror; DM1, DM2: Dichroic mirror; C1, C2, C3: Collimator; ND: Neutral density filter; F1, F2, F3: Optical filter; PBS: Pellicle beam splitter; PD: Photodiode.

For PAM signal detection, an unfocused needle ultrasonic transducer (40 MHz, bandwidth 80%, active element diameter 1.3 mm) was immersed in a water tank filled with distilled water. A window was opened at the bottom of the water tank and was sealed with a transparent polyethylene membrane. For imaging, a sample is placed under the window between the polyethylene membrane and a glass cube, and acoustically coupled with ultrasonic coupling gel. The induced PAM signals were amplified by a 54 dB preamplifier, and then digitized and directed to the PC by a digitizer (PCI-5154, National Instruments) with a sampling rate of 200 MS/s. A total of 1000 points corresponding to a sampling time of 5 μs were acquired with no signal averaging at each scanning position on the sample.

In the CFM subsystem, the back traveling fluorescence light excited by the pulsed laser in the sample passed through the dichroic mirror combining the OCT light and the 532 nm laser (DM1), reflected by another dichroic mirror (DM2, Short-pass, cutoff wavelength: 550 nm, Edmund Optics), passed through a short-pass filter (F1, FES0750, cutoff wavelength: 750 nm, Thorlabs) for blocking the back-reflected NIR light, and a long-pass filter (F2, FES0550, cutoff wavelength: 550 nm, Thorlabs) together with a laser rejection filter (F3,532 nm BP, OMEGA). It was then focused into a 25 μm pinhole by an achromatic doublet with a focal length of 30 mm (L3) and detected by a PMT module (PMM02, Thorlabs). The output signal of the PMT was digitized into the computer by another channel of the same digitizer. The sampling rate and the record length were the same as for the PAM subsystem.

In the OCT/ODT subsystem, the light from the broadband light source was coupled into a 3dB 2×2 fiber coupler and was split into the sample and reference arms. In the sample arm, the light exiting the fiber was collimated and combined with the PAM laser with the dichroic mirror DM1. The combined reflected light from the sample and reference arms was detected by a spectrometer. The spectrometer consisted of a 1200 lines/mm transmission grating, a multi-element imaging lens (f = 150 mm), and a line scan CCD camera (Aviiva-SM2-CL-2014, 2048 pixels with 14 μm pixel size operating in 12-bit mode, e2V) with an exposure time of 36μs.

Step-motor driven platforms (UniSlide, Velmex, Inc.) were used for scanning the sample and adjusting the focus of the objective lens. The sample together with the water tank was scanned in the X- and Y-directions by using a 2-axis platform. Each image was set to have

256×256 or 512×512 steps (X × Y) covering either 1.6 mm × 1.6 mm or 6.5 mm × 6.5 mm area, a step size of 6.4 μm or 12.8 μm. The entire image acquisition took about 20 or 80 minutes, respectively. The focus of the objective lens was adjusted by the Z-scan platform, which was controlled with the guidance of the OCT contour scan.

All the imaging subsystems were synchronized by the TTL output of the X-Y motor controller at each scanning step, which triggered the pulsed laser. The output of the photodiode (PD in Fig.3-1) in response to each laser pulse triggered a multi-channel digital delay generator (DG645, Stanford Research Systems). One output channel of the delay generator triggered the digitizer for acquisition of the PAM and CFM signals. Another output channel triggered a function generator (AFG3021B, Tektronix), the output of which was used to trigger the image acquisition board for the CCD camera of the spectrometer. The function generator worked in a burst mode: with each trigger received it generated four pulses to drive the OCT system to acquire four depth scans with an A-line rate of 24 kHz. These four depth scans were used to calculate the phase shift caused by the blood flow, thus generated the ODT images.

A microscope formed by an imaging lens (L2 in Fig 3-1, f = 200 mm) and the objective lens was used to guide the alignment of the sample for imaging. The microscope was coupled in the optical path by a pellicle beam splitter and the image was detected with a CMOS camera.

3.2.2 Imaging System Performance

The axial resolution of the OCT subsystem was mainly determined by the center wavelength and bandwidth of the broadband light source. When imaging biological tissues,

we only used 50 nm bandwidth and the measured depth resolution was 7.5 μm in air, which was a bit worse than the theoretical value of 6 μm. The axial resolution of the PAM subsystem was quantified by measuring the FWHM of the averaged PA pulse echoes envelope generated from a black tape. The PAM depth resolution was measured to be 31 μm.

Although the lateral resolution of the OCT and PAM is determined by the numerical aperture of the objective lens and the wavelength (theoretically: 2.5 μm and 3.8 μm for PAM and OCT, respectively), the lateral resolution of the current multimodal imaging system is limited by the step size of the mechanical scanner which is 6.4 μm for both OCT and PAM. The performance of the ODT has also been validated before with phantoms [101].

3.2.3 OCT-guided Dynamic Focusing

To achieve dynamic focusing, the relationship of the optical focus of the objective lens versus depth is established by imaging a black tape as the sample. The focus of the objective lens corresponds to the highest photoacoustic signal. When the highest photoacoustic signal is detected, the surface of the tape measured by OCT is defined as the depth location of the focus of the objective lens. This procedure resets the working condition of the imaging system. When imaging a biological subject, we first adjust the sample to get the highest photoacoustic signal at a reference point, which is selected with the guidance of the real-time video image and the PAM B-scans. The surface of the sample at the reference point, measured by OCT, is defined as the depth reference for the following scans. The depth adjustments for the objective lens at the following scan positions are

determined by the depth difference of the sample surface with the reference. Thus, the dynamic focusing is designed to follow the contour of the sample detected by OCT.

Before imaging, the area of interest of the subject was first imaged by the OCT system. A rapid OCT B-scan consisting of 256 A-lines was acquired in the X-direction. The contour of the subject along the scanned path was then extracted automatically by using a self-developed LabVIEW program.

3.2.4 Sample Preparation in Phantom, Ex Vivo and In Vivo Experiments

The multimodal imaging system was validated by imaging various samples including phantom, biological tissues ex vivo, and mouse ear in vivo. All experimental animal procedures were conducted in compliance with the guidelines of the Florida International University's Institutional Animal Care and Use Committee.

We first tested the performance of the OCT-guided dynamic focusing by imaging a rectangular capillary tube (dimensions: 0.1 mm path × 1 mm width × 0.09 mm wall) filled with fluorescent micro-particles (FluoSphere polystyrene, 1.0 μm, Ex: 540 nm, EM: 560 nm, Thermo Fisher Scientific). Then, we imaged the retinal pigment epithelium (RPE) of a human cadaver eye to demonstrate the capability of the PAM, OCT and CFM subsystems. A piece of the human cadaver eye was cut from the eyeball and the retina was removed to expose the RPE. The sample was fixed on a holder plate and was immersed in water for imaging.

A mouse ear was imaged in vivo to further demonstrate the full potential of the quad-modal OCT/ODT/PAM/CFM system and also test the OCT-guided contour scanning method. The

animal was anesthetized by intraperitoneal injection of a cocktail containing ketamine (54 mg/kg body weight) and xylazine (6mg/kg body weight). Then, the hair was gently removed from the ear by using a commercial hair removal gel. A small amount of acoustic coupling gel was applied on the mouse ear. The mouse was restrained in an animal mount at 20-degree angle.

3.2.5 Reducing the Nonlinear Effect in Optical Fibers

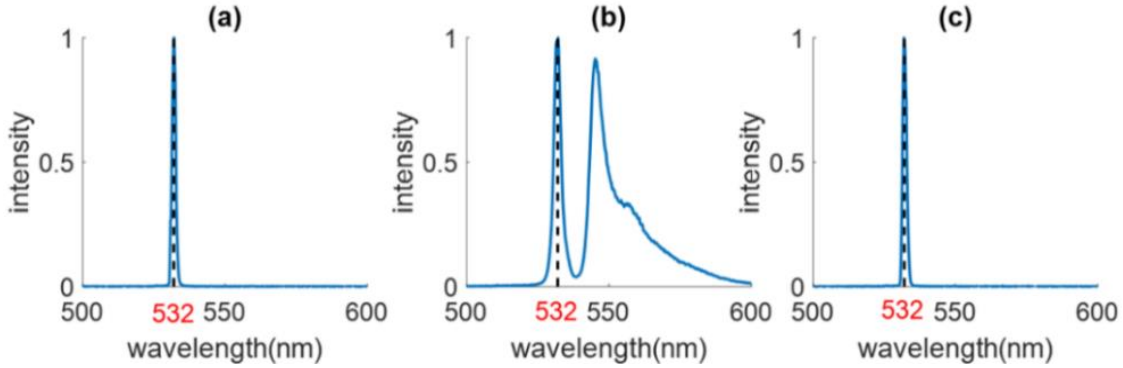

Figure 3-2 Measured optical spectrum of the pulsed laser before and after the single-mode optical fibers. (a) laser spectrum before the optical fiber; (b) laser spectrum exiting a 4.5 m long single-mode optical fiber; (c) laser spectrum exiting a 0.5 m long single-mode optical fiber. The intensity readings are normalized.

Long optical fiber was frequently used to increase the distance between the pulsed laser and the PAM detection units to avoid electrical interference from the laser driving circuits. Reducing the nonlinear effect of the single-mode optical fiber is important for fluorescence imaging to avoid overlap of the shifted illuminating spectrum with that of the fluorescence. The spectral shift caused by the nonlinear effect will affect the accuracy of quantitative absorption measurement in PAM, e.g., in blood vessel oximetry. We measured the spectrum of the 532 nm laser light before coupled into and after exiting the single-mode optical fiber. When the fiber length was 4.5 m, we observed that the peak wavelength was shifted from 532 nm (Fig. 3-2(a)) to 545 nm (Fig. 3-2(b)) due to Raman scattering in the

single mode fiber. One solution to this issue is to add a 532 nm laser line filter at the exit of the optical fiber to filter out the shifted longer wavelengths. However, this led to a drop in laser energy, in the 4.5 m fiber case from about 600 nJ to 200 nJ. Another solution is to shorten the optical fiber. When we shortened the fiber length from 4.5 m to 0.5 m, the nonlinear effect is significantly reduced. As shown in Fig. 3-2(c), in the spectrum of the laser light exiting the 0.5 m fiber, the wavelength shift can be neglected.

3.3 Results

3.3.1 OCT-guided Dynamic Focusing: Phantom Study

The rectangular capillary tube was fixed on a 20-degree angled plate. To get the contour of the sample surface, the phantom was first scanned at each Y location with the OCT system along the X-axis, which consists of 256 A-lines covering a range of 1.6 mm. Fig. 3-3(a) shows one OCT B-scan at the location marked with a yellow line in Fig. 3-3(e). The contour of the phantom was automatically generated by extracting the maximum of each OCT A-line in the B-scan image. The depth difference was calculated at each point on the X-axis in relative to the predefined depth of the maximum PAM signal. The depth difference was used to adjust the focus of the objective lens point by point to achieve dynamic focusing when the multimodal images were acquired.

Fig. 3-3 shows the effect of dynamic focusing on imaging the phantom. Fig.3-3 (c) and (d) show the PAM and CFM images before application of dynamic focusing. Fig.3-3 (e) and (f) shows the PAM and CFM images with dynamic focusing. We can see that after application of dynamic focusing, both the signal intensity and the sharpness of the PAM and CFM images are improved across the field of view. To further illustrate the

improvement of image quality by the OCT-guided dynamic focusing, we draw the signal intensities of the PAM and CFM (Fig.3-3 (g) and (h)) along the line shown in Fig. 3-3(c), (d), (e) and (f). In the PAM and CFM intensity curves the signal intensities at all the imaged points are significantly improved after the application of dynamic focusing except the points already in focus (the points in the dashed box).

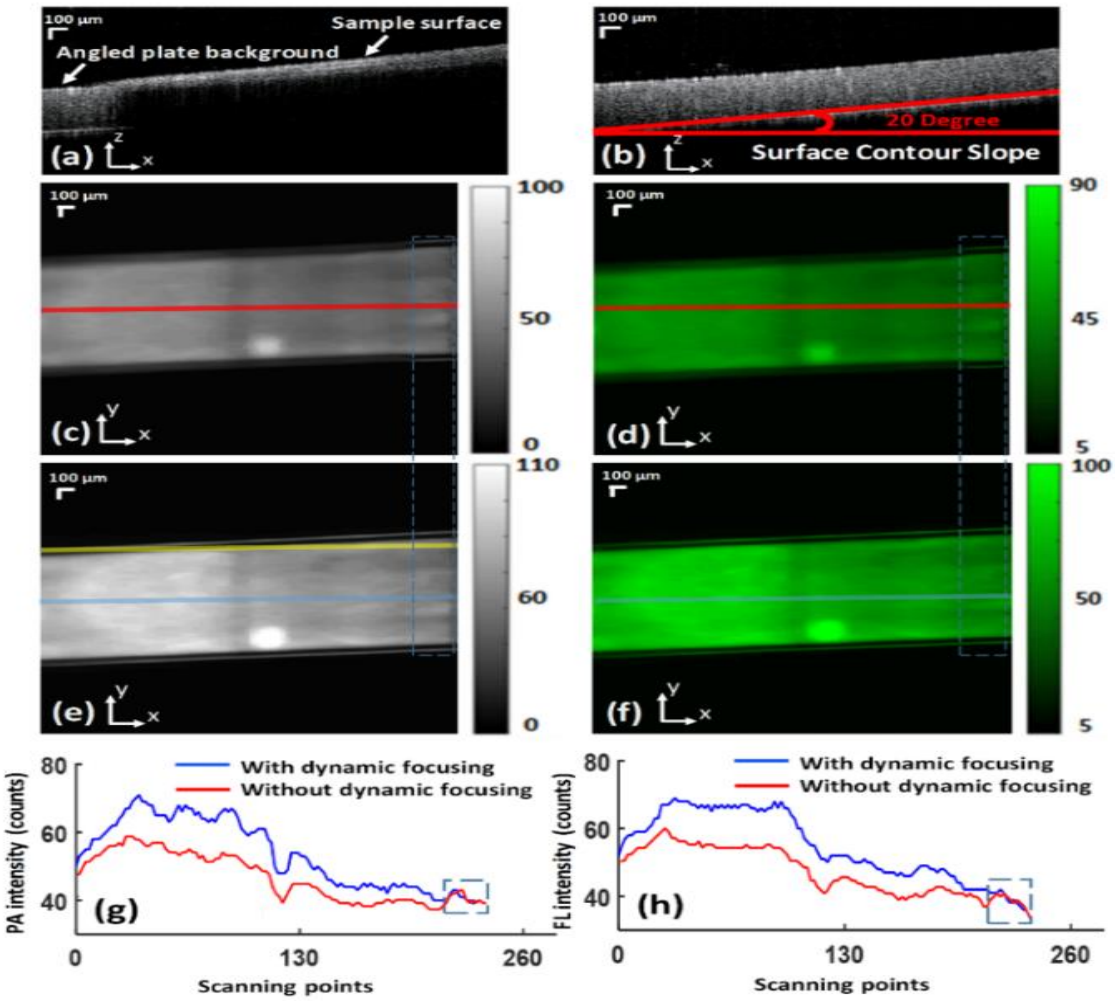

Figure 3-3 Phantom test of OCT-guided dynamic focusing using surface contour scanning. (a) OCT B-scan at the location marked in panel (e) as a yellow line; (b) OCT B-scan of the angled plate; (c) and (d) Simultaneously acquired PAM and CFM images without dynamic focusing; (e) and (f) Simultaneously acquired PAM and CFM images with dynamic focusing; (g) PA signal intensity along the line at the location marked in panel (c) and (e) as a red and blue line without and with dynamic focusing, respectively; (h) FL (fluorescence) signal intensity along the line at the location marked in panel (d) and (f) as a red and blue line without and with dynamic focusing, respectively; bar: 100μm.

3.3.2 OCT-guided Dynamic Focusing: Ex Vivo Simultaneous PAM, CFM and OCT Imaging

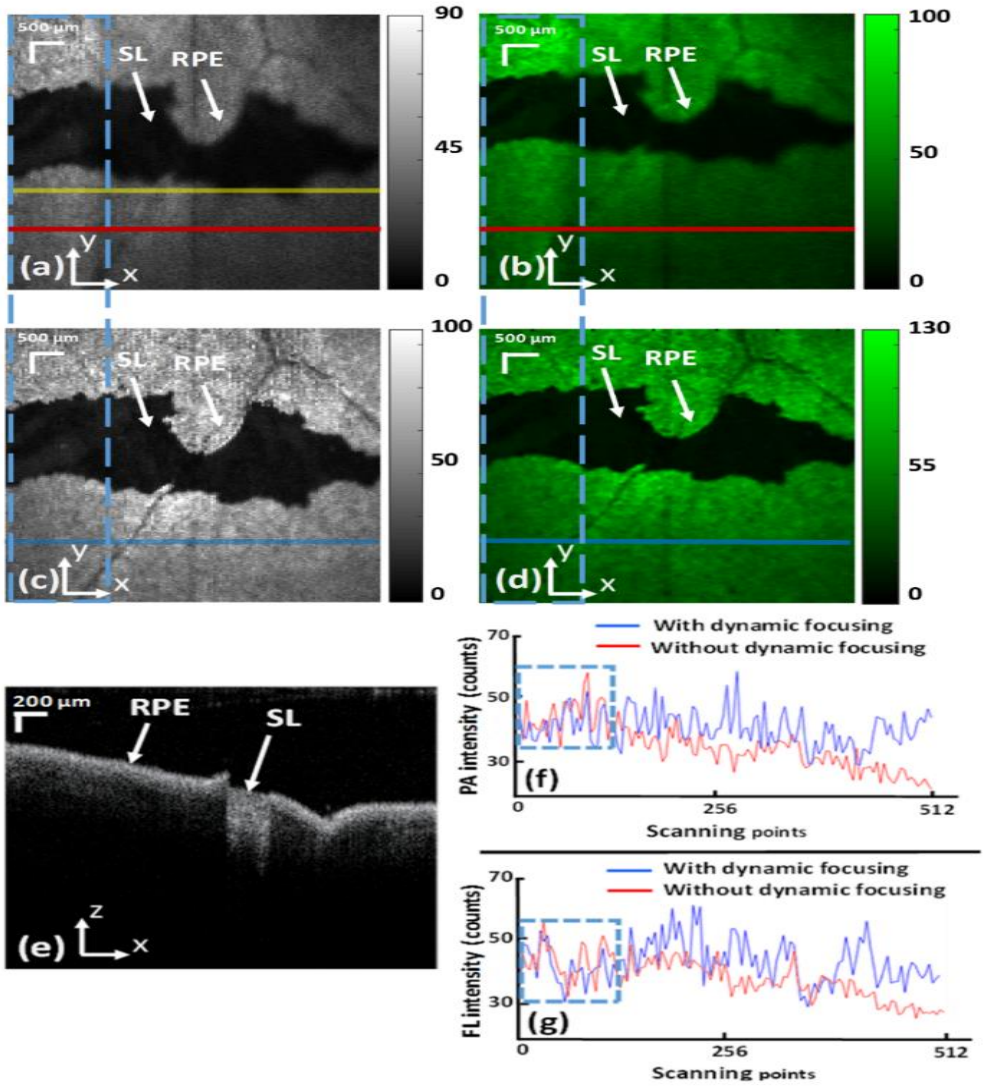

Figure 3-4 Multimodal imaging of a human eye ex vivo using OCT-guided dynamic focusing. (a) and (b) Simultaneously acquired PAM and CFM images without dynamic focusing; (c) and (d) Simultaneously acquired PAM and CFM images with dynamic focusing; (e) OCT B-scan at the location marked in panel (a) by the yellow solid line (displayed dynamic range, 55 dB); (f) PA signal intensity along the line at the location marked in panel (a) and (c) as a red and blue line without and with dynamic focusing, respectively; (g) FL (fluorescence) signal intensity along the line at the location marked in panel (b) and (d) as a red and blue line without and with dynamic focusing, respectively; RPE: Retinal Pigment Epithelium; SL: Sclera; bar, 500 μm.

After successful test on the phantom, we imaged the retinal pigment epithelium (RPE) of a human cadaver eye with the multimodal imaging system to test the performance of OCT-guided dynamic focusing on biological samples. Before data acquisition, the real-time OCT signal was used to guide moving the sample to the focal plane. The microscope was used to locate the region of interest (ROI). Before image acquisition, the same procedure was followed to extract the contour of the sample surface by using the OCT scan. Dynamic focusing was then applied, point by point, during image acquisition.

The performance of the OCT-guided dynamic focusing is demonstrated in Fig. 3-4. The simultaneously acquired PAM and CFM images were composed of 512 × 512 scanning points covering an area of 6.5 mm × 6.5 mm. The PAM images shown are a maximum-amplitude-projection (MAP) of the acquired 3D data. In the CFM images each pixel is an average of the acquired 1000 samples at each scanning point. The imaging time is about 80 minutes. Fig. 3-4(a) and (b) show the PAM and CFM images of the sample without dynamic focusing. Fig. 3-4(c) and (d) show the PAM and CFM images of the same area with dynamic focusing. Fig. 3-4(f) and (g) show the intensity of the PAM and CFM signals along the line marked in the corresponding images. The unevenly distributed melanin and lipofuscin granules in the RPE cells give rise to the spike appearance of the PAM and CFM signals. We can clearly see the improvement of the signal intensity and the sharpness of both the PAM and the CFM images by applying dynamic focusing.

Fig. 3-4 demonstrates the complementary molecular contrasts provided by the multimodal imaging system. The signals in PAM and CFM were generated by melanin and lipofuscin in the RPE, respectively, which can be verified by the OCT cross-sectional image shown

in Fig. 3-4(e), the location of which is marked in Fig. 3-4(a) by the yellow solid line. In the OCT image, we can clearly see that the dark regions in the PAM and CFM images correspond to the area deprived of RPE layer. Since both PAM and CFM were generated with the same group of photons, both images are intrinsically registered. The images of the two modalities look similar because both melanin and lipofuscin granules are all contained in the RPE cells and the resolution of the current system is not good enough to separate them.

3.3.3 In Vivo Simultaneous PAM, CFM, OCT and ODT Imaging with OCT-guided Dynamic Focusing

We imaged a mouse ear in vivo to demonstrate the full potential of the multimodal imaging system with dynamic focusing. After sample preparation, the mouse was restrained in a homemade 20-degree angled plate, which was fixed on the Z-axis platform. By placing the ear at an angle, the blood vessels were not perpendicular to the OCT probe light thus guaranteed that the Doppler angle would not be 90°. The mouse ear was then attached to the imaging window of the water tank. Using the Z-axis stage, the sample was adjusted to the focal plane by monitoring the OCT signal in real time. We could visually identify the ROI by using the microscope camera. The procedure for extracting the contour of the sample by using the OCT B-scans and adjusting the focus of the objective lens to achieve dynamic focusing was the same as in the phantom and ex vivo experiments. The entire image acquisition took about 20 minutes covering an area of 1.6 mm × 1.6 mm. The size of the imaging area was limited by the time limit of the anesthesia method.

Fig. 3-5 shows the simultaneously acquired PAM, CFM, OCT and ODT images of the sample to demonstrate the full potential of the multimodal imaging technique with OCT-

guided dynamic focusing. Each imaging subsystem reveals significantly different features of the mouse ear due to their different contrast mechanisms. The PAM image in Fig. 3-5(a) clearly imaged the blood vessels because hemoglobin in the red blood cells in the vessels has high optical absorption at 532 nm. Fig. 3-5(b) shows the OCT B-scan image at the location marked in Fig. 3-5(e), which revealed the tissue structures, including the epidermis, dermis, and the articular cartilage.

Fig. 3-5(c) shows a cross-sectional ODT image indicating directional blood flows. Red and blue colors represent direction of blood flow corresponding to arteries and veins, respectively. Two vessels, one artery and one vein were captured. The artery and vein were identified due to the fact that veins have typically larger lumen with thinner wall, transporting more blood volume, while arteries are smaller in diameter with thicker wall in proportion to their lumen. In addition, arteries and veins typically appear as a pair in tissue. Depending on the imaging configuration and the scanning direction on the animal, we can also distinguish arteries from veins according to the direction of the blood flow: arteries transport high pressure blood from the heart to smaller arteries in different organs and veins carry low pressure blood from venules to the heart [102]. At each scanning location, the depth-resolved phase differences among the four OCT A-lines were calculated by using the previously reported methods [103,104]. Briefly, the projected flow speed on the direction of the incident sample light can be calculated from the phase difference among the adjacent A-lines $\Delta\varphi_i = \varphi_{i+1} - \varphi_i$, where i is the A-line number:

$$v_p = \frac{\Delta\varphi_i \lambda_0 f_{A-line}}{4\pi n}, \quad (1)$$

where v_p is the projection of the absolute velocity v_a along the depth direction, λ_0 is the center wavelength of the light source, f_{A-line} is the axial scan frequency (A-line rate), n is the index of refraction of the sample.

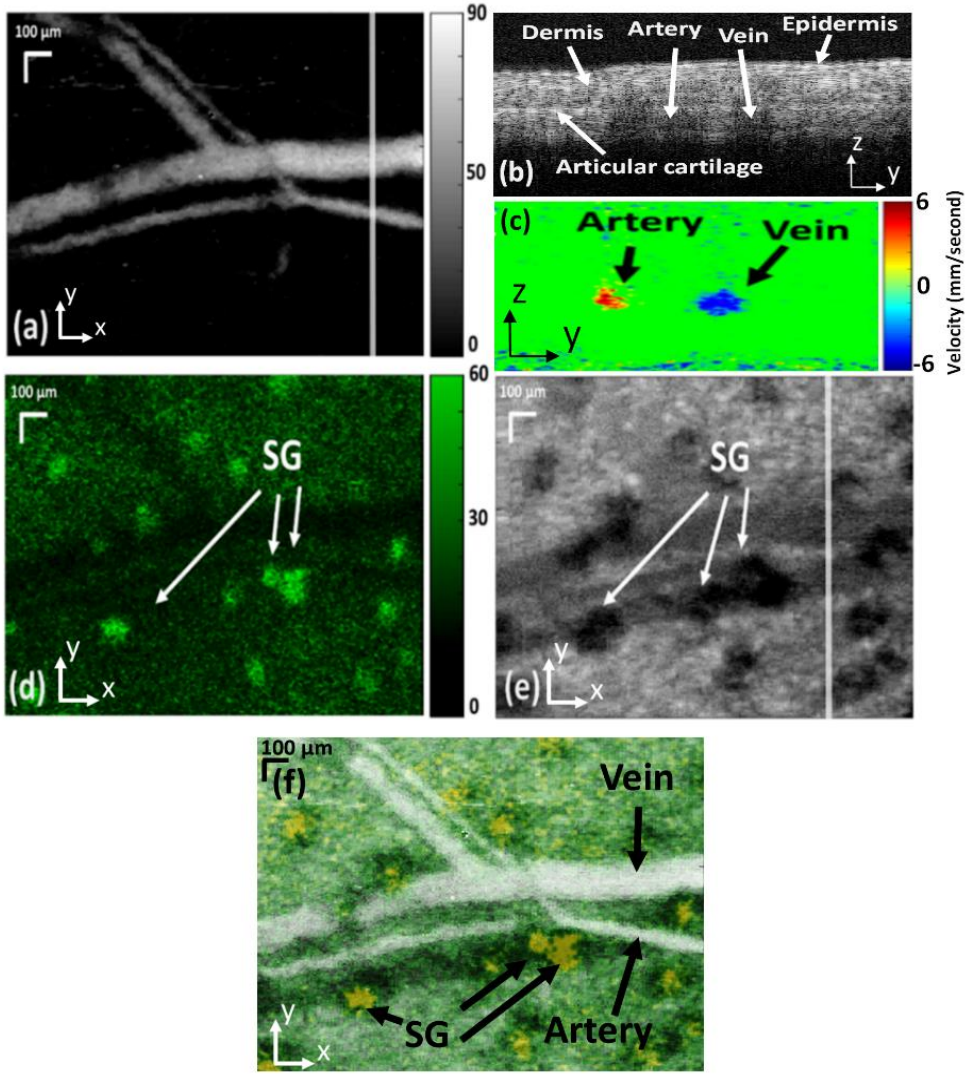

Figure 3-5 Simultaneously acquired PAM, CFM, OCT and ODT images of a mouse ear with dynamic focusing. (a) PA image (average contrast-to-noise ratio 50 dB); (b) OCT B-scan at the location marked in panel (e) by the solid line (displayed dynamic range, 45 dB); (c) ODT B-scan at the location marked in panel (e) by the solid line; (d) CFM image (average contrast-to-noise ratio 30 dB); (e) OCT 2D projection images generated from the acquired 3D OCT datasets; (f) Fused 2D image of simultaneously acquired PAM, CFM and OCT images; SG: Sebaceous glands; bar, 100μm.

Fig. 3-5(d) shows the fluorescence of the sebaceous glands in the skin. Several different molecules, such as porphyrins, keratin and tryptophan, are the possible sources for autofluorescence in sebaceous glands [105,106]. Fig. 3-5(e), shows a projection of the 3D OCT data on the X-Y plane [107]. The sebaceous glands appear dark in the projected OCT images due to the shadowing effect as shown in the OCT B-scans. Fig. 3-5(f) illustrates the fused image merging simultaneously acquired PAM, CFM and OCT images in a single shot. In PAM images, the blood vessels appear as bright color due to the high optical absorption of hemoglobin at wavelength of 532 nm in blood generating strong ultrasonic signals. In contrast, the blood vessels appear as dark color in the projected OCT image due to the shadowing effect caused by the highly scattering properties of the blood cells.

3.4 Discussion

We have successfully implemented a novel OCT-guided dynamic focusing technique in an integrated multimodal imaging system. The system was tested by imaging phantom, human eye ex vivo, and mouse ear in vivo. Taking advantage of high depth resolution of OCT, the depth information of each scanning point, in reference to the maximum amplitude of PAM signal, was extracted and utilized for dynamic focusing by using a motorized Z-stage. Although the improvement of SNR and image sharpness may not be the same for PAM and CFM when the highest PA signal may not be located in the same plane as that of the highest fluorescence signal, dynamic focusing will make the SNR more uniform across the imaging area. The adjustments of the objective lens in the Z direction should be recorded and saved to a file, which will be needed for reconstructing the 3D CFM image when optical sectioning is performed. Upon development of this novel method, which maintains

the sample at focus through the entire scanning, images with higher SNR can be acquired. This novel technique is suitable for imaging different samples with uneven surfaces.

Currently, the major limitation to the multimodal imaging system is the imaging speed, which is limited by the scanning speed of the step motors. To increase the imaging speed, a faster motor or different scanning mechanisms is needed, which is one of our focus in developing the system into more practical applications. Limited imaging depth of the OCT system, 2 mm for the current OCT system, may be another limitation for the dynamic focusing applications.

The digital delay generator plays a key role in synchronizing the imaging systems. The A-line rate of the OCT system is determined by the scanning motor while the A-line rate for ODT calculations is determined separately by the pulse repetition rate of the function generator. This arrangement assured that at each scanning position multiple depth-scans can be acquired, which decoupled the A-line rate for ODT from the scanning speed of the motor and made the ODT function possible. During the in vivo experiments, we found that the blood flow imaging was not always successful. We hypothesize that the pressure of the water tank on the sample may slow down the blood flow to the extent that exceeds the limit of the ODT measurement. We did not see capillaries in the PAM and ODT images of the mouse ear because ODT is not sensitive enough for capillary imaging due to the slow blood flow in capillaries. Since we imaged the lower part of the ear, there were possibly less capillaries to be captured around the arteries and veins in PAM image. This could also be due to the relatively low sensitivity of the unfocused needle transducer. A better transducer with higher sensitivity will be considered for the future work.

In the current CFM imaging the fluorophores providing the contrasts were lipofuscin in the RPE cells and porphyrins in the sebaceous glands, both are endogenous fluorophores. Lipofuscin is a complex lipid/protein aggregate of nondegradable end products from phagocytosis of shed photoreceptor outer segments in the RPE. It is the major source of fundus autofluorescence and it accumulates with age. The accumulation of lipofuscin in the RPE is believed to contribute to the pathogenesis of retinal diseases such as age-related macular degeneration (AMD) and Stargardt diseases [108-110]. Porphyrins in the sebaceous glands in the mouse ear are attached to individual hair follicles containing viscous fluid called sebum, which is responsible for moisture balance in the mouse skin [105]. By comparing the images of the sebaceous glands, we can see that they are highly optical absorbers in the NIR in comparison with the surrounding tissues because they cast shadows in the OCT cross-sectional image and appear dark in the OCT projection images. Most of the absorbed photons by the sebaceous glands in the visible spectrum, however, may not be converted to heat because they do not contribute to photoacoustic signals. Since they showed up in the CFM image, we can conclude that the absorbed photons in the visible spectrum were mainly converted to fluorescence. These are just examples for demonstrating the potentials of the multimodal imaging system.

For many biological applications, such as understanding the spatial heterogeneity of disease or monitoring of developmental process, the ability to simultaneously capture cellular and whole-organism level processes as well as their mutual interactions is necessary [111]. The proposed imaging system has potential to be used for in vivo retinal imaging, where the contrasts of all the different imaging modalities are provided by

endogenous agents such as, melanin, lipofuscin, scattering, and blood flow. We currently only target the autofluorescence with endogenous fluorophores. The system is also suitable for imaging exogenous fluorophores when the fluorescence probe has correct excitation and emission spectrum. There is also a possibility to replace the CFM with multiphoton microscopy by using an ultrafast Ti:sapphire laser as the excitation light source. In this case, the OCT and multiphoton microscopy can share the same light source. This will be our next step for improving the capabilities of the imaging system. More applications will also be explored as the technologies are being further developed and matured.

3.5 Conclusion

In conclusion, we have successfully developed a multimodal imaging system with OCT-guided dynamic focusing, which can simultaneously acquire OCT, ODT, PAM and CFM images with complementary contrasts. The novel OCT-guided dynamic focusing enabled imaging samples of uneven surface with improved SNR across the whole imaged area. The imaging system was validated by imaging phantom and biological samples ex vivo and in vivo. It is expected that further improvement of this optical microscopic instrument will find even broader applications for tissue imaging.

CHAPTER 4 OCT-guided Dynamic Focusing for Combined Optical and Mechanical Scanning Multimodal Photoacoustic Microscopy

4.1 Introduction

Photoacoustic microscopy (PAM) is an emerging biomedical optical imaging technology, which is capable of imaging the optical absorption contrast of biological tissues. PAM-based multimodal imaging technologies combine different imaging modalities to reveal complementary information of biological tissues for potential applications in both research and clinical diagnosis. PAM-based multimodal imaging has been achieved by combining PAM with other microscopic imaging modalities such as optical coherence tomography (OCT), optical Doppler tomography (ODT), confocal fluorescence microscopy (CFM), multi-photon microscopy, or second harmonic generation microscopy [51,56,57,59,112-114]. In these imaging techniques the PAM and other imaging modalities may share the same pulsed light source [54-56,58,61,62].

Field of view (FOV) and imaging speed are two important parameters affecting the application of PAM-based multimodal imaging systems. By using optical scanning and an unfocused ultrasonic transducer, optical-scanning PAM can achieve real-time imaging with an imaging speed depending on the pulse repetition rate of the excitation laser. However, in such configuration the FOV is limited by the field of sensitivity of the fixed unfocused ultrasonic transducer. One method to achieve faster imaging speed and large FOV is to combine optical scanning with mechanical scanning [115].

Focusing of the objective lens is a key for achieving high quality microscopic imaging especially for large FOV. Dynamic focusing is necessary when the contour of the sample surface is uneven and has a range of depth variation in the FOV that exceeds the depth of focus of the objective lens. Without dynamic focusing, the uneven surface of a sample can lead to uneven depth of focus and results in images with non-uniform lateral resolution and signal intensity, which is more significant with increasing FOV. Dynamic focusing has been reported for PAM imaging by using contour scan with PAM [99] or ultrasound [100]. We have achieved OCT-guided dynamic focusing for multimodal PAM imaging and demonstrated the capability by imaging biological samples in vivo [116]. OCT-guided dynamic focusing intrinsically has better guiding accuracy and faster guiding speed due to the better spatial resolution and much faster imaging speed.

To achieve fast imaging and large FOV, we updated our multimodal imaging system, which integrated optical resolution PAM, OCT, and CFM in one platform, by combining optical scanning with mechanical scanning. Optical scanning performs fast scan of the combined PAM excitation laser and the OCT probe light in the FOV of the needle ultrasonic transducer while mechanical scanning moves the imaging subject with a step size defined by the FOV of the transducer. The integrated OCT plays a key role not only for imaging but also for guiding the dynamic focusing to achieve uniform resolution in the combined large FOV. We took a different strategy for dynamic focusing with OCT guidance to match with the faster imaging speed.

4.2 Materials and Methods

4.2.1 Imaging System

A schematic of the experimental system is shown in Fig. 4-1, which is similar to that in chapter 3 except that a pair of galvanometer scanning mirrors (shown in the dashed box in Fig.4-1) was added in the optical systems to achieve fast scanning of the combined near infrared (NIR) and visible light beams across the aperture of the objective lens.

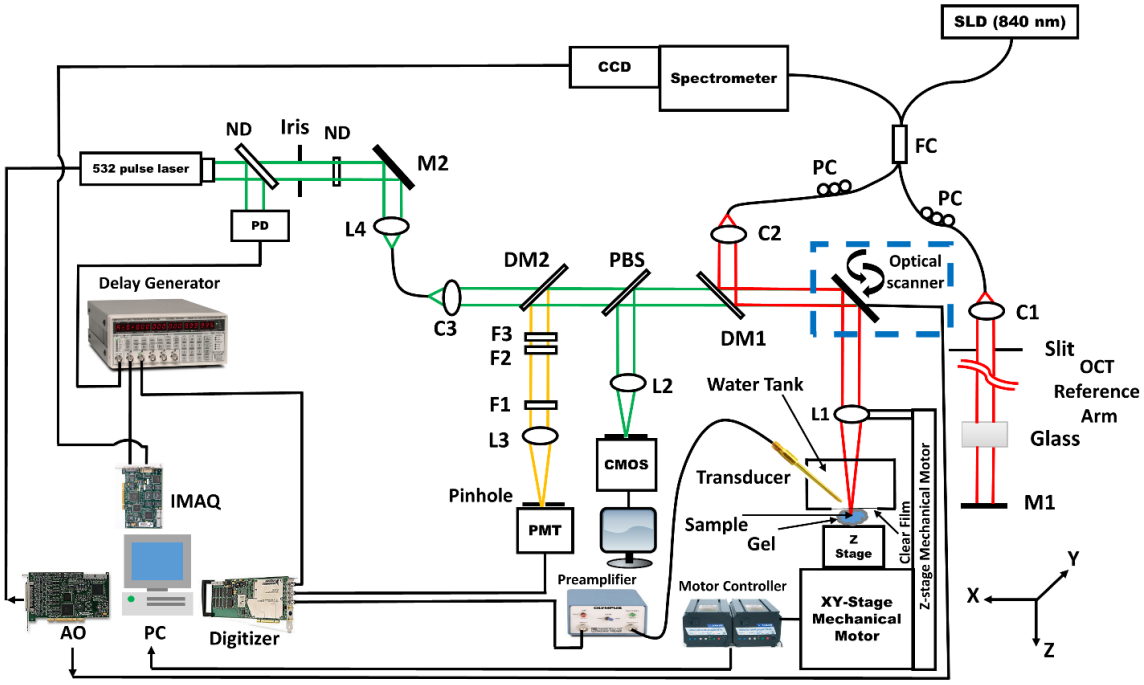

Figure 4-1 Schematic of the integrated PAM/OCT/CFM experimental system. SLD: Superluminescent diode; FC: 2×2 Fiber coupler; PC: Polarization controller; L1, L2, L3, L4: Lens; M1, M2: Mirror; DM1, DM2: Dichroic mirror; C1, C2, C3: Collimator; AO: Analog output; ND: Neutral density filter; F1, F2, F3: Optical filter; PBS: Pellicle beam splitter; PD: Photodiode.

In brief, the system combined PAM, OCT, and CFM for simultaneous multimodal imaging. PAM and CFM shared the same Q-switched frequency-doubled Nd:YAG laser (SPOT-10-200-532, Elforlight Ltd, wavelength: 532 nm, maximum pulse energy: 20 μJ, pulse duration: 2ns, maximum pulse repetition rate: 30 kHz) while the optical fiber-based OCT

used a broadband superluminescent diode-based light source (T-840 Broadlighter, Superlum Diodes Ltd, Ireland). The output pulsed laser was combined with the light beam in the sample arm of the OCT by a dichroic mirror (DM1). The combined light was scanned by the X-Y galvanometer mirrors and focused onto the sample by an objective lens (LMH-5X-532, EFL= 40mm, NA=0.13, Thorlabs). The OCT signal was detected in the spectral domain by a homemade spectrometer. The fluorescence signal was detected by a PMT (PMM02, Thorlabs) with a confocal arrangement through a set of filters and dichroic mirrors, which limited the detection spectrum to 550 nm – 750 nm. The generated photoacoustic signal from the sample was detected by an unfocused needle ultrasonic transducer, which was immersed in a water tank filled with distilled water. The transducer has a center frequency of 30 MHz with an active element diameter of 3 mm. The performances of all the sub-imaging systems are similar to that in our previous publication [116].

We combined optical scanning with mechanical scanning to increase the imaging speed and the FOV. The scanning directions of the galvanometer mirrors are aligned with the mechanical scan. Mechanical scanning was accomplished by using a step-motor-driven platform to move the sample together with the water tank and the ultrasonic transducer in the lateral directions (X and Y). The objective lens was mounted on a Z-scan platform for fine tuning the focus with guidance of the OCT.

All the imaging systems were synchronized by using the sampling clock of an analog output board (AO, PCI-6731, National Instruments), the outputs of which controlled the X-Y galvanometers. At each scanning position of the galvanometers the sampling clock

triggered the pulsed laser, which was partially reflected by a glass plate and detected by a photodiode (PD). The output of the PD triggered a multi-channel digital delay generator (DG645, Stanford Research Systems). One output channel of the delay generator was used to trigger the image acquisition board (PCI-1428, National Instruments) for acquiring the interference spectrum of OCT and another channel was used to trigger the digitizer for acquiring the PAM and CFM signals.

4.2.2 Scanning Scheme and OCT-guided Dynamic Focusing

To achieve large FOV and maximize imaging speed with minimal loss of SNR, the laser and NIR beams are first scanned within the FOV of the ultrasonic transducer (~ 2 mm × 2 mm) by the galvo-mirrors. The sample is then moved to the adjacent imaging area by the mechanical scanning platform. This procedure repeats until the entire region of interest (ROI) of the sample is imaged. At each interval between the mechanical and the optical scanning, the objective lens is adjusted for dynamic focusing. Once the entire ROI of the sample is scanned, all the small images acquired with fast optical scanning are stitched together to form an image of large FOV.

For dynamic focusing we first established the depth relationship between the PAM and OCT by imaging a black tape. The maximum detected photoacoustic signal is achieved when the objective lens is in focus while the OCT image tells the depth of the surface. The relationship of the optical focus of the objective lens with depth can thus be established. In our previous mechanical scanning multimodal imaging system OCT-guided dynamic focusing was applied point by point, i.e., the focus of the objective lens was adjusted for each scanning position. This point-by-point dynamic focusing method is suitable for the

relatively slow mechanical scanning mechanism. For the current fast optical scanning the adjusting speed of the objective lens cannot catch up with the scanning speed. Thus, we adopted an aerial dynamic focusing strategy, i.e., the focus of the objective lens is adjusted area by area.

To achieve dynamic focusing we need to establish a reference focal plane for the objective lens. For biological imaging, we manually adjusted the sample to reach the maximum photoacoustic signal at a reference point, which was selected with the help of the real-time video image and PAM B-scans. The depth location of this reference point is extracted by OCT as a reference for the subsequent scans. In each fast-scanning area, the sample was first imaged with OCT. The depth of the sample surface at each OCT A-line was extracted and the depth position (Z coordinates) was averaged. The difference between this averaged Z position and that of the reference point gives the adjustment range of the objective lens.

We have proved that the mean of the Z coordinates of the scanned sample surface equals the minimum of the mean squared error. The depth positions of the sample surface at each scanning point and the optimal point for focusing adjustment at a fast-scanning area are expressed as Z_s and Z_o, respectively. The sum of the squared error can be expressed as

$$\Delta z^2 = \sum_{m=1}^{M} [z_s(m) - z_o]^2 \qquad (1)$$

Where m is the sequential number of a scanning point and M is the total number of the scanning point in the fast-scanning area. When the optimal depth adjustment is selected for Z_o, we should have $\frac{d\Delta Z^2}{dZ_o} = 0$. We thus have

$$z_o = \frac{\sum_{m=1}^{M} z_s(m)}{M} \quad (2)$$

4.3 Results

The scanning scheme and the performance of dynamic focusing were validated by imaging various biological samples. All experimental animal procedures were conducted in compliance with the guidelines of the Florida International University's Institutional Animal Care and Use Committee.

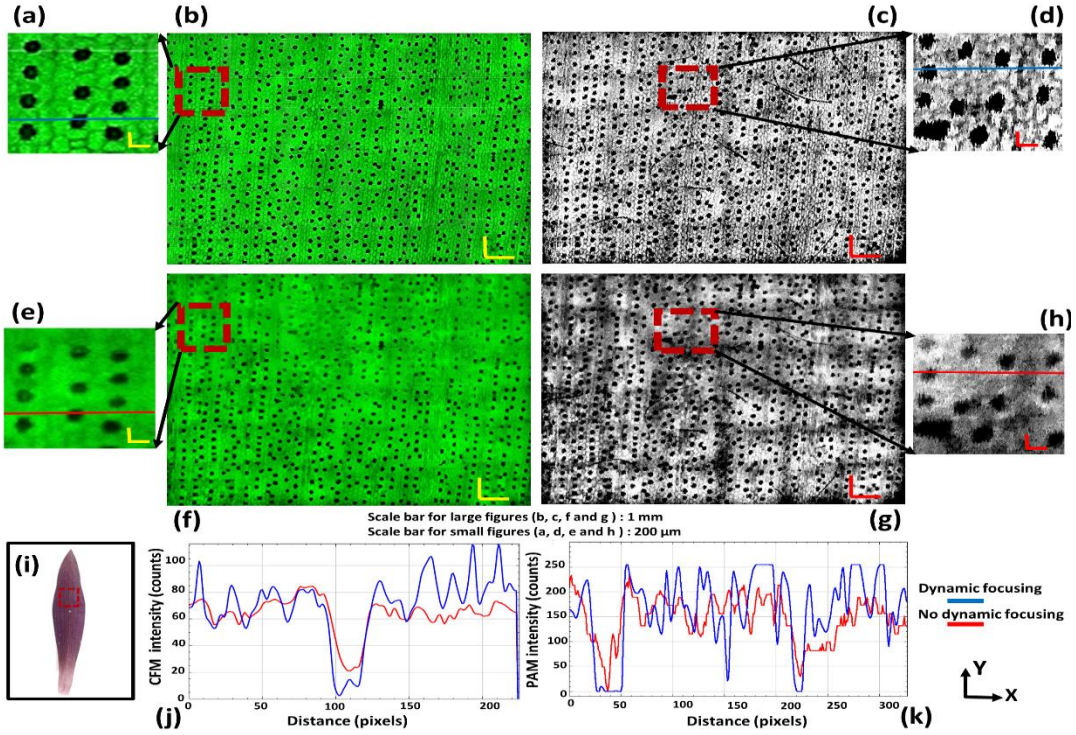

Figure 4-2 Simultaneously acquired PAM and CFM images of a purple queen plant leaf to test the OCT-guided dynamic focusing. (a) Enlarged CFM image with dynamic focusing marked in panel (b) by a dashed box; (b) CFM image with dynamic focusing; (c) Maximum amplitude projection of the PAM image with dynamic focusing; (d) Enlarged PAM image with dynamic focusing marked in panel (c) by a dashed box; (e) Enlarged CFM image without dynamic focusing marked in panel (f) by a dashed box; (f) CFM image without dynamic focusing; (g) PAM image without dynamic focusing; (h) Enlarged PAM image without dynamic focusing marked in panel (h) by a dashed box; (i) A photo of the imaged sample where the selected imaging area is marked by a dashed box; (j) Fluorescence signal intensity along the lines at the location marked in panel (a) and (e) with (blue) and without (red) dynamic focusing; (k) Photoacoustic signal intensity along the lines at the location marked in panel (d) and (h) with (blue) and without (red) dynamic focusing; bar: 1mm and 200µm for large and small figures, respectively.

We first imaged a leaf of purple queen plant as shown in Fig. 4-2. The leaf was selected because of its availability of providing contrasts for all the imaging modalities. It also has abundant structures to provide easy visual judgment about the performance of dynamic focusing. The freshly collected leaf was taped on an aluminum plate and placed under the window of the water tank. Ultrasonic coupling gel was applied between the leaf and the polystyrene film of the window to ensure good ultrasound coupling. The sample was manually adjusted to the focal plane of the objective lens while monitoring the OCT and PAM signals and the reference point was defined for dynamic focusing accordingly. Each fast-imaging area consisted of 512×128 A-lines covering an area of 2 mm × 2 mm contributing to the final large area of 12 mm by 12 mm. The entire image acquisition took about 8 minutes.

Figure 4-2 shows the CFM and PAM imaging results of the leaf with (Fig. 4-2b and c) and without (Fig. 4-2f and g) dynamic focusing. The CFM and PAM images with large FOV of 12 mm by 12 mm consist of 36 small images acquired with fast optical scanning. We montaged the small fast scanning images by using ImageJ. According to the literature the signals in PAM and CFM were generated by anthocyanin and chlorophylls in the leaf structure, respectively. From the enlarged images shown in Fig. 4-2a, d, e and h we can clearly see the improved sharpness of the CFM and PAM images with dynamic focusing. With dynamic focusing, the nuclei and cell walls are clearly seen in the images. In addition, the signal intensity of the PAM and CFM images are significantly improved across the large imaging area. For a direct comparison to show the improvement, we plotted the signal intensities of both CFM and PAM (Fig. 4-2j and k) along the lines marked in Fig. 4-2a, d,

e and h. We calculated the estimated contrast by subtracting the averaged signal intensity inside the cells appeared dark from the averaged signal intensities outside the cells appeared bright for both CFM and PAM. The estimated contrast improvement is 41% and 38% for CFM and PAM, respectively.

We imaged the ear of a Swiss Webster mouse in vivo to demonstrate the full potential of the multimodal imaging system with dynamic focusing for combined large FOV and fast imaging speed. We first anesthetized the animal by intraperitoneal injection of a cocktail containing ketamine (54 mg/kg body weight) and xylazine (6mg/kg body weight). Then, we gently removed the hair from the ear by using a commercial hair removal gel and applied a drop of acoustic coupling gel on the mouse ear. The mouse was restrained in a homemade animal mount, which was fixed on the manually adjustable Z-axis stage (Fig.1). The mouse ear was in contact with the polystyrene film window of the water tank through ultrasonic coupling gel. The sample was moved to the focal plane with the guidance of the real-time OCT. The region of interest (ROI) was selected with the help of the real time microscopic imaging. Following the same procedure for reference point selection and dynamic focusing the sample was imaged with a total FOV of 10 mm × 10 mm which took about 5 minutes for the whole image acquisition.

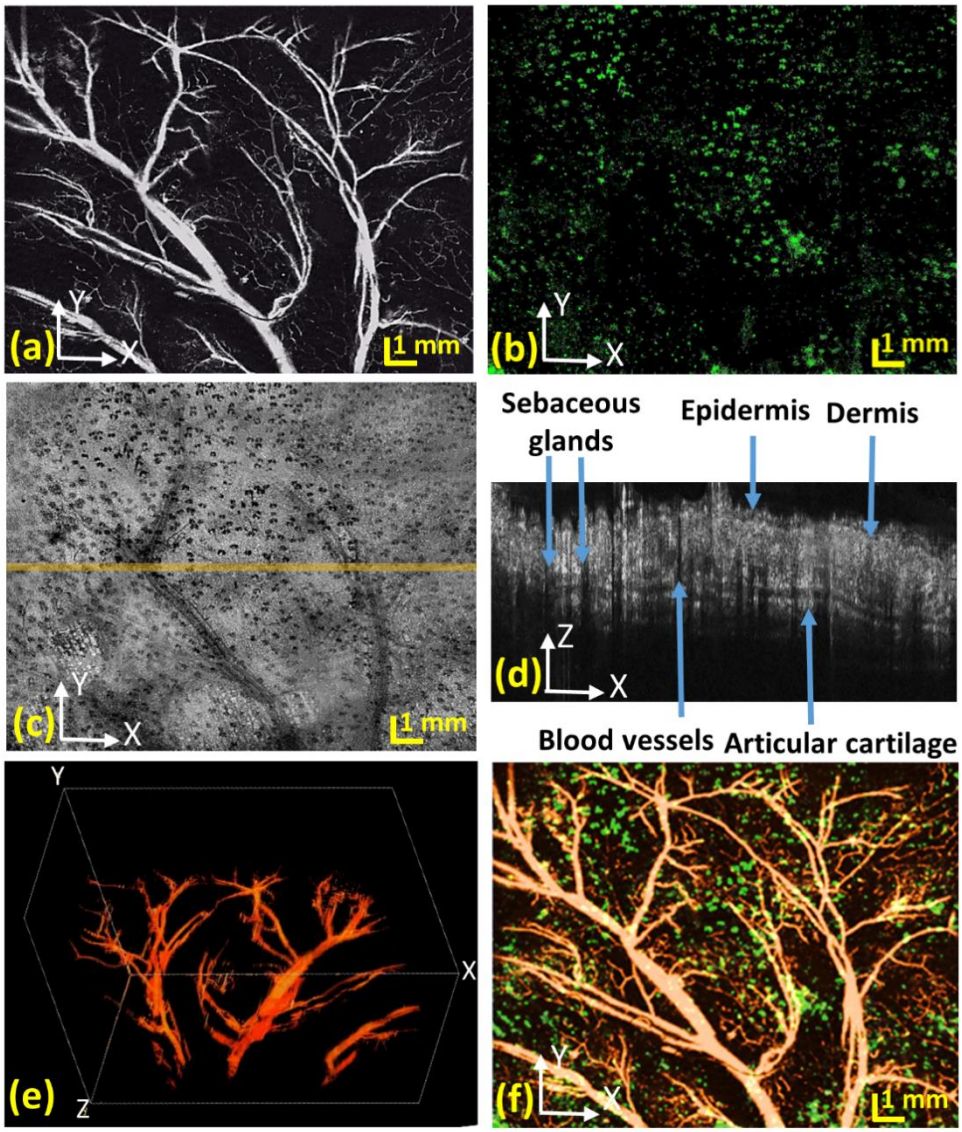

Figure 4-3 Simultaneously acquired PAM, CFM, and OCT images of a mouse ear with dynamic focusing. (a) Maximum amplitude projection of the PAM image; (b) CFM image; (c) OCT projection images generated from the acquired 3D OCT datasets; (d) OCT B-scan at the location marked in panel (c) by a solid line; (e) PAM 3D image reconstruction; (f) Fused PAM projection and CFM images; SG: Sebaceous glands; bar: 1mm.

Figure 4-3 shows the simultaneously acquired PAM, CFM, and OCT images of a mouse ear with OCT-guided dynamic focusing. The images of different imaging modalities revealed complementary features of the mouse ear as a result of the different contrast mechanisms provided. The PAM image in Fig.4-3a clearly reveals the blood vessels, the

imaging contrast of which is provided by the optical absorption of hemoglobin in the red blood cells. Fig.3b displays the fluorescence image, which revealed the sebaceous glands distributed in the ear skin. The possible sources of autofluorescence in the sebaceous glands include porphyrins, keratin and tryptophan molecules [105,106]. Fig. 4-3c shows the *en face* view of the 3D OCT dataset displaying in the X-Y plane. Due to the shadowing effect as shown in the OCT B-scan image (Fig.4-3d), the sebaceous glands appear as black spots in the *en face* OCT display. The OCT cross sectional imaging in Fig.4-3d shows the depth resolved tissue structures. Fig.4-3e shows a 3D reconstruction of the PAM image. Fig.4-3f illustrates the fused image combining simultaneously acquired CFM and PAM images. Thanks to dynamic focusing, the image resolution is uniform across all the large FOV, which is evidenced in Fig.4-3a where capillaries can be recognized in most of the imaged area.

4.4 Discussion

By combining optical and mechanical scanning, we have significantly improved the imaging speed for large FOV imaging. The imaging speed is mainly limited by the pulse repetition rate (PRR) of the PAM excitation laser and the speed of the mechanical scan. Thus, to further improve the imaging speed, a higher PRR laser and a faster scanning motor are needed. Currently, the pulse repetition rate of a commercially available Q-switched laser can reach more than 100 kHz. Such a high PRR laser will greatly improve the overall imaging speed. In the current imaging system, the OCT imaging speed is matched with that of the PAM and CFM. The OCT imaging speed can be easily increased to 100 kHz with a fast CMOS camera used in the spectrometer.

OCT-guided dynamic focusing has enabled uniform focusing of the objective lens across the large FOV. However, there is a possible tradeoff between effective focusing and the fast-optical scanning FOV. In case the contour of the sample surface in the optical scanning FOV has a depth-variation range exceeding the depth of focus of the objective lens, we will need to reduce the area of optical scanning to ensure all points in the optical scanning FOV will be in focus. Thus, to determine the optical scanning FOV an evaluation of the surface condition with OCT may be necessary before acquisition of the multimodal images.

The ultrasonic transducer also plays a key role in determining the PAM imaging quality, the optical scanning range, and thus the overall imaging speed. In Fig.4-3a, we can see that the image has a resolution down to the capillary level. However, not all the capillaries were resolved in the FOV, which is hypothesized to be the result of limited sensitivity of the transducer. The field of sensitivity of transducer limits the FOV of the optical scan. In Fig. 4-2c and g, it appears that the edges of each fast-scanning area have relatively lower intensity, which is caused by the relatively low sensitivity of the ultrasound transducer at the edge of its FOV. One possible solution would be reducing the step size of the mechanical motor creating larger overlap between each fast scanning so that it could compensate the dark edges and make the entire large image more uniform. When a transducer with larger FOV is used the solution should be more feasible. Another solution is to use image processing to compensate for the sensitivity distribution.

The accuracy of surface contour extraction is determined not only by the axial resolution of the OCT but also the surface condition of the sample. As long as the sample surface can provide a clear boundary for OCT imaging there would be no problem for extracting the

depth of the surface at each OCT A-line. Since dynamic focusing is following the contour of the sample surface, we also assume that the targeted tissue structure for imaging, such as the vasculature network, is parallel to the sample surface or the depth variation in reference to the sample surface is less than the depth of focus of the objective lens. This assumption works for the mouse ear sample because we have good focusing across the whole large FOV.

Since only the focus of the objective lens is adjusted and the sample remains stationary in Z- direction during imaging, the three-dimensional (3D) relationship among all the imaging points remains unchanged by dynamic focusing. Thus, 3D reconstruction is not affected by the dynamic focusing process and there is no need for a large-scale alignment between the small images in the montage process. To reconstruct the final large 3D PAM image, we first transferred every small 3D data volume (512 × 128 × 1000) into a single large 3D array (2560 × 640 × 1000) for further image processing. After creating the large 3D array, we extracted PAM vertical (x-z) slices from the time-resolved photoacoustic signal at each depth, similar to the OCT B-scan. Then, each sliced image was enhanced to increase the SNR and reduce the possible artifacts rendering the final volume image by Z-stacking of all (x-z) slices. However, the very small capillaries appeared in Fig. 4-3a still didn't show up in Fig 4-3e due to the low SNR creating noisy environment for 3D reconstruction. Using an ultrasound transducer with higher SNR and also applying more efficient image processing methods will potentially improve the final 3D PAM image in our future studies.

4.5 Conclusion

In conclusion, a combined optical and mechanical scanning multimodal photoacoustic microscopy with OCT-guided dynamic focusing has been developed. The imaging system integrates PAM, OCT, and CFM images with complementary contrasts for multimodal imaging of biological tissues. By combining optical and mechanical scanning, the proposed imaging system has been able to achieve large FOV and high imaging speed. In addition, the novel OCT-guided dynamic focusing has been shown to be able to improve SNR across the entire imaged area of a sample with uneven surface. Ex vivo and in vivo imaging studies were performed and validated the capability of the proposed imaging system.

CHAPTER 5 Integrating Photoacoustic Microscopy, Optical Coherence Tomography, OCT Angiography, and Fluorescence Microscopy for Multimodal Imaging

5.1 Introduction

In the previous chapters, we reported a simultaneous multimodal imaging platform, which integrated PAM, OCT, CFM, and ODT to offer multimodal multi-contrast imaging of biological tissues in vivo. It is necessary to examine each biomarker to pinpoint comprehensive disease-related information for disease diagnosis and research[117,118]. Each of these optical imaging technologies can only provide specific information of biological tissues limited by the optical contrast that each can offer. For instance, the optical contrasts of PAM, OCT, CFM, and ODT are based on different optical properties of biological tissues: optical absorption, back-scattering, fluorescence, and blood flow, respectively. Multimodal imaging techniques [51,62,94,119] can overcome such limitations by providing complementary contrasts for imaging.

In this chapter, we investigate the feasibility of integrating the Optical coherent tomography angiography (OCTA) function to our multimodal imaging platform. OCTA[120-123] is a clinically significant branch of OCT for non-invasive imaging of the microcirculation in vivo. OCTA has been used in preclinical and clinical research for studying various diseases in several medical areas such as dermatology [41], gastroenterology [124], cardiology [125], and neurology [126]. The system is thus able to provide absorption, scattering, fluorescence, Doppler, and motion contrast in one platform.

5.2 Methods

5.2.1 Imaging System

We updated our multimodal imaging system, discussed earlier in chapter 4 for the current study by changing the CCD camera of the OCT spectrometer to significantly increase the OCT imaging speed to a line rate of up to 70 kHz. Fig. 5-1 shows a schematic of the imaging system. In brief, a broadband superluminescent diode-based near-infrared (NIR) light source (T-840 Broadlighter, Superlum Diodes Ltd, Ireland) and a Q-switched frequency-doubled Nd:YAG laser (SPOT-10-200-532, Elforlight Ltd, wavelength: 532 nm, maximum pulse energy: 20 μJ, pulse duration: 2ns, maximum pulse repetition rate (PRR): 30 kHz) were used for OCT/OCTA and PAM/CFM, respectively. The NIR and visible light was combined by a dichroic mirror and scanned together by a X-Y galvanometer scanner. The light was focused onto a sample by an objective lens (Microspot focusing objectives, LMH-5X-532, EFL= 40mm, NA=0.13, Thorlabs). The backscattered NIR light from the sample was collected by the objective lens, combined with the reflected light in the reference arm, and detected in the spectral domain by a home-made spectrometer. To make the system suitable for OCTA we improved the OCT imaging speed by using a fast CCD camera in the spectrometer (Aviiva-EM4-CL-2014, 2048 pixels with 14 μm pixel size operating in 12-bit mode, e2V). The spectrometer used a 1200 lines/mm transmission grating and a multi-element imaging lens (f = 150 mm).

The photoacoustic signal was detected by a 30 MHz unfocused small footprint ultrasonic transducer immersed in a water tank filled with deionized water. The water tank has a window at the bottom sealed with polystyrene film. For PAM imaging the sample was

attached to the window through ultrasound coupling gel. The fluorescence signal excited by the 532 nm laser pulse was also collected by the objective lens and detected by a PMT with the combination of a set of filters and a pinhole.

We combined optical scanning with mechanical scanning to achieve large field of view (FOV). Mechanical scan was accomplished by using a step-motor driven platform (UniSlide, Velmex, Inc.) to scan the sample together with the water tank in the X and Y directions. Dynamic focusing was accomplished by using a motorized stage to adjust the objective lens in the Z direction.

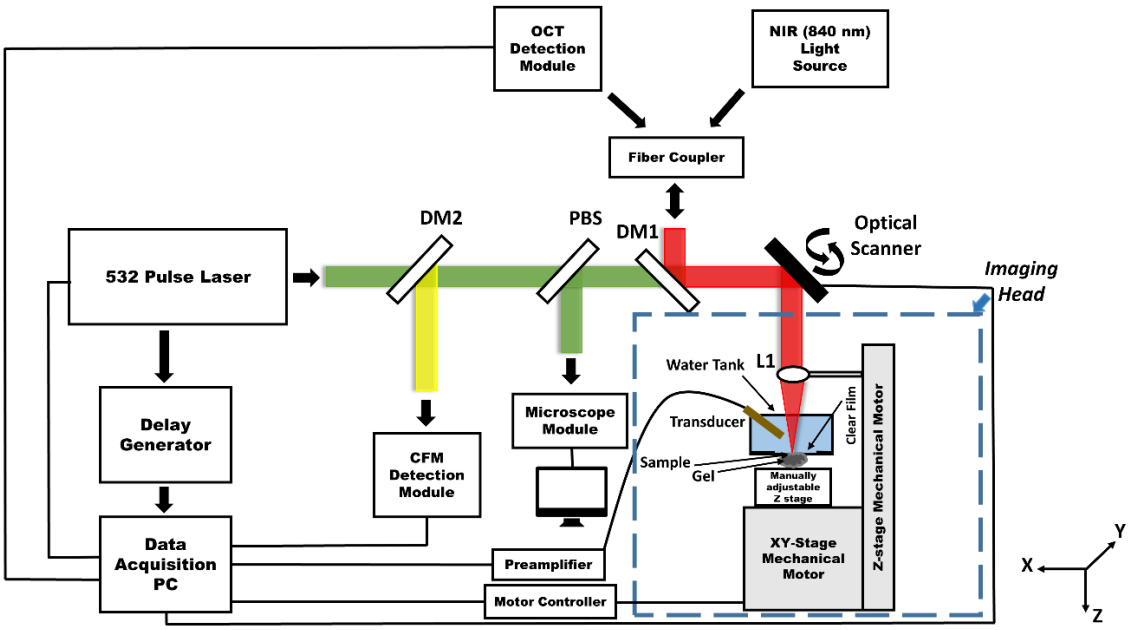

Figure 5-1 Schematic of the integrated PAM/OCT/CFM/OCTA multimodal imaging platform. L1: Objective lens; DM1, DM2: Dichroic mirror; PBS: Pellicle beam splitter.

For multimodal imaging, we performed OCTA separately before or after acquiring the combined OCT, PAM, and CFM images due to the differences of the imaging speed. The maximum imaging speed of PAM and CFM is 24 kHz determined by the PRR of the pulsed laser, which can be improved by using a laser with higher PRR. The performance of all the

sub-imaging systems, including lateral and axial resolutions are the same as reported in Chapter 1.

5.2.2 OCT Angiography Algorithm

For OCTA imaging each cross-sectional scan (B-scan) was repeated 4 times at each spatial location of the sample. Each B-scan consisted of 512 depth scans (A-lines). The scanning rate of 40 kHz was selected for in vivo mouse ear imaging. Over the years, numerous OCTA algorithms were developed [127], which have been successfully applied to different in vivo samples for visualization of the vasculature, such as speckle variance [128], phase variance [129], correlation mapping [130], split-spectrum amplitude-decorrelation [131], and optical microangiography [132]. We used an algorithm similar to the improved speckle-contrast OCTA (ISC-OCTA) [133] to calculate the OCTA signal in the current study. The amplitude of the raw OCT signals was extracted from each of the 4 B-scans and the speckle contrast image k_s was calculated as follows:

$$k_s(x, y_j, z) = \frac{1}{1-N} * \sum_i^{N-1} \frac{|I(x,y_{i+1},z) - I(x,y_i,z)|}{I(x,y_{i+1},z) + I(x,y_i,z)} \quad (1)$$

where N is the total number of the repeated B-scans; $I(x, y_i, z)$ is the signal intensity at i-th B-scan. The final blood flow image was generated [133] as following:

$$I_f(x, y_j, z) = I_s(x, y_j, z) * k_s(x, y_j, z) \quad (2)$$

where I_f is the OCTA flow signal used for the final blood flow image; I_s is the mean of intensity value of the 4 consecutive B-scans; The ISC-OCTA method helps suppressing the noise due to background noise and bulk motion enhancing the blood flow signal.

5.3 Results

We validated the performance of the proposed multimodal imaging system by imaging a mouse ear in vivo. We first imaged a large area of a mouse ear by using the combined optical scanning with mechanical scanning to demonstrate the capability of the OCTA function with large FOV. All animal procedures were conducted following the protocol approved by the Florida International University's Institutional Animal Care and Use Committee.

Figure 5-2 shows the OCTA image of a mouse ear with a FOV of 12 mm × 12 mm. Before imaging, the mouse was anesthetized by intraperitoneal injection of a cocktail containing ketamine (54 mg/kg body weight) and xylazine (6mg/kg body weight). Then, the animal was restrained in an animal mount secured on the manually adjustable Z-axis stage, which was mounted on the X-Y motorized stage. The NIR light was scanned within the aperture of the objective lens by the fast galvanometer scanner to acquire the OCT signals for OCTA imaging. The sample was then moved to the neighboring imaging area by the mechanical scanner. This procedure was repeated until the entire region of interest (ROI) was imaged. Each fast-imaging area consisted of 512×128 A-lines covering an area of 2 mm × 2 mm contributing to the final large FOV of 12 mm × 12 mm. The entire image acquisition took about 9 minutes. The OCTA images of all the fast scanned areas were stitched together to generate the final image.

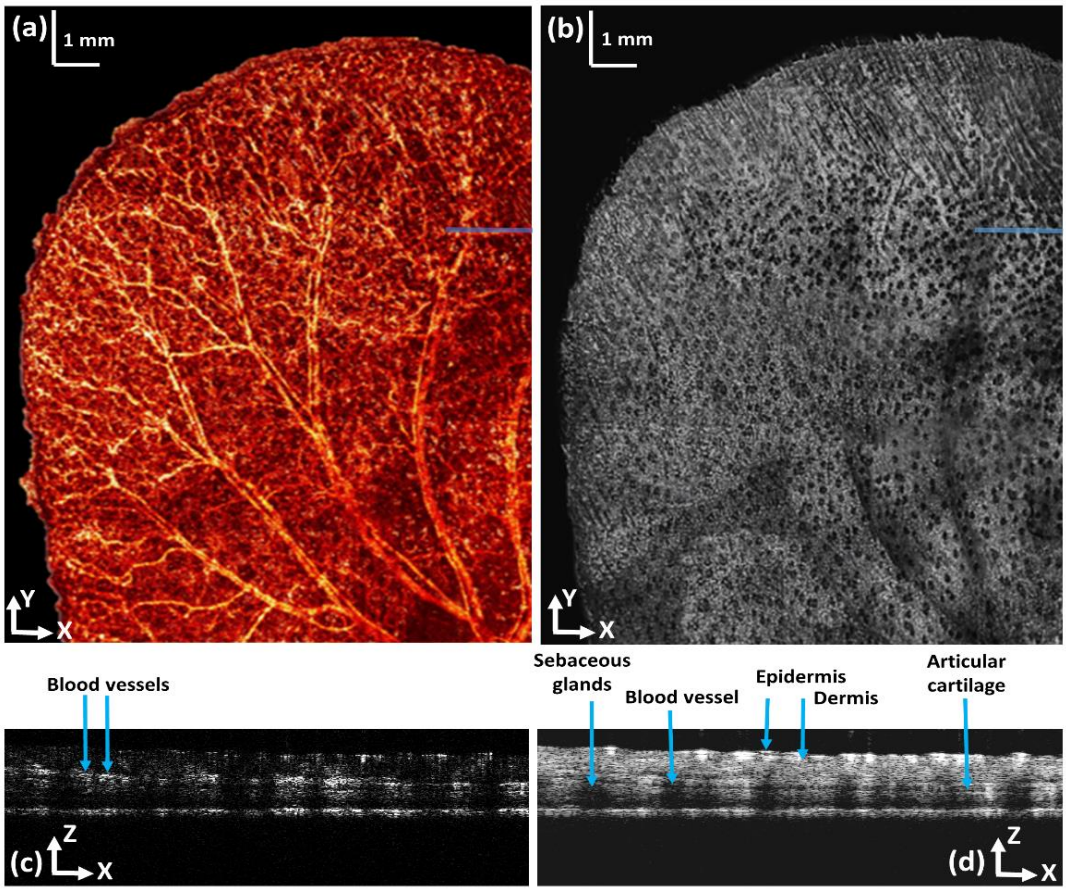

Figure 5-2 OCTA image of a mouse ear. (a) En face projection of the OCTA image; (b) OCT projection image generated from the acquired 3D OCT dataset; (c) Cross-sectional OCT blood flow image at the location marked in panel (a) by a solid line; (d) OCT B-scan at the location marked in panel (b) by a solid line; bar; 1 mm.

Figure 5-2a displays the *en face* view of the large FOV OCTA image of the mouse ear. We can see that both the large vessels and the small capillaries were clearly revealed over the entire imaging area. Fig. 5-2b shows the projection of the 3D OCT dataset in the X-Y plane, which shows clearly the different features compared to the OCTA image demonstrating the different contrast mechanisms. We can see that the sebaceous glands appear as black spots in the image due to the shadowing effect as shown in the depth-resolved OCT B-scan image (Fig. 5-2d), which shows the tissue structure. The OCTA signal is displayed in Fig. 2c revealing the blood flow separated from the stationary background tissue.

After successful OCTA imaging of the mouse ear with large FOV, we performed *in vivo* multimodal imaging on a different mouse ear to demonstrate the capability of the multimodal imaging system providing complementary information of living tissue. Before imaging, we followed the same sample preparation standards [116,134] for anesthesia, animal fixation, hair removal and acoustic coupling gel application. Using the guidance of the real time microscope, integrated in the multimodal imaging system, we visually selected the ROI and moved the animal to the focal plane of the objective lens, which corresponds to the maximum PAM signal, the same procedure used for dynamic focusing in our previous studies [116,134]. We only imaged a small area of 2 mm × 2 mm, limited by the small FOV of the ultrasonic transducer, with the fast-optical scanning.

We first scanned the ROI with PAM, OCT, and CFM at an imaging speed of 24 kHz, which took about 4 seconds, and then OCTA imaging was performed on the same ROI at an imaging speed of 40 kHz taking about 3 seconds. The OCTA was performed separately due to the limited PRR of the pulsed laser and the different scanning pattern which repeated each B-scan 4 times at each location.

Figure 5-3a shows the PAM image of the mouse ear revealing the vasculature network in the tissue. The blood vessels appear bright due to the high optical absorption of hemoglobin in the red blood cells at 532 nm generating strong ultrasound signal. Fig. 5-3b demonstrates the *en face* view of the OCTA image of the same imaged area. The blood vessels including the small capillaries appear bright in the OCTA image due to the specific imaging contrast mechanism that OCTA provides separating the flowing particles form the stationary tissue. Fig. 5-3c shows the autofluorescence image of the skin tissue [135]. Fig. 5-3d shows a

projection of the 3D OCT data on the X-Y plane. Fig. 5-3e and f are the OCT and the OCTA B-scan images at the location marked in Fig.5-3d and Fig.5-3b revealing the tissue structures and the blood flow, respectively.

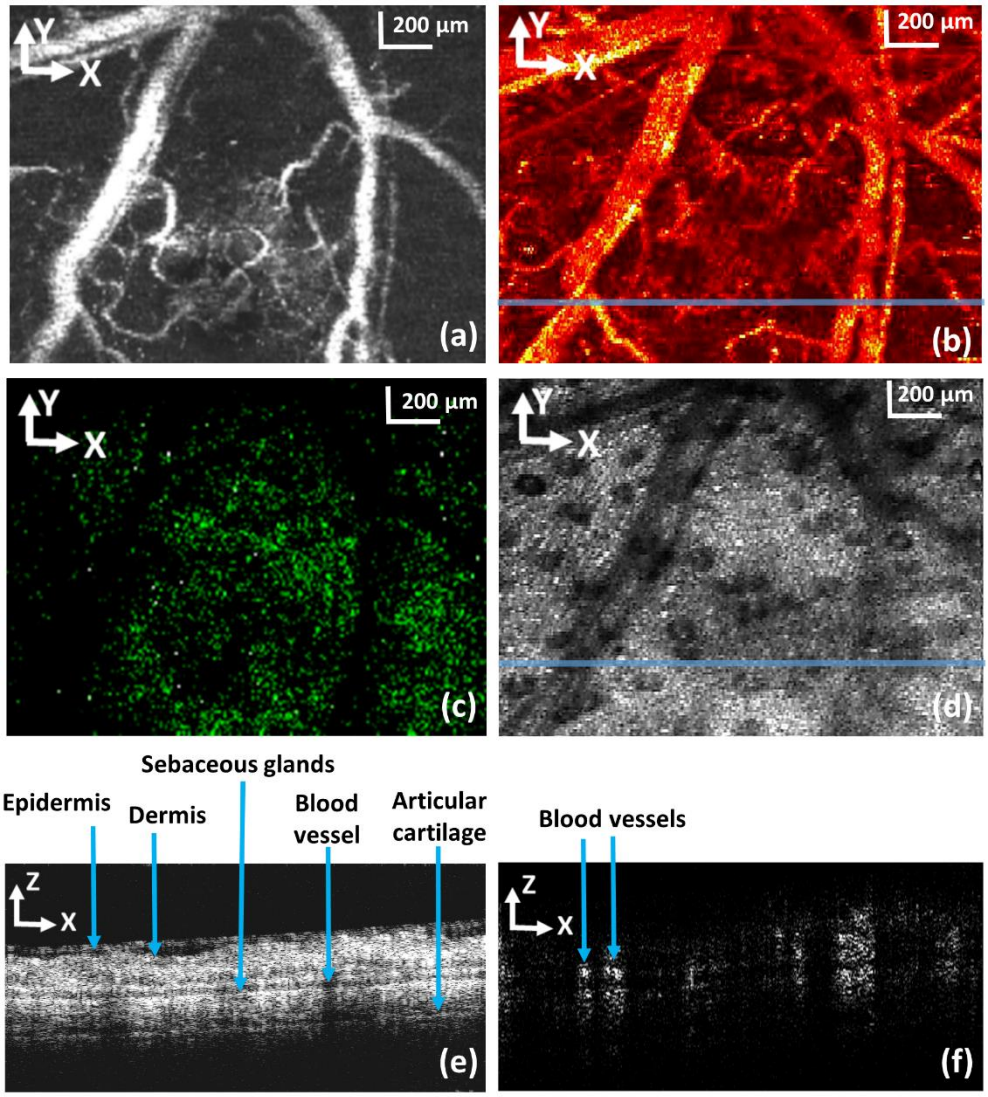

Figure 5-3 Simultaneously acquired PAM, CFM, and OCT images together with the OCTA image in the same ROI of a mouse ear. (a) Maximum amplitude projection of the PAM image; (b) *en face* view of the OCTA image; (c) CFM image; (d) OCT projection images generated from the acquired 3D OCT dataset; (e) OCT B-scan at the location marked in panel (d) by a solid line; (f) Cross-sectional OCT blood flow image at the location marked in panel (b) by a solid line; bar: 200 mm.

5.4 Discussion

We can see in the imaging results that the PAM and OCTA revealed similar features of the vasculature of the biological samples. Although both PAM and OCTA are developed to image the vasculature, the contrast mechanisms are different. PAM is based on the optical absorption of hemoglobin in the red blood cells and is able to image the oxygenation of the blood vessels by using multiple illuminating wavelengths. PAM is not sensitive to motion of the scattering blood cells, i.e., it is not sensitive to blood vessel non-perfusion. In contrast, OCTA is based on motion of the scatters in the blood vessels, not limited to the red blood cells. OCTA is sensitive to motion. It can thus reveal blood vessel non-perfusion, characteristics of the non-functioning microvasculature. The two optical imaging modalities can thus reveal complementary information of the microcirculation.

The lateral resolution of the different imaging modalities in the multimodal imaging system depends on the optical focus of the objective lens. Since the wavelength of the PAM illumination laser is in the visible spectrum much shorter than that used for OCTA we expect that the lateral resolution of the optical-resolution PAM is better than that of OCTA in the superficial region. However, the imaging depth of OCTA is expected to be better that that of optical-resolution PAM. Different from OCTA, a pure optical imaging modality, the sensitivity and the fast-scanning FOV of PAM depends on the detection sensitivity and FOV of the ultrasonic transducer. Thus, the PAM image quality highly depends on the ultrasonic transducer used.

We increased the FOV by combining optical scanning with mechanical scanning. To make the system suitable for practical applications we need to improve the FOV for the fast scan,

which is currently limited by the FOV of the ultrasonic transducer. To further improve the imaging speed, we need to use a laser with higher PRR. A state-of-the-art Q-switched laser can reach a PRR of higher than 100 kHz, which can increase our imaging speed of about 5 folds. In the current study we decoupled OCTA imaging from the simultaneous acquisition of PAM, OCT and CFM images. This is because the PRR of the pulsed laser is limited to 24 kHz, so it is not possible to simultaneously trigger the pulsed laser and the CCD camera for performing simultaneous imaging.

The imaging speed of the OCTA subsystem is limited by the line rate of the CCD camera and the achievable scanning speed of the galvanometer scanner. The allowable OCTA imaging speed of 70 kHz is similar to that used in most of the systems in ophthalmic applications. We used a speed of 40 kHz for the experiments due to the limitations of the galvanometer scanner. A faster galvanometer scanner will be needed to use the full speed of the spectrometer for OCTA.

The proposed imaging system will potentially be able to provide complementary information of either healthy or diseased tissues. For example, the proposed imaging system has the potential to be used in retinal imaging for the study and diagnosis of degenerative retinal diseases, where the contrasts of all the different imaging modalities are provided by endogenous agents such as, melanin (PAM), lipofuscin (CFM), retina tissue structure (OCT) and retinal capillary network (OCTA). Another example would be for brain imaging where blood vessel oxygen saturation can be measured with PAM for metabolism study; neural network imaging can be performed using multiphoton CFM (the current pulsed laser needs to be replaced with an ultrafast laser). In this application, OCTA

will be able to image the vasculature in the brain down to capillary level with higher imaging depth and faster imaging speed compared to optical-resolution PAM.

5.5 Conclusion

In summary, we have successfully added OCTA capability in our multimodal imaging platform. The system is able to provide OCTA together with PAM, OCT, and CFM imaging of biological tissues. We achieved large FOV and high imaging speed by combing optical scanning with mechanical scanning. The upgraded multimodal imaging system was tested by imaging animal models in vivo. We expect that further improvement on the proposed multimodal imaging system will make it more suitable for research and clinical studies.

CHAPTER 6 Comparative Study of Optical Coherence Tomography Angiography Algorithms for Rodent Retinal Imaging

6.1 Introduction

Optical coherence tomography angiography (OCTA) is a non-invasive imaging technology, which can reveal the three-dimensional (3D) microvasculature of biological tissues in vivo[33]. Based on the motion contrasts among the repetitively acquired OCT images, OCTA can differentiate moving particles (mainly red blood cells in blood flow) from the static background tissue generating a 3D map of the perfusing blood vessels. OCTA has been recognized as a powerful diagnostic and research tool in ophthalmology in evaluating retinal diseases such as diabetic retinopathy[37], glaucoma[38], age-related macular degeneration (AMD)[39], artery and vein occlusions[40], etc. In addition, OCTA has also been used in the research and clinical investigations in dermatology[41], gastroenterology[42], and neurology[136].

Several OCTA algorithms have been developed to extract the motion contrast buried in the measured OCT signals, the interference signal of the light reflected from the reference and sample arms of the interferometer. Depending on whether phase, intensity, or the complex interference signal is used for the calculation, the algorithms can be categorized into phase based, intensity based, and complex signal based OCTA. The widely used algorithms include split-spectrum amplitude-decorrelation angiography (SSADA)[131], speckle variance (SV)[128], phase variance (PV)[129], improved speckle contrast (ISC)[133], and optical microangiography (OMAG)[132].

Imaging the retinal vasculature of animals, especially rodent models, is one critical application of OCTA, since animal models play a key role in basic research and treatment development for all kinds of eye diseases. However, a large majority of the OCTA ophthalmic applications are on humans including comparative studies of the different algorithms[127,137-145]. Since the anatomy, size, and metabolic rate of rodent eyes are different from human, the performance of the different OCTA algorithms may differ from that in human applications. In this study, we compared the angiographic images calculated from the same datasets by using the three different OCTA algorithms in the three different categories qualitatively and quantitatively. A statistical analysis is performed among the quantitative results (a paired t-test) to provide more information about the performance of each of the OCTA algorithms.

6.2 Methods

6.2.1 OCTA Algorithms

For OCTA imaging, at each spatial location of the sample (either rat retina or mouse ear in our studies) 4 cross-sectional images (B-scans) were acquired consecutively. The coordinate system was selected in which X represents the coordinate of the fast scan (B scan, the horizontal direction for retinal imaging), Y represents the coordinate of the slow scan (vertical direction in retinal imaging), and Z represents the coordinate in the depth. We use *j* to represent the number of the repetitive B-scan and N to represent the total number of the repetitive B-scan at each sample location. The depth resolved OCT signal at each spatial location can then be described as:

$$I_{OCTj}(x,y,z) = A_j(x,y,z)\exp\left[\phi_j(x,y,z)\right] \quad (1)$$

where $A_j(x,y,z)$ and $\phi_j(x,y,z)$ are the spatially resolved amplitude and phase of the OCT signal of the *j*-th B-scan.

6.2.1.1 PV Algorithm

The PV algorithm calculates the phase difference among the repeated consecutive cross-sectional OCT B-scans. Unlike the method for Doppler OCT, in which the phase difference is calculated between the adjacent A-lines in a B-scan, calculations are done among the B-scans meaning with much longer time interval. Consequently, the images contain no flow velocity information. This method minimizes the dependency of flow detection on vessel orientation. Typically, PV requires bulk motion correction and phase unwrapping prior to the final phase variance calculation. This algorithm has been successfully implemented in retinal imaging [146,147]. The PV algorithm can be expressed in the following formula [148]:

$$I_{PV}(\mathrm{x},\mathrm{y},\mathrm{z}) = \frac{1}{1-N} * \sum_j^{N-1}[\Delta\phi_j(x,y,z) - \frac{1}{1-N}\sum_{j=0}^{N-1}\Delta\phi_j(x,y,z)]^2 \quad (2)$$

where I_{PV} is the OCTA flow signal and $\Delta\phi_j$ is the phase difference between the consecutive B-scans.

6.2.1.2 ISC Algorithm

In the ISC algorithm, the changes in the OCT signal intensity between subsequent B-scans caused by the moving particles are calculated [133,149]. To calculate the OCTA signal, the amplitude of the OCT signals from each of the 4 B-scans was used to calculate the speckle contrast image k_s [133]:

$$k_s(x,\mathrm{y},z) = \frac{1}{1-N} * \sum_j^{N-1} \frac{\left|A_{j+1}^2(x,y,z) - A_j^2(x,y,z)\right|}{A_{j+1}^2(x,y,z) + A_j^2(x,y,z)} \quad (3)$$

The final blood flow image was generated as following:

$$I_{ISC} = A_s^2(x,y,z) * k_s(x,y,z) \quad (4)$$

where I_{ISC} is the OCTA flow signal used for the final blood flow image; A_s^2 is the mean of intensity value of the 4 consecutive B-scans.

6.2.1.3 OMAG Algorithm

OMAG calculates the flow signal by performing a direct subtraction of the complex OCT signal between the consecutively repeated B-scans. [150,151]. The flow signal can be calculated with the following equation [152]:

$$I_{OMAG} = \frac{1}{1-N} * \sum_{j=0}^{N-1} (\left|I_{OCTj+1}(x,y,z) - I_{OCTj}(x,y,z)\right|). \quad (5)$$

6.3 System and In Vivo Animal Imaging

We used the near infrared OCT (NIR-OCT) in our previously developed dual-modal VIS-OCT-FAF retinal imaging system[153] for rodent retinal imaging. In brief, the NIR-OCT used a broadband superluminescent diode (SLD) with a center wavelength of 840 nm and bandwidth of 50 nm as the light source. The interference light was detected by a home-built spectrometer with a line scan CMOS camera (Sprint, Basler) with an A-line rate of up to 140 kHz. For in vivo mouse ear imaging, we used the OCTA function of our proposed Penta-modal imaging system, in which a SLD-based NIR light source with a center wavelength of 840 nm and bandwidth of 100 nm (Broadlighter, Superlume Diodes) was

used. In the Penta-modal imaging system, the OCT signal was detected by a home-built spectrometer with a fast CCD camera (Aviva EM4, e2V, maximum A-line rate: 70 kHz). In both retina and mouse ear imaging we used A-scan speed of 40 kHz, considering the limitation of the X-Y galvanometer scanner. The imaging conditions, including the position of the reference arm, light power, and focus, have been kept constant in each experiment. For OCTA imaging, each of the 128 B-scans was repeated four times at each spatial location, i.e., each y location, of the sample. Each B-scan consisted of 512 A-lines. Thus, in each imaging area a total of 512×4×128 A-lines were acquired, covering an area of 1.5 mm × 0.75 mm of the rat retina (2 mm× 2 mm of the mouse ear). The NIR light power was 800 μW and 600 μW for in vivo rat retina and a mouse ear imaging, respectively.

6.4 Study Design

To make a more general comparison among the different OCTA algorithms for ophthalmology and microscopic imaging applications, we imaged both rat retina and mouse ear. Four eyes of albino Spraque Dawley rats were imaged, and a mouse ear (Swiss Webster) was also imaged in vivo. Each acquired dataset were processed with the ISC, PV, and OMAG algorithms. The retinal images were segmented manually at the inner limiting membrane (ILM), the inner nuclear layer (INL), the external limiting membrane (ELM), and the retinal pigment epithelium (RPE). The superficial, deep, and RPE layers were defined as the retinal layers from ILM to INL, INL to ELM, and ELM to RPE. For each layer the OCTA data were projected onto the X-Y plane by using axial summation amplitude projection (SAP). The quality of the projected OCTA images was compared first visually by looking at how much detail of the capillary network can be resolved. To make

quantitative comparisons, we calculated the blood vessel density (BVD), vessel diameter index (VDI), vessel perimeter index (VPI), and vessel complexity index (VCI) for the segmented superficial retinal layers [154,155]. All the linear-scale images were denoised, binarized, and skeletonized prior to the quantitative analysis [156].

BVD is defined as the ratio of the total image area occupied by the vasculature to the total area in an OCTA image:

$$BVD = \frac{\sum_{x=1,y=1}^{n} A^2(x,y)}{\sum_{x=1,y=1}^{n} I(x,y)} \quad (6)$$

where $A^2(x,y)$ represents the intensity value of the pixels in linear scale registered as vessel area (white pixels on the binarized map), $I(x,y)$ represents all the n pixels occupied by the OCTA image.

VDI is calculated as the ratio of the vessel area to the vessel length, as shown in the following formula:

$$VDI = \frac{\sum_{x=1,y=1}^{n} A^2(x,y)}{\sum_{x=1,y=1}^{n} S(x,y)} \quad (7)$$

where $A^2(x,y)$ denotes all the pixels occupied by vessel area, and $S(x,y)$ represents all the pixels occupied by vessel length (white pixels on skeletonized map).

VPI is defined as the ratio of overall contour length of blood vessel boundaries to the total area in the OCTA image:

$$VPI = \frac{\sum_{x=1,y=1}^{n} P(x,y)}{\sum_{x=1,y=1}^{n} I(x,y)} \quad (8)$$

where *P(x,y)* represents the pixels within the vessel perimeter (white pixels on perimeter map), and *I(x,y)* donates all the pixels in the OCTA image.

VCI is quantified using both the vessel perimeter and the vessel area map, calculated as:

$$VCI = \frac{[\sum_{x=1,y=1}^{n} P(x,y)]^2}{4\pi \sum_{x=1,y=1}^{n} A^2(x,y)} \quad (9)$$

where *P(x,y)* represents the pixels within the vessel perimeter (white pixels on perimeter map), and $A^2(x,y)$ represents the pixels registered as vessel area (white pixels on binarized map).

All experimental animal procedures were conducted in compliance with the guidelines of the Florida International University's Institutional Animal Care and Use Committee.

6.5 Results

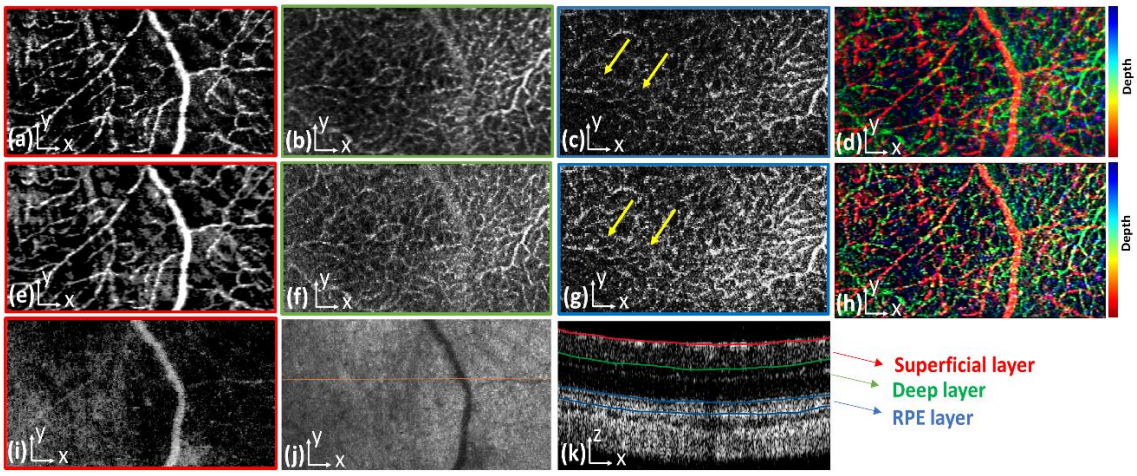

Figure 6-1 The OCTA retinal image of an albino rat processed with ISC, OMAG, and PV. (a), (b), and (c): SAP of the OCTA data in the superficial, deep, and RPE layers processed with ISC; (d): the ISC composite image of all the retinal layers coded with color; (e), (f), and (g): SAP of the OCTA data in the superficial, , deep, and RPE layers processed with OMAG; (h): the OMAG composite image of all the retinal layers coded with color; (i) SAP of the OCTA data in the superficial retinal layer processed with PV; (j) OCT fundus image; (k) OCT cross-sectional image illustrating the segmented retinal layers in the retina at the location marked in panel (j) by the solid line. Colormap: red=superficial retinal layer, green= deep retinal, blue= RPE layer.

Figure 6-1 shows the retinal images processed with the ISC (Fig. 6-1a, b, and c), OMAG (Fig. 6-1e, f, g), and PV (Fig. 6-1i) algorithms. Fig. 6-1a, e, and i are the SAP of the OCTA data in the superficial retinal layer processed with ISC, OMAG, and PV, respectively. Fig. 6-1b and f are the SAP of the OCTA data in the deep retinal layer processed with ISC and OMAG, respectively. Fig. 6-1c and g are the SAP of the OCTA data in the RPE layer processed with ISC and OMAG, respectively. Fig. 6-1d and h are the composite images of ISC and OMAG of all the retinal layers coded with color (red: superficial retinal layer; green: deep retinal layer; blue: RPE layer). Fig. 6-1j is the OCT fundus image[107] (*en face* view of the 3D OCT data). Fig. 6-1k is the OCT cross-sectional image showing the segmentation.

As can be observed, both the ISC and OMG algorithms are successful in constructing the images of the vascular networks in different retinal layers. However, there are some differences in revealing the details of the microcapillaries. As pointed by the arrows, the OMAG algorithm can resolve more capillaries and the signal strength in the deeper layer in the OMAG images is higher. In contrast, the PV algorithm was able to visualize only the large blood vessels in the superficial layer of the retina. We do not include the images of the deeper layers processed with the PV algorithm in Fig. 6-1 due to the poor quality.

Figure 6-2 shows the in vivo imaging results of the mouse ear. Fig. 6-2a is the *en face* view of the 3D OCT data, in which no blood vessels can be clearly visualized. Fig. 6-2b, c, and d are the SAP of the OCTA images constructed with the ISC, OMAG, and PV algorithms, respectively. We can see that all the three OCTA algorithms can comparatively visualize

the major blood vessels in the mouse ear while ISC and OMAG are more successful in resolving the capillaries, a result consistent with that of rodent retinal imaging.

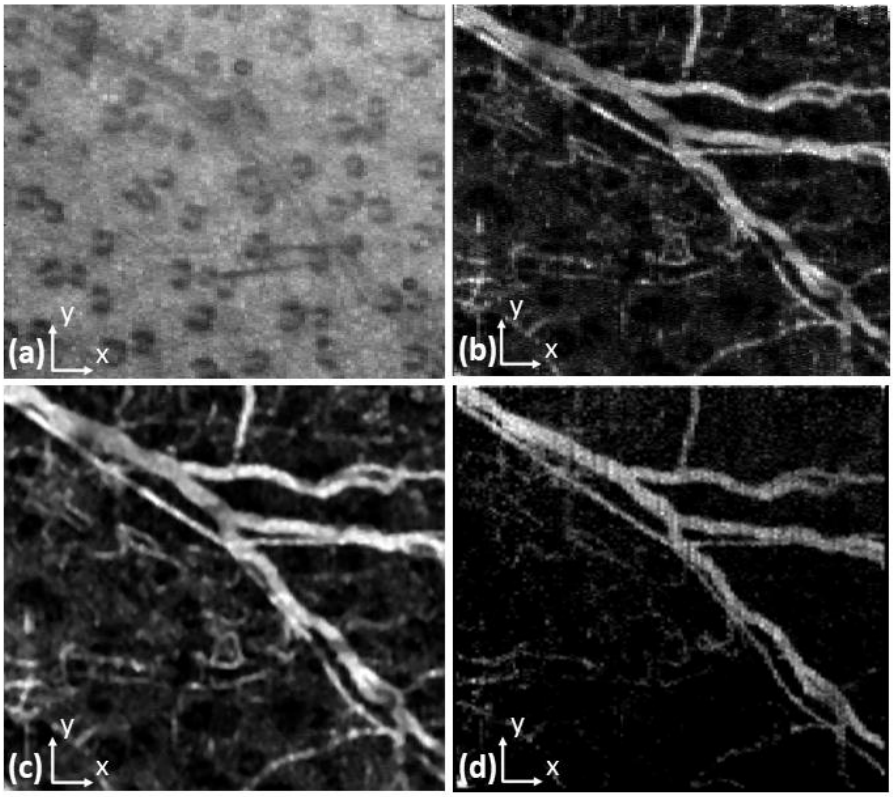

Figure 6-2 OCTA image of a mouse ear processed with ISC, OMAG, and PV. (a): OCT *en face* view; (b): SAP of the OCTA data processed with ISC; (c) SAP of the OCTA data processed with OMAG; (d) SAP of the OCTA data processed with PV.

6.6 OCTA Algorithm Quantitative Comparisons

We quantitatively compared the performance of ISC and OMGA in rodent retina and mouse ear imaging. Due to the relatively poor performance of the PV methods in visualizing the small blood vessels and capillaries compared to ISC and OMAG, we excluded this technique in our quantitative comparison study. Table 6-1 shows the calculated BVD, VDI, VPI, and VCI, from the acquired images (n = 4 for rat retina and n = 1 for the mouse ear).

Table 6-1 Summary of the calculated OCTA quantitative parameters

Datasets	1		2		3		4		5	
Parameters	ISC	OMAG	ISC	OMAG	ISC	OMAG	ISC	OMAG	ISC	OMAG
BVD	0.24	0.28	0.22	0.26	0.27	0.32	0.32	0.35	0.16	0.15
VDI (μm)	17	18	29	30	42	41	29	32	48	44
VPI	0.14	0.16	0.08	0.09	0.07	0.08	0.11	0.11	0.03	0.04
VCI	1024	1018	420	430	340	370	190	180	110	67

BVD: blood vessel density, VDI: vessel diameter index, VPI: vessel perimeter index, VCI: vessel complexity index

A paired t-test analysis was performed for the data between the two algorithms (P-value $\leq$ 0.05 was assumed for statistical significance). The OMAG algorithm provided statistically significant higher mean values of BVD and VPI compared to the ISC algorithm (0.27±0.07 vs. 0.24±0.05 for BVD; 0.09±0.04 and 0.08±0.04 for VPI), while no statistically significant difference was observed for VDI and VCI among the algorithms (Table 6-2).

Table 6-2 Statistical analysis results between ISC and OMAG

Parameter	**OMAG**	**ISC**	***P-value***
BVD	0.27±0.07	0.24±0.05	0.04*
VDI	33±10	33±12	0.91
VPI	0.09±0.04	0.08±0.04	0.01*
VCI	410±370	420±360	0.64

* Significant difference

6.7 Discussion

From the imaging results on rat retina and mouse ear we can see that both ISC and OMAG images are similar in visualizing the microvasculature, suggesting that both algorithms are suitable for OCTA applications in rodent models. The PV algorithm performed poorly, especially in retinal imaging. This might be caused by several factors including phase instability of the imaging system and uncontrolled sample motion. Previous experimental studies [157] concluded that the sole phase information may not be ideal for obtaining high quality images of the vascular structures. For visualizing capillaries in deeper layers such as the RPE (See Fig 1c, and g), consistent with previously reported in the literature [127,157], OMAG provided slightly better results for the vascular network compared to ISC, possibly due to the utilization of the full OCT signal for flow signal calculation. However, since the ISC algorithm only takes the amplitude of the OCT signal into account for motion-contrast calculations, this algorithm is less computationally intensive compared to OMAG. Additionally, OMAG and PV are all sensitive to bulk motion artifacts, which requires a relatively time-consuming bulk motion effect removal before the final OCTA image reconstruction. It should be noted, however, that none of the above techniques were successful in visualizing the choriocapillaris in rodent retina, which needs to be investigated further. One probable reason is the anatomy of the rodent eye, such as the structure of the anterior segments and the small pupil size of the rat eye compared to humans, which may negatively affect the capability in resolving the deep choriocapillaris. We observed that some of the small vessels appeared in the OCTA images were not fully

connected. We hypothesize that this discontinuity was due to either the limited sampling density or slower blood flow in the rodent's eye compared to humans.

In the quantitative evaluations we can see that OMAG provided statistically significant higher mean values of BVD and VPI compared to the ISC, which may mean that OMAG can reveal more blood vessels as evidenced in the OCTA images. However, whether this mean that OMAG is superior in revealing the true values still need studies to compare with histology. The importance of the current findings is that when using OCTA as a tool in research or diagnostic applications it is necessary to use the same algorithm throughout the whole process. In the calculations of BVD, VDI, VPI, and VCI we only evaluated the superficial retinal layers for quantitative comparison, since imaging the vasculature of the deep retinal layers in the rodent retinas were not always successful.

In this study, to cover different applications we imaged rat retina and mouse ear, which covers ophthalmoscopy and microscopy, two major different optical configurations: retinal imaging requires an ocular lens while microscopy requires only an objective lens. In ophthalmoscopy the lateral resolution is mainly limited by the optics of the eye while in microscopy the lateral resolution is mainly limited by the NA of the objective lens. Thus, this study may represent general imaging conditions although more data are needed to make the observations more conclusive. The poor performance of PV in our study may related to the specific imaging system we used. Further test will be needed to include not only larger sample size but also different imaging systems preferably commercial OCT systems with and without eye tracking.

6.8 Conclusion

In summary, we compared three representative OCTA algorithms, ISC, PV, and OMAG for imaging animal models visually and quantitatively. It was shown that ISC and OMAG algorithms are more robust to provide high quality OCTA images in rodent imaging in vivo. Results also demonstrated that OMAG may provide slightly better visual results for the vascular network in deeper layers compared to the ISC method. Statistically significant higher BVD and VDI values calculated from OMAG than ISC suggests that it is necessary to use the same OCTA algorithm in research and diagnosis when these values are used as a marker of disease status, progression, or treatment outcomes.

CHAPTER 7 Multimodal Imaging of Plasmodium Parasites in Mosquito Midguts

7.1 Introduction

Malaria parasites in mosquito midguts undergoes several stages for infecting the insect vector and ultimately causing the spread of pathogen and disease. The malaria parasite transmission cycle involves a rapid production of gametes, fertilization, and conversion of zygotes into motile ookinetes immediately after blood feeding. After 19 to 36 hours, the invasion process begins with crossing the midgut wall by ookinetes and eventually transforming into oocysts in the basal subepithelial space. The invasion process is found to be very slow, and the parasites go through different modes of motility while crossing the midgut wall. These include stationary rotation, translocational straight segment motility, and translocational spiralling motility. The malaria parasites development involves morphological and cellular changes in plasmodia as well as the midgut epithelia membrane[158,159].

The development of malaria parasites in mosquito midguts is a crucial link between insect vector and human host. An in-depth understanding of this process can help the development of new strategies aiming at transmission-blocking and ultimately inhibiting the spread of the disease by the mosquito. The in vivo imaging of midgut has been previously reported by Dina Vlachou et al. [160]. Utilizing a high-resolution 4 dimensional (4D) and 3D confocal microscopy, the authors imaged the parasite in the explanted or intact midgut of living mosquitos.

Here, we report the preliminary results of our investigation on feasibility of the proposed multimodal imaging system for in vivo study of malaria parasite invasion within mosquito midgut. We hypothesize that OCT, CFM and PAM can be used to image different optical contrasts inside the mosquito midgut. In addition, the OCT motion contrast imaging can be utilized to test the feasibility of this imaging technology for slow motion detection of the parasites within the midgut, as well as tracking the movement of the parasites at different modes of motility. The OCT motion contrast imaging has been shown to be sensitive to slow movements (e.g., the Brownian motion can be detected by the OCT motion-contrast imaging technology[161]). Thus, we hypothesize that this technology can help detect the parasite movement inside the midgut with high sensitivity. The depth-resolving capability of OCT can also aid the detection and visualize structural changes in the midgut caused by the motion of parasites.

We tested our hypothesis by imaging phantom, ex vivo midgut, and in vivo mosquito infected with malaria parasite.

7.2 Methods

7.2.1 Imaging System

The imaging system configuration used for conducting this experimental imaging study was similar to our previously described system shown in Fig.1-1 in Chapter 5. We used the fast-optical scanner to image the small FOV of 2 mm and 2 mm for ex vivo midgut, and the living mosquito imaging studies. All OCT, OCTA, PAM and CFM images consisted of 512 × 128 pixels. For PAM/CFM/OCT ex vivo midgut imaging, the scanning rate of 20 kHz was used. To ensure the OCT motion-contrast imaging is sensitive for slow motion

detection, the OCT motion-contrast phantom imaging was performed with an interscan time of 1 minute to increase the time interval between the signal measurements. The flow signal was calculated between four repeated B-scans, extracted from each OCT dataset with 1-minute time interval at scanning rate of 10 kHz. For in vivo mosquito imaging, the OCT motion-contrast imaging was performed with four repetitions for each B-scans at the scanning rate of 10 kHz. The same ISV-OCTA method was adopted for generating the motion-contrast OCT images, for both phantom and in vivo experiments.

7.2.2 Sample Preparation in Phantom, Ex Vivo, And In Vivo Experiments

The proposed multimodal imaging platform was used to image different samples including phantom, ex vivo midgut, and in vivo mosquito. All ex vivo, and in vivo malaria parasite samples were collected from the Biology department at Florida International University. All procedures were in accordance with the guidelines of the Florida International University's Institutional Animal Care and Use Committee.

We first performed PAM, OCT, and CFM multimodal imaging by imaging the ex vivo midgut samples. The samples were collected and imaged immediately after extraction from the infected mosquitos. The sample was gently placed on the imaging plate and was immersed in water for acoustic coupling and to ensure that the samples stay hydrated during the scanning.

Further, we tested the potential capability of the OCT motion-contrast function for detecting the slow motion of ookinete malaria parasite in the midgut. The phantom solution (Intralipid 20%) was diluted, and a programmable syringe pump was used to inject the

solution into a plastic tube (inner diameter of 1.5 mm). A constant slow velocity of 5 μm/min was set to mimic the slow parasite motion during the midgut invasion process.

The in vivo mosquito imaging was subsequently performed by the OCT motion contrast technique along with the conventional OCT imaging to monitor the structural changes and the parasite invasion process inside the midgut within the living mosquito sample. All in vivo samples were infected with the malaria parasite and were prepared by an expert in the Biology laboratory. The samples were then transferred to the optical imaging laboratory. After securing each sample on a holder plate, we imaged infected living mosquito samples over a time course of 45 minutes.

7.3 Results

7.3.1 Ex Vivo PAM, OCT, and CFM Imaging of Midgut

We first performed PAM, OCT, and CFM multimodal imaging of an ex vivo midgut samples. The samples were collected from the Biology department and then imaged immediately after extraction from the infected mosquitos. We present our preliminary results on mosquito malaria parasite midgut multimodal imaging, as shown in Fig.7-1.

Fig. 7-1 (a) shows the autofluorescence image, potentially originating from the cluster of parasites invading the midgut wall. Fig. 7-1 (b) demonstrates 2D OCT projection images generated from the acquired 3D OCT dataset. The tissue structure of the midgut is also visualized in the OCT B-scan shown in Fig. 7-1 (d). The dark shadows appeared in the OCT B-scan is possibly due to the invasion of parasites through the midgut wall. To test the capability of the PAM imaging subsystem, we also imaged one midgut sample

separately. We hypothesize that the PAM signals are generated by blood in the midgut. Our preliminary results indicate that the multimodal imaging system was able to acquire CFM, OCT and PAM images from mosquito midgut specimens based on different optical contrasts.

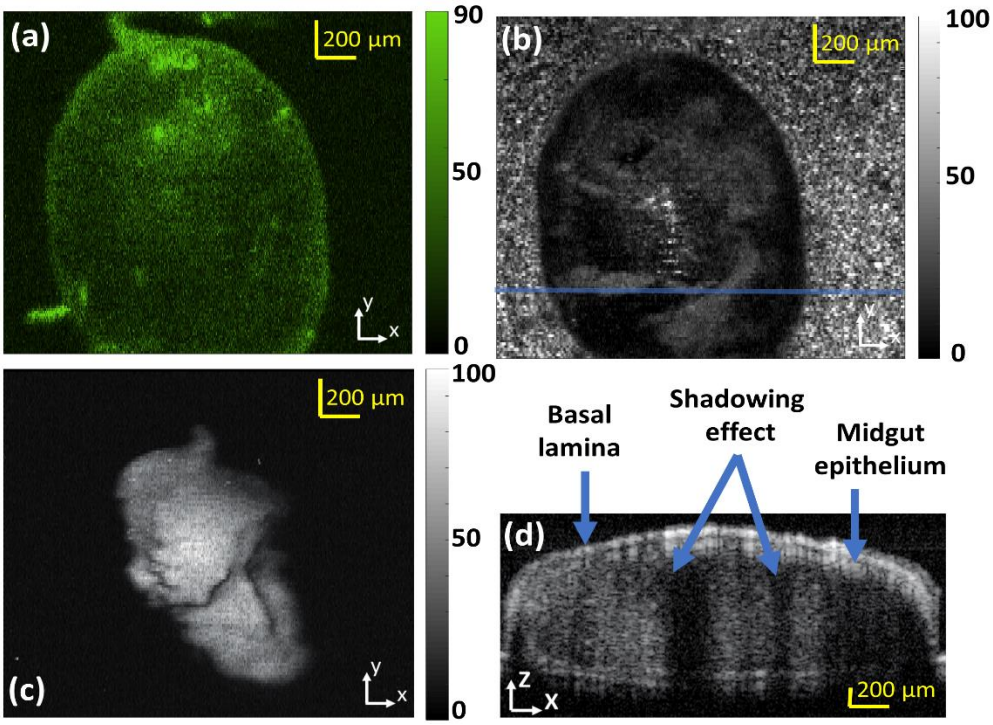

Figure 7-1 Simultaneously acquired CFM, and OCT images together with the PAM image of two different mosquito midguts infected samples. (a) CFM image; (b) OCT projection images generated from the acquired 3D OCT dataset; (c) Maximum amplitude projection of the PAM image; (d) OCT B-scan at the location marked in panel (b) by a solid line; bar: 200 µm.

7.3.2 OCT Motion-Contrast Imaging: Phantom Study

A plastic tube with inner diameter of 1.5 mm was attached to the tip of a 10 mL syringe mounting on a programmable pumping syringe (WPI AL-1000). The flow velocity of 5 µm/min was set, mimicking the slow speed of the malaria parasite inside the midgut of a living mosquito. The phantom study was designed to ensure that the OCT motion-contrast imaging subsystem would be able to detect the slow motion. The tube was then secured on a holder plate under the objective lens for imaging. The Intralipid 20% was injected through

the tube with a flow speed of ~5 μm/min. The Intralipid was used for the phantom experiment due to its high scattering optical property, which was desired for the OCT signal detection.

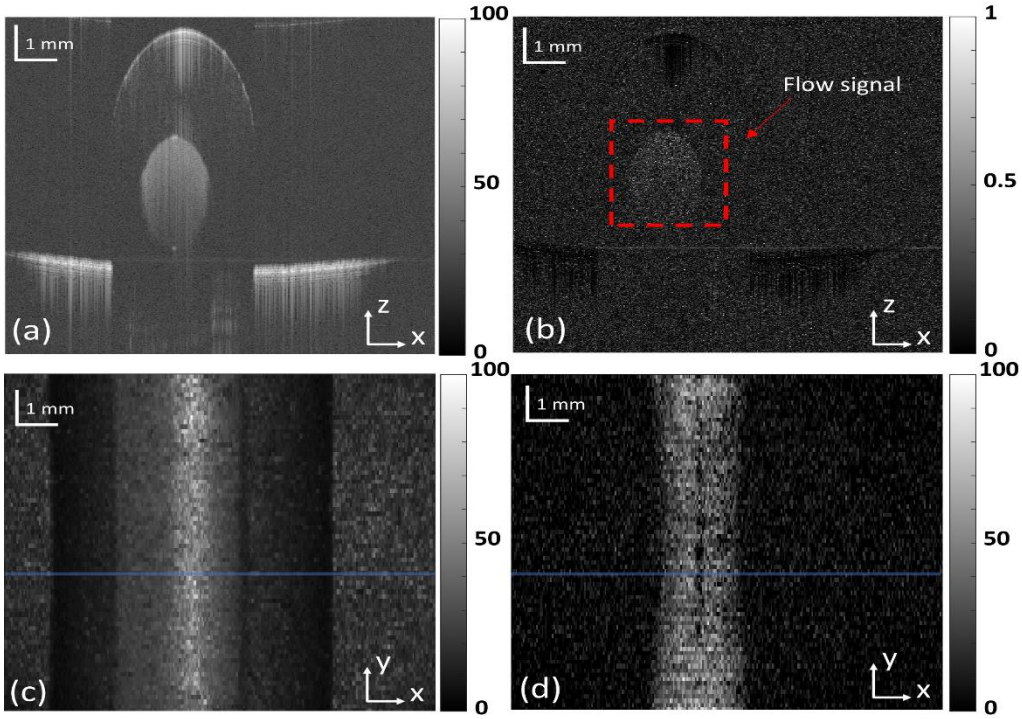

Figure 7-2 OCT motion-contrast image of a capillary tube. (a) OCT B-scan image at the location marked in the panel (c) by a solid line; (b) cross-sectional OCT flow image at the location marked in the panel (d) by a solid line; (c) En face OCT image; (d) En face OCT flow image; bar:1 mm.

Figure 7-2 demonstrates the OCT motion-contrast image of the tube consisting of 512×128 pixels. The OCT motion-contrast imaging was performed at a scanning rate of 10 kHz and each B-scan was repeated 4 times at each location. The ISC-OCTA technique, as detailed in Chapter 5, was applied to calculate the flow signal and generate OCT motion-contrast image. Fig. 7-2 (a) demonstrate the cross-sectional OCT B-scan, revealing the outer and inner surface of the tube as well as the Intralipid flow inside the tube. Fig. 7-2 (b) shows the OCT motion-contrast cross-sectional B-scan. It can be observed that only the flow signal is revealed at the center of the image, while the stationary background signal,

including outer and inner surfaces of the tube, appear to be black. Fig. 7-2 (c) displays the *en face* view of the conventional OCT image of the capillary tube, while Fig. 7-2 (d) illustrates the *en face* view of the OCT motion-contrast image of the tube. The relatively low SNR of the OCT motion-contrast image was due to the slow flow rate, making the flow signal detection challenging.

7.3.3 OCT Motion-Contrast Imaging: In Vivo Infected Mosquito Imaging Study

Following the phantom imaging study, we imaged a living infected mosquito with OCT motion-contrast together with the conventional OCT. Wings were cut for immobilization of the sample. The sample was gently secured on an imaging plate for imaging.

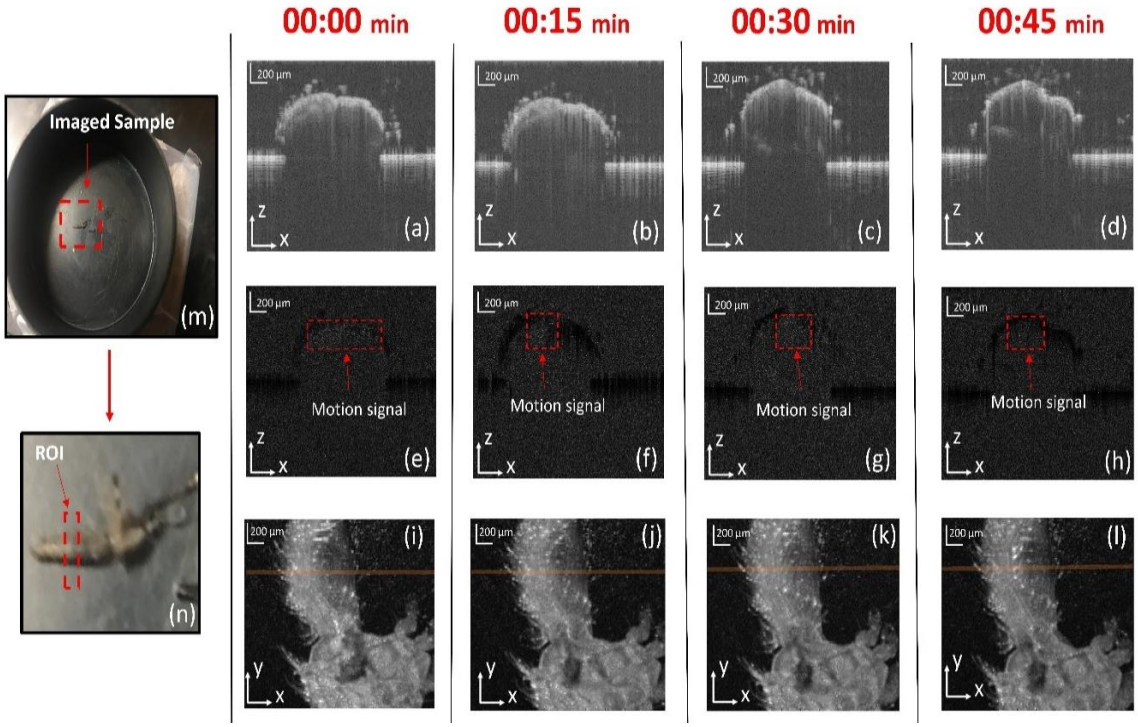

Figure 7-3 Simultaneously acquired OCT motion-contrast images together with the OCT image of a living mosquito; (a, b, c, d) OCT B-scans acquired every 15 minutes, at the location marked in panel (i, j , k, l) by a solid line; (e, f, g, h) Cross-sectional OCT motion contrast images of the corresponding B-scans; (i, j, k, l) OCT projection images generated from the acquired 3D OCT dataset; (m) Colored image of the imaged sample; (n) The imaged ROI; bar: 200 µm

The scanning range was set to 2 mm by 2 mm. The living mosquito was monitored over a course of 45 minutes by performing OCT motion-contrast imaging as well as the conventional OCT every 15 minute at scanning rate of 10 kHz. The structural OCT and OCT motion-contrast images were processed to monitor any structural changes or detect any motion inside the midgut caused by the parasite membrane invasion. Figure 7-3 demonstrates our preliminary results on the OCT and OCT motion-contrast images of the in vivo sample. Fig. 7-3 (a, b, c, d) are the B-scan OCT images of the midgut revealing the tissue structure. It can be observed that the midgut structure close to the surface has been changed over time, which may be the result of parasite motion inside the midgut. Fig. 7-3 (e, f, g, h) shows the cross-sectional OCT motion-contrast images of the corresponding structural CT B-scans, detecting the motion inside the midgut, which was possibly generated by the parasite movement. Fig. 7-6 (m) and Fig. 7-3 (n) depict the colored image of the sample and the ROI, respectively. The OCT 2D projection of the samples for every dataset are shown in Fig. 7-3 (i, j, k, and l).

7.4 Discussion

We examined the capability of the proposed multimodal imaging system for the study the mosquito malaria parasite invasion process in the midgut. The imaging system was tested on ex vivo, and in vivo samples. It was shown that the imaging platform can target different molecules in the ex vivo midgut specimen using PAM, OCT, and CFM imaging. However, we could not clearly identify the source of each optical contrast. In addition, the OCT motion contrast together with the conventional OCT was found to be promising for the detection of parasite motion as well as structural changes inside the mosquito midgut.

The structural changes and the detected motion within the midgut of the living mosquito samples, appeared in the conventional OCT images as well as the OCT motion-contrast images, supporting the potential application of the proposed multimodal imaging for imaging the malaria parasites and it holds a great potential for monitoring the invasion process in the midgut.

This study is still in its early stages and further improvements in the imaging system is required for malaria parasite imaging with high precision and accuracy. For example, the resolution of the OCT motion contrast imaging system in this study was not high enough to resolve the individual parasites. The higher spatial resolution of the imaging system will also be required to improve monitoring the morphological changes in the ookinete parasites. Furthermore, since motion detection sensitivity using the OCT motion contrast heavily relies on the A-line scanning rate, and that the parasite movement velocity varies with the motility stage, additional experimentation and observations are needed to obtain an optimal scanning rate of the system to monitor different stages of the invasion process. In this study, we primarily focused on structural changes and motion detection close to the outer surface of midgut. Follow up studies can also monitor the invasion process in deeper layers within the midgut owing to high imaging depth of the OCT technology. In future imaging studies, transgenic parasites expressed with GFP [160] can also be utilized to facilitate visualization of the Plasmodium ookinetes in the mosquito midgut.

7.5 Conclusion

The proposed multimodal imaging system was utilized to image the malaria parasite in the mosquito's midgut for the first time. The preliminary results were shown to be promising,

indicating the potential of the imaging system for use in studying the movement of malaria parasites and the invasion process. The presented multimodal imaging system may provide valuable insight into better understanding of the infection and transmission process of malaria parasites in the mosquito midgut.

CHAPTER 8 Concluding Remarks

8.1 Summary

Although different optical imaging technologies have a key role in various areas of biomedical research, the limitations associated with each contrast mechanism limits the information they can provide for disease diagnosis. To address this issue, we developed a Penta-modal microscopic optical imaging system featuring a novel OCT-guided contour scanning technique, which can image complementary contrasts of a sample either ex vivo or in vivo. The imaging system images the contrasts that are based on optical absorption (PAM), optical scattering (OCT), blood flow velocity (ODT), motion of the scatters (OCTA), and fluorescence (CFM).

We first developed a quadruple-modal imaging system by integrating PAM with OCT, ODT, and CFM (chapter 3). The images are acquired by using the mechanical scanning, which scans the sample. A single Q-switched 532 nm laser was shared for PAM and CFM, while a NIR light source was used for OCT, ODT. The imaging system also features OCT-guided dynamic focusing, a technique for adjusting objective lens focus to follow the contour of the sample surface. It is necessary to apply dynamic focusing for a sample having uneven surface to help achieve uniform spatial resolution and SNR across the ROI. Dynamic focusing was enabled by the OCT depth information of the sample surface. Since mechanical scanning was employed for multimodal imaging, point by point dynamic focusing was applied. The focus of the objective lens can be adjusted for each A-line of PAM. Dynamic focusing using PAM or US for contour scanning was previously reported

by other groups[99,162]. Yeh et al.[99] developed a purely OR-PAM contour scanning method, which continuously adjusted the focus by tracking blood vessels' profile. This method was used to study tumors with uneven surfaces in mouse brain in vivo. In another research study, Ning et al.[162] developed an ultrasound-aided PAM dynamic focusing approach. This method directly detects the skull cortex surface relying on US pulse-echo signals rather than inaccurate PAM based method, which depends on brain vessels. In comparison, our OCT-guided dynamic focusing approach may provide a better guiding accuracy due to higher axial resolution and faster guiding speed thanks to the better performance of OCT.

Further, we combined the mechanical scanning with the optical scanning to achieve large FOV and high imaging speed (chapter 4). Upon the upgrading the imaging system, we achieved a uniform resolution in an FOV of 10 mm×10 mm with an imaging time of ~5 min. Since fast imaging speed was desired, the point-by-point dynamic focusing method was replaced by an aerial dynamic focusing strategy for multimodal imaging system using the combination of optical and mechanical scanning. This approach adjusts the objective-lens focus according to the depth of surface at the center of each fast-optical scan area. This strategy is suitable for achieving dynamic focusing in large FOV with fast-speed imaging.

We later added OCTA function to the proposed multimodal imaging system and its performance was tested by imaging mouse ear in vivo (chapter 5). The upgraded multimodal imaging system integrated five imaging modalities, including, PAM, CFM, OCT, ODT, and OCTA. Generated by the same photons, the images of PAM and CFM are precisely registered in the lateral directions, while the OCT, ODT, and OCTA images are

also registered. Registration among the PAM/CFM and OCT-based images was achieved by light alignment and synchronization control.

Next, we conducted a comparative study to evaluate the performance of different OCTA algorithms for ophthalmology and microscopic imaging applications (chapter 6). Both rat retina and mouse ear were imaged for more general comparison. We compared the performance of three OCTA algorithms that are based on the variance of phase, amplitude, and the complex representations of the OCT signals for rodent retinal imaging, namely the PV, ISC, and OMAG. The performance of the different algorithms was evaluated by comparing the quality of the OCTA images regarding how well the vasculature network can be resolved. Quantities that are widely used in ophthalmic studies including BVD, VDI, VPI, VCI were also compared. Our results demonstrated that both the ISC and OMAG algorithms are more robust than PV, and they can reveal similar vasculature features while there are statistically differences in the calculated quantities.

Following the promising results from in vivo animal studies, the potential application of the proposed multimodal imaging system was investigated in a preliminary study of multimodal imaging of plasmodium parasites in mosquito midguts (chapter 7). The OCT motion-contrast imaging was also performed by imaging a living mosquito sample for potential parasite motion detection inside the midgut. Previously, fluorescence microscopy was used for studying the malaria parasite invasion process both in vivo and ex vivo[160]. Our OCT imaging technique is label-free and can provide higher imaging depth compared to fluorescence microscopy. Due to the depth-resolving capability of OCT, 3D images with

high resolution and faster scanning can be achieved without a need for performing time-consuming optical sectioning, a required step in confocal fluorescence microscopy.

8.2 Limitations

One limiting factor for the proposed multimodal imaging technology, especially for clinical applications is speed of the PAM imaging, which is limited by the scanning mechanism and the PRR of the laser. Thus, a high PRR laser with stable pulse energy is always desired for improving the imaging speed. Fast scanning technique is essential for achieving fast imaging speed. Current optical scanning can achieve fast imaging speed in a very limited FOV. The FOV of current optical scanning OR-PAM is limited by the FOV of the unfocused ultrasonic transducer, which also limits the SNR of PAM. Thus, future improvement on the proposed multimodal imaging technology highly relies on the performance and design of the ultrasonic detection techniques.

Another limiting factor for the application of the presented imaging technology is how to extract critical information quantitatively from these images for diagnosis and clinical research. Further investigation is needed before this imaging system can make a significant impact in practical applications. One achievable improvement is to include the function of imaging blood oxygenation by using multiple illuminating wavelengths. This will add more value to the proposed multimodal imaging technology.

In conclusion, the Penta-modal optical imaging system is still in the early stages of development, especially for clinical application. It relies on the advancement of laser, scanning mechanisms, and ultrasound detection techniques to make significant impact on

disease diagnosis and research. Further studies, including in vivo human imaging, are required to enable the imaging system for practical applications and use it for preclinical and clinical environments. Simultaneous imaging of multiple contrasts with precise spatial registration potentially has significant impact on biomedical research and applications. Upon the above-mentioned improvements on the Penta-modal imaging system, it is expected that the presented imaging system will have the potential to provide more valuable information for research and diseases studies.

8.3 Potential Applications and Future Work

The multimodal imaging system outlined in this dissertation can be useful in a variety of applications thanks to the specific optical contrast offered by each employed modality. Here, we discuss a number of potential applications of the proposed Penta-modal imaging system, retinal and brain imaging.

8.3.1 Retinal Multimodal Imaging

Various retinal diseases are linked to the alteration of some specific biomarkers and molecules in the retina such as lipofuscin/A2E. Changes in retina tissue structure and blood flow has also been shown to be a symptom of different diseases[163]. For example, lipofuscin along with A2E are found in RPE layer of the retina and accumulates with age. This accumulation occurs in retinal degenerative diseases like Age-related Macular Degeneration (AMD) resulting in reduction of cell viability as well as weakening of the RPE cells and their line of defense [164]. It has been hypothesized that the choroidal blood flow may predict diseases progression. For example, decrease in foveolar choroidal blood

flow may be associated with AMD. It has also shown that eyes with dry AMD experience a decrease in choriocapillaris density, which may be associated with drusen [164].

The proposed Penta-modal imaging system has the potential to be used for in vivo retinal imaging to simultaneously measure several involved biomarkers. The system can image endogenous agents including melanin, lipofuscin, scattering, as well as blood flow. Exogenous contrast agents can also be utilized. The obtained information can be useful for future development of therapeutic and treatment strategies.

8.3.2 Brain Multimodal Imaging

Brain function requires a strictly regulated relationship between cerebral blood flow (CBF), neuronal activity, and energy metabolism. Various pathological and neurodegenerative conditions at different stages, including cancer, stroke and Alzheimer's disease are associated with notable alternations in energy metabolism, signaling and cerebral blood flow [165-167]. Therefore, an in-depth understanding of the relationship between neural activity, energy metabolism and their effect on CBF is vital for understanding brain function in health and under pathological conditions.

The presented multimodal optical imaging system can prove to be useful for a high spatial temporal resolution analysis of cerebral metabolism and hemodynamics in vivo. With some improvement, the imaging system will be able to measure multiple parameters of cerebral energetics in a living tissue, including vascular structure, blood flow, blood vessel oxygen saturation and neuronal network. The improvement includes replacing the pulsed laser with a femto-second high power laser and the use of multiple wavelengths for multiphoton confocal microscopy (MPM) and PAM, respectively. Obtaining such information will be

beneficial for further investigation of relationship between cerebral microvasculature and various cell types in both healthy and diseased brains [168-170].

REFERENCES

1 Balas, C. Review of biomedical optical imaging—a powerful, non-invasive, non-ionizing technology for improving in vivo diagnosis. *Measurement science and technology* **20**, 104020 (2009).

2 Lv, J. *et al.* In vivo photoacoustic imaging dynamically monitors the structural and functional changes of ischemic stroke at a very early stage. *Theranostics* **10**, 816 (2020).

3 Xiao, M., Dai, C., Li, L., Zhou, C. & Wang, F. Evaluation of Retinal Pigment Epithelium and Choroidal Neovascularization in Rats Using Laser-Scanning Optical-Resolution Photoacoustic Microscopy. *Ophthalmic research*, 1-13 (2019).

4 Shuaib, M. M., Helmy, G. M., Eldin, N. B., Elnahry, A. G. & Elnahry, G. A. Optical coherence tomography of the optic nerve head before and after optic nerve sheath fenestration for idiopathic intracranial hypertension. *Acta Neurologica Belgica*, 1-3 (2020).

5 Schönfeldt-Lecuona, C. *et al.* From imaging the brain to imaging the retina: optical coherence tomography (OCT) in schizophrenia. *Schizophrenia bulletin* **42**, 9-14 (2016).

6 Chen, W., You, J., Gu, X., Du, C. & Pan, Y. High-speed swept source optical coherence Doppler tomography for deep brain microvascular imaging. *Scientific reports* **6**, 38786 (2016).

7 Haindl, R. *et al.* in *Ophthalmic Technologies XXVI.* 969302 (International Society for Optics and Photonics).

8 Park, K. S., Shin, J. G., Qureshi, M. M., Chung, E. & Eom, T. J. Deep brain optical coherence tomography angiography in mice: in vivo, noninvasive imaging of hippocampal formation. *Scientific reports* **8**, 1-7 (2018).

9 Coscas, F. *et al.* Optical coherence tomography angiography in retinal vein occlusion: evaluation of superficial and deep capillary plexa. *American journal of ophthalmology* **161**, 160-171. e162 (2016).

10 Mikami, H. *et al.* Ultrafast confocal fluorescence microscopy beyond the fluorescence lifetime limit. *Optica* **5**, 117-126 (2018).

11 Wu, Z. *et al.* Multi-photon microscopy in cardiovascular research. *Methods* **130**, 79-89 (2017).

12 Ferradal, S. L. *et al.* Functional imaging of the developing brain at the bedside using diffuse optical tomography. *Cerebral cortex* **26**, 1558-1568 (2016).

13 Desroches, J. *et al.* A new method using Raman spectroscopy for in vivo targeted brain cancer tissue biopsy. *Scientific reports* **8**, 1-10 (2018).

14 Mlodzianoski, M. *et al.* Active PSF Shaping and Adaptive Optics Enable Volumetric Single Molecule Super-Resolution Microscopy through Brain Sections. *Biophysical Journal* **116**, 283a-284a (2019).

15 Jeon, S., Kim, J., Lee, D., Baik, J. W. & Kim, C. Review on practical photoacoustic microscopy. *Photoacoustics* **15**, 100141 (2019).

16 Xu, M. & Wang, L. V. Photoacoustic imaging in biomedicine. *Review of scientific instruments* **77**, 041101 (2006).

17 Kim, J., Lee, D., Jung, U. & Kim, C. Photoacoustic imaging platforms for multimodal imaging. *Ultrasonography* **34**, 88 (2015).

18 Liu, W. & Yao, J. Photoacoustic microscopy: principles and biomedical applications. *Biomedical engineering letters* **8**, 203-213 (2018).

19 Strohm, E. M., Moore, M. J. & Kolios, M. C. Single cell photoacoustic microscopy: a review. *IEEE Journal of Selected Topics in Quantum Electronics* **22**, 137-151 (2015).

20 Fang, P. *et al.* Technical principles of OCT angiography. *Der Ophthalmologe: Zeitschrift der Deutschen Ophthalmologischen Gesellschaft* **113**, 6-13 (2016).

21 Han, I. C. & Jaffe, G. J. Comparison of spectral-and time-domain optical coherence tomography for retinal thickness measurements in healthy and diseased eyes. *American journal of ophthalmology* **147**, 847-858. e841 (2009).

22 De Boer, J. F., Leitgeb, R. & Wojtkowski, M. Twenty-five years of optical coherence tomography: the paradigm shift in sensitivity and speed provided by Fourier domain OCT. *Biomedical optics express* **8**, 3248-3280 (2017).

23 Radadia, H. C., Sapre, A. A., Joshiyara, P. P., Shah, D. M. & Ninama, N. A. Analysis of macular thickness by spectral domain OCT in normal healthy population of Gujrat, India. *Indian Journal of Clinical and Experimental Ophthalmology* **4**, 131-135 (2018).

24 de Oliveira Dias, J. R. *et al.* Natural history of subclinical neovascularization in nonexudative age-related macular degeneration using swept-source OCT angiography. *Ophthalmology* **125**, 255-266 (2018).

25 Huang, D. *et al.* Optical coherence tomography. *science* **254**, 1178-1181 (1991).

26 Inohara, T. *et al.* Lesion morphological classification by OCT to predict therapeutic efficacy after balloon pulmonary angioplasty in CTEPH. *International journal of cardiology* **197**, 23-25 (2015).

27 Kardon, R. The role of the macula OCT scan in neuro-ophthalmology. *Journal of neuro-ophthalmology: the official journal of the North American Neuro-Ophthalmology Society* **31**, 353 (2011).

28 Welzel, J. Optical coherence tomography in dermatology: a review. *Skin Research and Technology: Review article* **7**, 1-9 (2001).

29 Chiu, S. J. *et al.* Validated automatic segmentation of AMD pathology including drusen and geographic atrophy in SD-OCT images. *Investigative ophthalmology & visual science* **53**, 53-61 (2012).

30 Huang, D., Jia, Y., Rispoli, M., Tan, O. & Lumbroso, B. OCT Angiography of time course of choroidal neovascularization in response to anti-angiogenic treatment. *Retina (Philadelphia, Pa.)* **35**, 2260 (2015).

31 Leitgeb, R. A., Werkmeister, R. M., Blatter, C. & Schmetterer, L. Doppler optical coherence tomography. *Progress in retinal and eye research* **41**, 26-43 (2014).

32 Wang, Y., Bower, B. A., Izatt, J. A., Tan, O. & Huang, D. Retinal blood flow measurement by circumpapillary Fourier domain Doppler optical coherence tomography. *Journal of biomedical optics* **13**, 064003 (2008).

33 Makita, S., Hong, Y., Yamanari, M., Yatagai, T. & Yasuno, Y. Optical coherence angiography. *Optics express* **14**, 7821-7840 (2006).

34 Park, S. S., Thinda, S., Kim, D. Y., Zawadzki, R. J. & Werner, J. S. Phase-variance optical coherence tomographic angiography imaging of choroidal perfusion changes associated with acute posterior multifocal placoid pigment epitheliopathy. *JAMA ophthalmology* **134**, 943-945 (2016).

35 Ploner, S. B. *et al.* in *Bildverarbeitung für die Medizin 2018* 98-102 (Springer, 2018).

36 Chu, Z. *et al.* Complex signal-based optical coherence tomography angiography enables in vivo visualization of choriocapillaris in human choroid. *Journal of biomedical optics* **22**, 121705 (2017).

37 Hwang, T. S. *et al.* Optical coherence tomography angiography features of diabetic retinopathy. *Retina (Philadelphia, Pa.)* **35**, 2371 (2015).

38 Lee, E. J., Lee, K. M., Lee, S. H. & Kim, T.-W. OCT angiography of the peripapillary retina in primary open-angle glaucoma. *Investigative ophthalmology & visual science* **57**, 6265-6270 (2016).

39 Moult, E. *et al.* Ultrahigh-speed swept-source OCT angiography in exudative AMD. *Ophthalmic Surgery, Lasers and Imaging Retina* **45**, 496-505 (2014).

40 Suzuki, N. *et al.* Microvascular abnormalities on optical coherence tomography angiography in macular edema associated with branch retinal vein occlusion. *American journal of ophthalmology* **161**, 126-132. e121 (2016).

41 Baran, U., Choi, W. J. & Wang, R. K. Potential use of OCT-based microangiography in clinical dermatology. *Skin research and technology* **22**, 238-246 (2016).

42 Lee, H.-C. *et al.* in *Biomedical Imaging and Sensing Conference.* 107110A (International Society for Optics and Photonics).

43 Wylęgała, A. Principles of OCTA and applications in clinical neurology. *Current neurology and neuroscience reports* **18**, 96 (2018).

44 Nie, S., Chiu, D. T. & Zare, R. N. Probing individual molecules with confocal fluorescence microscopy. *Science* **266**, 1018-1021 (1994).

45 Gustafsson, M. G. *et al.* Three-dimensional resolution doubling in wide-field fluorescence microscopy by structured illumination. *Biophysical journal* **94**, 4957-4970 (2008).

46 Hackley, P. C., Jubb, A. M., Burruss, R. C. & Beaven, A. E. Fluorescence spectroscopy of ancient sedimentary organic matter via confocal laser scanning microscopy (CLSM). *International Journal of Coal Geology*, 103445 (2020).

47 Wang, P., Wu, T.-H. & Zhang, Y. Monitoring and visualizing of PAHs into mangrove plant by two-photon laser confocal scanning microscopy. *Marine pollution bulletin* **64**, 1654-1658 (2012).

48 Ilie, M. A. *et al.* Current and future applications of confocal laser scanning microscopy imaging in skin oncology. *Oncology letters* **17**, 4102-4111 (2019).

49 Langer, G., Bouchal, K.-D., Grün, H., Burgholzer, P. & Berer, T. Two-photon absorption-induced photoacoustic imaging of Rhodamine B dyed polyethylene spheres using a femtosecond laser. *Optics express* **21**, 22410-22422 (2013).

50 Tan, Z. *et al.* Multimodal subcellular imaging with microcavity photoacoustic transducer. *Optics express* **19**, 2426-2431 (2011).

51 Song, W. *et al.* Fully integrated reflection-mode photoacoustic, two-photon, and second harmonic generation microscopy in vivo. *Scientific reports* **6**, 32240 (2016).

52 Subochev, P., Fiks, I. & Frenz, M. Simultaneous triple-modality imaging of diffuse reflectance, optoacoustic pressure and ultrasonic scattering using an acoustic-resolution photoacoustic microscope: feasibility study. *Laser physics letters* **13**, 025605 (2016).

53 Rao, B., Soto, F., Kerschensteiner, D. & Wang, L. V. Integrated photoacoustic, confocal, and two-photon microscope. *Journal of biomedical optics* **19**, 036002 (2014).

54 Zhang, X. *et al.* Simultaneous dual molecular contrasts provided by the absorbed photons in photoacoustic microscopy. *Optics letters* **35**, 4018-4020 (2010).

55 Zhang, X., Puliafito, C. A., Jiao, S. & Zhang, H. F. Simultaneous in vivo imaging of melanin and lipofuscin in the retina with photoacoustic ophthalmoscopy and autofluorescence imaging. *Journal of biomedical optics* **16**, 080504 (2011).

56 Wang, Y., Maslov, K., Kim, C., Hu, S. & Wang, L. V. Integrated photoacoustic and fluorescence confocal microscopy. *IEEE Transactions on Biomedical Engineering* **57**, 2576-2578 (2010).

57 Jiao, S., Xie, Z., Zhang, H. F. & Puliafito, C. A. Simultaneous multimodal imaging with integrated photoacoustic microscopy and optical coherence tomography. *Optics letters* **34**, 2961-2963 (2009).

58 Zhang, X., Jiao, S. & Zhang, H. Optical coherence photoacoustic microscopy: accomplishing optical coherence tomography and photoacoustic microscopy with a single light source. *Journal of biomedical optics* **17**, 030502 (2012).

59 Liu, X. *et al.* Optical coherence photoacoustic microscopy for in vivo multimodal retinal imaging. *Optics letters* **40**, 1370-1373 (2015).

60 Bondu, M. *et al.* Multispectral photoacoustic microscopy and optical coherence tomography using a single supercontinuum source. *Photoacoustics* **9**, 21-30 (2018).

61 Lee, C. *et al.* Combined photoacoustic and optical coherence tomography using a single near-infrared supercontinuum laser source. *Applied optics* **52**, 1824-1828 (2013).

62 Liu, X., Wen, R., Li, Y. & Jiao, S. Optical coherence photoacoustic microscopy (OC-PAM) with an intensity-modulated continuous-wave broadband light source. *Journal of Optics* **18**, 064001 (2016).

63 Huang, D. *et al.* Optical coherence tomography. *Science (New York, NY)* **254**, 1178 (1991).

64 Wojtkowski, M. *et al.* Ultrahigh-resolution, high-speed, Fourier domain optical coherence tomography and methods for dispersion compensation. *Optics express* **12**, 2404-2422 (2004).

65 de Venecia, G., Davis, M. & Engerman, R. Clinicopathologic correlations in diabetic retinopathy: I. Histology and fluorescein angiography of microaneurysms. *Archives of Ophthalmology* **94**, 1766-1773 (1976).

66 Földes-Papp, Z., Demel, U. & Tilz, G. P. Laser scanning confocal fluorescence microscopy: an overview. *International immunopharmacology* **3**, 1715-1729 (2003).

67 Holz, F. G., Bellmann, C., Rohrschneider, K., Burk, R. O. & Voölcker, H. E. Simultaneous confocal scanning laser fluorescein and indocyanine green angiography. *American journal of ophthalmology* **125**, 227-236 (1998).

68 Cai, X., Zhang, Y. S., Xia, Y. & Wang, L. V. Photoacoustic microscopy in tissue engineering. *Materials today* **16**, 67-77 (2013).

69 Liu, W. & Zhang, H. F. Photoacoustic imaging of the eye: A mini review. *Photoacoustics* **4**, 112-123 (2016).

70 Chang, C.-J. & Hou, K.-H. High-resolution optical Doppler tomography for in vitro and in vivo fluid flow dynamics. *Chang Gung medical journal* **26**, 403-411 (2003).

71 You, J., Du, C., Volkow, N. D. & Pan, Y. Optical coherence Doppler tomography for quantitative cerebral blood flow imaging. *Biomedical optics express* **5**, 3217-3230 (2014).

72 Fercher, A. F. Optical coherence tomography. *Journal of Biomedical Optics* **1**, 157-174 (1996).

73 Gladkova, N. D. *et al.* In vivo optical coherence tomography imaging of human skin: norm and pathology. *Skin Research and Technology* **6**, 6-16 (2000).

74 Gupta, M., Rollins, A. M., Izatt, J. A. & Efimov, I. R. Imaging of the atrioventricular node using optical coherence tomography. *Journal of cardiovascular electrophysiology* **13**, 95-95 (2002).

75 Swanson, E. A. *et al.* In vivo retinal imaging by optical coherence tomography. *Optics letters* **18**, 1864-1866 (1993).

76 Brand, S. *et al.* Optical coherence tomography in the gastrointestinal tract. *Endoscopy* **32**, 796-803 (2000).

77 An, L. & Wang, R. K. In vivo volumetric imaging of vascular perfusion within human retina and choroids with optical micro-angiography. *Optics Express* **16**, 11438-11452 (2008).

78 Cherecheanu, A. P., Garhofer, G., Schmidl, D., Werkmeister, R. & Schmetterer, L. Ocular perfusion pressure and ocular blood flow in glaucoma. *Current opinion in pharmacology* **13**, 36-42 (2013).

79 Ehrlich, R. *et al.* Age-related ocular vascular changes. *Graefe's Archive for Clinical and Experimental Ophthalmology* **247**, 583 (2009).

80 Xia, J., Yao, J. & Wang, L. V. Photoacoustic tomography: principles and advances. *Electromagnetic waves (Cambridge, Mass.)* **147**, 1 (2014).

81 Yao, J. & Wang, L. V. Sensitivity of photoacoustic microscopy. *Photoacoustics* **2**, 87-101 (2014).

82 Gottschalk, S., Felix Fehm, T., Luís Deán-Ben, X. & Razansky, D. Noninvasive real-time visualization of multiple cerebral hemodynamic parameters in whole mouse brains using five-dimensional optoacoustic tomography. *Journal of Cerebral Blood Flow & Metabolism* **35**, 531-535 (2015).

83 Jansen, K., Van Der Steen, A. F., van Beusekom, H. M., Oosterhuis, J. W. & van Soest, G. Intravascular photoacoustic imaging of human coronary atherosclerosis. *Optics letters* **36**, 597-599 (2011).

84 Oh, J.-T. *et al.* Three-dimensional imaging of skin melanoma in vivo by dual-wavelength photoacoustic microscopy. *Journal of biomedical optics* **11**, 034032-034032-034034 (2006).

85 Yao, J. *et al.* High-speed label-free functional photoacoustic microscopy of mouse brain in action. *Nature methods* **12**, 407-410 (2015).

86 Lichtman, J. W. & Conchello, J.-A. Fluorescence microscopy. *Nature methods* **2**, 910 (2005).

87 Webb, R. H. Confocal optical microscopy. *Reports on Progress in Physics* **59**, 427 (1996).

88 Wagnieres, G. A., Star, W. M. & Wilson, B. C. In vivo fluorescence spectroscopy and imaging for oncological applications. *Photochemistry and photobiology* **68**, 603-632 (1998).

89 Ntziachristos, V., Tung, C.-H., Bremer, C. & Weissleder, R. Fluorescence molecular tomography resolves protease activity in vivo. *Nature medicine* **8**, 757 (2002).

90 Klohs, J. *et al.* Near-infrared fluorescence imaging with fluorescently labeled albumin: a novel method for non-invasive optical imaging of blood–brain barrier impairment after focal cerebral ischemia in mice. *Journal of neuroscience methods* **180**, 126-132 (2009).

91 Chong, S. P., Lai, T., Zhou, Y. & Tang, S. Tri-modal microscopy with multiphoton and optical coherence microscopy/tomography for multi-scale and multi-contrast imaging. *Biomedical optics express* **4**, 1584-1594 (2013).

92 Berer, T., Leiss-Holzinger, E., Hochreiner, A., Bauer-Marschallinger, J. & Buchsbaum, A. Multimodal noncontact photoacoustic and optical coherence tomography imaging using wavelength-division multiplexing. *Journal of biomedical optics* **20**, 046013-046013 (2015).

93 Yue, S., Slipchenko, M. N. & Cheng, J. X. Multimodal nonlinear optical microscopy. *Laser & photonics reviews* **5**, 496-512 (2011).

94 Park, J. *et al.* A dual-modality optical coherence tomography and fluorescence lifetime imaging microscopy system for simultaneous morphological and biochemical tissue characterization. *Biomedical optics express* **1**, 186-200 (2010).

95 Nafar, Z., Jiang, M., Wen, R. & Jiao, S. Visible-light optical coherence tomography-based multimodal retinal imaging for improvement of fluorescent intensity quantification. *Biomedical optics express* **7**, 3220-3229 (2016).

96 Jiang, M., Liu, T., Liu, X. & Jiao, S. Simultaneous optical coherence tomography and lipofuscin autofluorescence imaging of the retina with a single broadband light source at 480nm. *Biomedical optics express* **5**, 4242-4248 (2014).

97 Dai, C., Liu, X. & Jiao, S. Simultaneous optical coherence tomography and autofluorescence microscopy with a single light source. *Journal of biomedical optics* **17**, 0805021-0805023 (2012).

98 Soliman, D., Tserevelakis, G. J., Omar, M. & Ntziachristos, V. Combining microscopy with mesoscopy using optical and optoacoustic label-free modes. *Scientific reports* **5**, 12902 (2015).

99 Yeh, C., Soetikno, B. T., Hu, S., Maslov, K. I. & Wang, L. V. Microvascular quantification based on contour-scanning photoacoustic microscopy. *Journal of biomedical optics* **19**, 096011 (2014).

100 Ning, B. *et al.* Ultrasound-aided multi-parametric photoacoustic microscopy of the mouse brain. *Scientific reports* **5**, 18775 (2015).

101 Dai, C., Liu, X., Zhang, H. F., Puliafito, C. A. & Jiao, S. Absolute retinal blood flow measurement with a dual-beam Doppler optical coherence tomography. *Investigative ophthalmology & visual science* **54**, 7998-8003 (2013).

102 Kroeker, C. G. Cardiovascular System:: Anatomy and Physiology. *Cardiovascular Mechanics*, 1-17 (2018).

103 Dai, C., Liu, X., Zhang, H. F., Puliafito, C. A. & Jiao, S. Absolute Retinal Blood Flow Measurement With a Dual-Beam Doppler Optical Coherence TomographyImaging Retinal Blood Flow With Dual-Beam OCT. *Investigative ophthalmology & visual science* **54**, 7998-8003 (2013).

104 Wehbe, H. *et al.* Automatic retinal blood flow calculation using spectral domain optical coherence tomography. *Optics Express* **15**, 15193-15206 (2007).

105 Jang, W. H. *et al.* In vivo characterization of early-stage radiation skin injury in a mouse model by two-photon microscopy. *Scientific reports* **6**, 19216 (2016).

106 Li, C., Pitsillides, C., Runnels, J. M., Côté, D. & Lin, C. P. Multiphoton microscopy of live tissues with ultraviolet autofluorescence. *IEEE Journal of selected topics in quantum electronics* **16**, 516 (2010).

107 Jiao, S., Knighton, R., Huang, X., Gregori, G. & Puliafito, C. A. Simultaneous acquisition of sectional and fundus ophthalmic images with spectral-domain optical coherence tomography. *Optics express* **13**, 444-452 (2005).

108 Boulton, M., McKechnie, N., Breda, J., Bayly, M. & Marshall, J. The formation of autofluorescent granules in cultured human RPE. *Investigative ophthalmology & visual science* **30**, 82-89 (1989).

109 Sparrow, J. R. & Boulton, M. RPE lipofuscin and its role in retinal pathobiology. *Experimental eye research* **80**, 595-606 (2005).

110 Johnson, E. J. Age-related macular degeneration and antioxidant vitamins: recent findings. *Current Opinion in Clinical Nutrition & Metabolic Care* **13**, 28-33 (2010).

111 Keller, P. J. Imaging morphogenesis: technological advances and biological insights. *Science* **340**, 1234168 (2013).

112 Jiao, S. *et al.* Photoacoustic ophthalmoscopy for in vivo retinal imaging. *Optics express* **18**, 3967-3972 (2010).

113 Li, L. *et al.* Fast subcellular optical coherence photoacoustic microscopy for pigment cell imaging. *Optics letters* **40**, 4448-4451 (2015).

114 Fatakdawala, H. *et al.* Multimodal in vivo imaging of oral cancer using fluorescence lifetime, photoacoustic and ultrasound techniques. *Biomedical optics express* **4**, 1724-1741 (2013).

115 Rao, B., Li, L., Maslov, K. & Wang, L. Hybrid-scanning optical-resolution photoacoustic microscopy for in vivo vasculature imaging. *Optics letters* **35**, 1521-1523 (2010).

116 Dadkhah, A., Zhou, J., Yeasmin, N. & Jiao, S. Integrated multimodal photoacoustic microscopy with OCT-guided dynamic focusing. *Biomedical optics express* **10**, 137-150 (2019).

117 Bowman, F. D., Drake, D. F. & Huddleston, D. E. Multimodal imaging signatures of Parkinson's disease. *Frontiers in neuroscience* **10**, 131 (2016).

118 Scelsi, M. A. *et al.* Genetic study of multimodal imaging Alzheimer's disease progression score implicates novel loci. *Brain* **141**, 2167-2180 (2018).

119 Nafar, Z., Wen, R. & Jiao, S. Visible-light optical coherence tomography-based multimodal system for quantitative fundus autofluorescence imaging. *Experimental Biology and Medicine* **243**, 1265-1274 (2018).

120 Lim, C. W. *et al.* Optical coherence tomography angiography of the macula and optic nerve head: microvascular density and test-retest repeatability in normal subjects. *BMC ophthalmology* **18**, 315 (2018).

121 Feucht, N. *et al.* Optical coherence tomography angiography indicates associations of the retinal vascular network and disease activity in multiple sclerosis. *Multiple Sclerosis Journal* **25**, 224-234 (2019).

122 Hagag, A. M., Gao, S. S., Jia, Y. & Huang, D. Optical coherence tomography angiography: technical principles and clinical applications in ophthalmology. *Taiwan journal of ophthalmology* **7**, 115 (2017).

123 Pircher, M. & Zawadzki, R. J. Review of adaptive optics OCT (AO-OCT): principles and applications for retinal imaging. *Biomedical optics express* **8**, 2536-2562 (2017).

124 Tsai, T.-H. *et al.* Optical coherence tomography in gastroenterology: a review and future outlook. *Journal of biomedical optics* **22**, 121716 (2017).

125 Saw, J. Coronary angiogram classification of spontaneous coronary artery dissection. *Catheterization and Cardiovascular Interventions* **84**, 1115-1122 (2014).

126 Wang, L., Murphy, O., Caldito, N. G., Calabresi, P. A. & Saidha, S. Emerging applications of optical coherence tomography angiography (OCTA) in neurological research. *Eye and Vision* **5**, 11 (2018).

127 Zhang, A., Zhang, Q., Chen, C.-L. & Wang, R. K. Methods and algorithms for optical coherence tomography-based angiography: a review and comparison. *Journal of biomedical optics* **20**, 100901 (2015).

128 Cadotte, D. W. *et al.* Speckle variance optical coherence tomography of the rodent spinal cord: in vivo feasibility. *Biomedical optics express* **3**, 911-919 (2012).

129 Schwartz, D. M. *et al.* Phase-variance optical coherence tomography: a technique for noninvasive angiography. *Ophthalmology* **121**, 180-187 (2014).

130 Enfield, J., Jonathan, E. & Leahy, M. In vivo imaging of the microcirculation of the volar forearm using correlation mapping optical coherence tomography (cmOCT). *Biomedical optics express* **2**, 1184-1193 (2011).

131 Conti, F. F. *et al.* Choriocapillaris and retinal vascular plexus density of diabetic eyes using split-spectrum amplitude decorrelation spectral-domain optical coherence tomography angiography. *British Journal of Ophthalmology* **103**, 452-456 (2019).

132 Bojikian, K. D. *et al.* Optic disc perfusion in primary open angle and normal tension glaucoma eyes using optical coherence tomography-based microangiography. *PloS one* **11**, e0154691 (2016).

133 Wang, L., Li, Y., Li, Y. & Li, K. Improved speckle contrast optical coherence tomography angiography. *American journal of translational research* **10**, 3025 (2018).

134 Dadkhah, A. & Jiao, S. Optical coherence tomography-guided dynamic focusing for combined optical and mechanical scanning multimodal photoacoustic microscopy. *Journal of biomedical optics* **24**, 121906 (2019).

135 Kelly, K. A. *et al.* Detection of vascular adhesion molecule-1 expression using a novel multimodal nanoparticle. *Circulation research* **96**, 327-336 (2005).

136 Wylęgała, A. Principles of OCTA and applications in clinical neurology. *Current neurology and neuroscience reports* **18**, 1-10 (2018).

137 Kashani, A. H. *et al.* Optical coherence tomography angiography: a comprehensive review of current methods and clinical applications. *Progress in retinal and eye research* **60**, 66-100 (2017).

138 Gorczynska, I., Migacz, J. V., Zawadzki, R. J., Capps, A. G. & Werner, J. S. Comparison of amplitude-decorrelation, speckle-variance and phase-variance OCT angiography methods for imaging the human retina and choroid. *Biomedical optics express* **7**, 911-942 (2016).

139 Reich, M. *et al.* Comparison of current optical coherence tomography angiography methods in imaging retinal hemangioblastomas. *Translational vision science & technology* **9**, 12-12 (2020).

140 Matsunaga, D., Yi, J., Puliafito, C. A. & Kashani, A. H. OCT angiography in healthy human subjects. *Ophthalmic Surgery, Lasers and Imaging Retina* **45**, 510-515 (2014).

141 Rabiolo, A. *et al.* Comparison of methods to quantify macular and peripapillary vessel density in optical coherence tomography angiography. *PloS one* **13**, e0205773 (2018).

142 Tan, B. *et al.* Approaches to quantify optical coherence tomography angiography metrics. *Annals of Translational Medicine* **8** (2020).

143 Guduru, A., Lupidi, M., Gupta, A., Jalali, S. & Chhablani, J. Comparative analysis of autofluorescence and OCT angiography in Stargardt disease. *British Journal of Ophthalmology* **102**, 1204-1207 (2018).

144 Jia, Y. *et al.* Quantitative optical coherence tomography angiography of choroidal neovascularization in age-related macular degeneration. *Ophthalmology* **121**, 1435-1444 (2014).

145 Jia, Y. *et al.* Quantitative optical coherence tomography angiography of vascular abnormalities in the living human eye. *Proceedings of the National Academy of Sciences* **112**, E2395-E2402 (2015).

146 Fingler, J., Schwartz, D., Yang, C. & Fraser, S. E. Mobility and transverse flow visualization using phase variance contrast with spectral domain optical coherence tomography. *Optics express* **15**, 12636-12653 (2007).

147 Fingler, J., Zawadzki, R. J., Werner, J. S., Schwartz, D. & Fraser, S. E. Volumetric microvascular imaging of human retina using optical coherence tomography with a novel motion contrast technique. *Optics express* **17**, 22190-22200 (2009).

148 Kim, D. Y. *et al.* In vivo volumetric imaging of human retinal circulation with phase-variance optical coherence tomography. *Biomedical optics express* **2**, 1504-1513 (2011).

149 Wang, L., Chen, Z., Li, Y., Yang, J. & Li, Y. Optical coherence tomography angiography for noninvasive evaluation of angiogenesis in a limb ischemia mouse model. *Scientific reports* **9**, 1-9 (2019).

150 Zhang, Q. *et al.* Wide-field optical coherence tomography based microangiography for retinal imaging. *Scientific reports* **6**, 1-10 (2016).

151 Wang, R. K. Optical microangiography: a label-free 3-D imaging technology to visualize and quantify blood circulations within tissue beds in vivo. *IEEE Journal of Selected Topics in Quantum Electronics* **16**, 545-554 (2009).

152 Chen, C.-L. & Wang, R. K. Optical coherence tomography based angiography. *Biomedical optics express* **8**, 1056-1082 (2017).

153 Nafar, Z., Wen, R., Guan, Z., Li, Y. & Jiao, S. Quantifying lipofuscin in retinal pigment epithelium in vivo by visible-light optical coherence tomography-based multimodal imaging. *Scientific reports* **10**, 1-10 (2020).

154 Chu, Z. *et al.* Quantitative assessment of the retinal microvasculature using optical coherence tomography angiography. *Journal of biomedical optics* **21**, 066008 (2016).

155 Yao, X., Alam, M. N., Le, D. & Toslak, D. Quantitative optical coherence tomography angiography: a review. *Experimental Biology and Medicine* **245**, 301-312 (2020).

156 Smith, C. A., Hooper, M. L. & Chauhan, B. C. Optical coherence tomography angiography in mice: quantitative analysis after experimental models of retinal damage. *Investigative ophthalmology & visual science* **60**, 1556-1565 (2019).

157 Xu, J., Song, S., Li, Y. & Wang, R. K. Complex-based OCT angiography algorithm recovers microvascular information better than amplitude-or phase-based algorithms in phase-stable systems. *Physics in Medicine & Biology* **63**, 015023 (2017).

158 Sinden, R. Molecular interactions between Plasmodium and its insect vectors. *Cellular microbiology* **4**, 713-724 (2002).

159 Yoshida, S. *et al.* A single-chain antibody fragment specific for the Plasmodium berghei ookinete protein Pbs21 confers transmission blockade in the mosquito midgut. *Molecular and biochemical parasitology* **104**, 195-204 (1999).

160 Vlachou, D. *et al.* Real-time, in vivo analysis of malaria ookinete locomotion and mosquito midgut invasion. *Cellular microbiology* **6**, 671-685 (2004).

161 Kim, C. S., Qi, W., Zhang, J., Kwon, Y. J. & Chen, Z. Imaging and quantifying Brownian motion of micro-and nanoparticles using phase-resolved Doppler variance optical coherence tomography. *Journal of biomedical optics* **18**, 030504 (2013).

162 Ning, B. *et al.* Ultrasound-aided multi-parametric photoacoustic microscopy of the mouse brain. *Scientific reports* **5**, 1-7 (2015).

163 Bressler, N. M. & Bressler, S. B. in *Retina Fifth Edition* 1183-1212 (Elsevier Inc., 2012).

164 Ambati, J. & Fowler, B. J. Mechanisms of age-related macular degeneration. *Neuron* **75**, 26-39 (2012).

165 Kumar, A. & Foster, T. C. 10 Neurophysiology of Old Neurons and Synapses. *Brain aging: models, methods, and mechanisms*, 229 (2007).

166 Lin, M. T. & Beal, M. F. Mitochondrial dysfunction and oxidative stress in neurodegenerative diseases. *Nature* **443**, 787-795 (2006).

167 Wallace, D. C. A mitochondrial paradigm of metabolic and degenerative diseases, aging, and cancer: a dawn for evolutionary medicine. *Annu. Rev. Genet.* **39**, 359-407 (2005).

168 Srinivasan, V. J. *et al.* Depth-resolved microscopy of cortical hemodynamics with optical coherence tomography. *Optics letters* **34**, 3086-3088 (2009).

169 Sakadžić, S. *et al.* Imaging of oxygen partial pressure in cerebral vasculature and tissue using a two-photon-enhanced phosphorescent nanoprobe. *Nat. Methods* **7**, 755-759 (2010).

170 Yaseen, M. A. *et al.* Microvascular oxygen tension and flow measurements in rodent cerebral cortex during baseline conditions and functional activation. *Journal of Cerebral Blood Flow & Metabolism* **31**, 1051-1063 (2011).

APPENDICES

FIU Research & Economic Development
FLORIDA INTERNATIONAL UNIVERSITY

MEMORANDUM

To:	Dr. Shuliang Jiao
CC:	File
From:	Barbara L. Rodriguez, MBA, Associate Director for Research Integrity
Date:	August 8, 2018
Protocol Title:	"Imaging the mice with OCT and photoacoustic microscopy".

The Institutional Animal Care and Use Committee has renewed your protocol application.

Protocol Approval #:	IACUC-17-041-CR01		
TOPAZ Reference #:	200792		
Approval Date:	07/23/18	**Expiration Date:**	08/28/19
Special Conditions:	N/A		

As a requirement of IACUC re-approval, you are required to:

1. Submit an IACUC amendment application for all proposed additions or changes to your protocol. All changes and additions must be reviewed and approved by the IACUC prior to implementation.
2. Promptly submit an Event Form that will notify the IACUC regarding any unanticipated deaths, adverse events, unexpected study results or a phenotype that negatively impacts the welfare of an animal. As well as, any deviations from the approved protocol. Notification must still occur even if the issue has been identified and corrected. Notification must be timely, to minimize the effect on animal welfare
3. Receive annual review and re-approval of your study prior to your IACUC expiration date. Please submit the IACUC renewal form at least 30 days in advance of the study's expiration date. As a reminder, if your protocol has reached its third year; please submit a new application prior to your expiration date.
4. Submit an IACUC Project Completion Report Form when the study is finished or discontinued.

For further information, you may visit the FIU IACUC website at:
http://research.fiu.edu/iacuc/index.html.

OFFICE OF RESEARCH INTEGRITY
11200 SW 8th Street · MARC 430 · Miami, FL 33199 · Tel 305-348-2494 · Fax 305-348-6389 · www.fiu.edu

FIU Research & Economic Development
FLORIDA INTERNATIONAL UNIVERSITY

MEMORANDUM

To:	Dr. Shuliang Jiao, Principal Investigator
CC:	File
From:	Mario E. Sánchez, Research Integrity Coordinator
Date:	November 2, 2020
Protocol Title:	"Multimodal retinal functional imaging."

The Institutional Animal Care and Use Committee has renewed your protocol application.

Protocol Approval #: IACUC-18-046-CR02
TOPAZ Reference #: 200905
Approval Date: 07/25/2020 **Expiration Date:** 08/02/2021
Special Conditions: N/A

As a requirement of IACUC re-approval, you are required to:

1. Submit an IACUC amendment application for all proposed additions or changes to your protocol. All changes and additions must be reviewed and approved by the IACUC prior to implementation.
2. Promptly submit an Event Form that will notify the IACUC regarding any unanticipated deaths, adverse events, unexpected study results or a phenotype that negatively impacts the welfare of an animal. As well as, any deviations from the approved protocol. Notification must still occur even if the issue has been identified and corrected. Notification must be timely, to minimize the effect on animal welfare
3. Receive annual review and re-approval of your study prior to your IACUC expiration date. Please submit the IACUC renewal form at least 30 days in advance of the study's expiration date. As a reminder, if your protocol has reached its third year; please submit a new application prior to your expiration date.
4. Submit an IACUC Project Completion Report Form when the study is finished or discontinued.

For further information, you may visit the FIU IACUC website at:
http://research.fiu.edu/iacuc/index.html.

OFFICE OF RESEARCH INTEGRITY
11200 SW 8th Street · MARC 430 · Miami, FL 33199 · Tel 305-348-2494 · Fax 305-348-6389 · www.fiu.edu

VITA

ARASH DADKHAH

Born, Tehran, Iran

2007-2012 B.Sc., Mechanical Engineering, Solid Mechanics
Islamic Azad University
Tehran, Iran

2012-2014 M.S., Biomedical Engineering, Biomechanics
Amirkabir University of Technology
Tehran, Iran

2015-2021 Ph.D., Biomedical Engineering, Medical Optical Imaging
Florida Internatioal University
Miami, Florida

PUBLICATIONS AND PRESENTATION

+ Arash Dadkhah*, Jun Zhou, Nusrat Yeasmin and Shuliang Jiao, " Integrated multimodal photoacoustic microscopy with OCT- guided dynamic focusing" Biomedical Optics Express, 2019, 10: 137-150. https://doi.org/10.1364/BOE.10.000137. (Original article; 14 pages).

+ Arash Dadkhah*, and Shuliang Jiao, " Optical coherence tomography-guided dynamic focusing for combined optical and mechanical scanning multimodal photoacoustic microscopy" Journal of Biomedical Optics, 24(12), 121906 (2019), doi: 10.1117/1.JBO.24.12.121906. 2019 (Original article; 7 pages).

+ Arash Dadkhah*, and Shuliang Jiao, " Integrating Photoacoustic Microscopy, Optical Coherence Tomography, OCT Angiography, and Fluorescence Microscopy for Multimodal Imaging" Journal of Experimental Biology and Medicine, 2020; 245: 342–347. DOI: 10.1177/1535370219897584 (Original article; 6 pages).

+ Arash Dadkhah*, and Shuliang Jiao, " Integrating photoacoustic microscopy with other imaging technologies for multimodal imaging" Experimental Biology and Medicine 2020; 0: 1–7. DOI: 10.1177/1535370220977176 (Original article; 7 pages).

+ Arash Dadkhah*, Jun Zhou, Nusrat Yeasmin and Shuliang Jiao, "A multimodal imaging platform with integrated simultaneous photoacoustic microscopy, optical coherence tomography, optical Doppler tomography and fluorescence microscopy" Proc. SPIE.

10494, Photons Plus Ultrasound: Imaging and Sensing 2018, (Refereed conference proceeding; 7 pages).

+ Arash Dadkhah*, Xing Pang, Elizabeth Solis, Ruogu Fang and Anuradha Godavarty, " Wound size measurement of lower extremity ulcers using segmentation algorithms" Proc. SPIE. 9703, Optical Biopsy XIV: Toward Real-Time Spectroscopic Imaging and Diagnosis 2016 (Refereed conference proceeding; 6 pages).

+ Xing Pang, Arash Dadkhah, Jiali Lei, Elizabeth Solis, Suset Rodriguez, Francisco Perez-Clavijo, Stephen Wigley, Ruogu Fang, and Anuradha Godavarty, " Near-Infrared Optical Imaging and Wound Segmentation in Lower Extremity Ulcers " Proc. OSA Optics and the Brain, Biomedical Optics 2016 (Refereed conference proceeding).

+ Arash Dadkhah*, and Shuliang Jiao, "OCT-guided integrated multimodal photoacoustic microscopy for fast scanning speed and large scanning area" Photons Plus Ultrasound: Imaging and Sensing, SPIE, March 2019, San Francisco, California, United States (Oral).

+ Arash Dadkhah*, Jun Zhou, Nusrat Yeasmin and Shuliang Jiao, "A multimodal imaging platform with integrated simultaneous photoacoustic microscopy, optical coherence tomography, optical Doppler tomography and fluorescence microscopy" 10494, Photons Plus Ultrasound: Imaging and Sensing, SPIE, Feb 2018, San Francisco, California, United States (Oral).

+ Arash Dadkhah*, Xing Pang, Elizabeth Solis, Ruogu Fang and Anuradha Godavarty, "Wound size measurement of lower extremity ulcers using segmentation algorithms" 9703, Optical Biopsy XIV: Toward Real-Time Spectroscopic Imaging and Diagnosis, SPIE, March 2016, San Francisco, California, United States (Oral).

+ Xing Pang, Arash Dadkhah*, Jaili Lei, Elizabeth Solis, Suset Rodriguez, Francisco Perez-Clavijo, Stephen Wigley, Ruogu Fang, Anuradha Godvarty, "Near-Infrared Optical Imaging and Wound Segmentation in Lower Extremity Ulcers" OSA, Optical Society of America Annual Meeting, April 2016, Fort Lauderdale, Florida United States (Oral).

+ Arash Dadkhah*, Edwin Robledo, Trevor Solorzano, Jiali Lei, Anuradha Godavarty, " Functional Imaging of Diabetic Wound Using a Noncontact Near-Infrared Scanner: Instrumentation Development" MARC U*STAR & NIGMS RISE Student Mini-Symposium, FIU, Miami, FL, October 2016 (Oral).